
signature supervisor



DISSERTATION

Test of the Pauli Exclusion Principle for electrons in the Gran Sasso underground laboratory

at the Stefan Meyer Institute for subatomic physics

under the supervision of
Dr. Johann Marton

by

Andreas Pichler

Boltzmanngasse 3,
1090 Vienna

February 9, 2018

signature student

Kurzfassung

Abstract

The Pauli Exclusion Principle (PEP) is a fundamental principle in physics, governing the behavior of fermionic particles. Due to its importance, it needs to be tested as precisely as possible. In a pioneering experiment, Ramberg and Snow supplied an electric current to a Cu target, and searched for PEP violating atomic transitions of “fresh” electrons from the current. As these transitions are only expected when the current is on, the difference between the spectra with and without current can be used to set an upper limit for the violation of the PEP. The VIP (VIolation of Pauli Exclusion Principle) experiment could set this upper limit to 4.7×10^{-29} with the described method. The VIP2 experiment wants to improve this limit by upgrading crucial components of the setup.

One crucial component of the VIP2 setup are the Silcion Drift Detectors which detect the possible photons from PEP violating transitions. These detectors were tested in the laboratory of the Stefan Meyer Institute together with argon cooling, which kept their temperature at around 100 K. Their energy and time resolution were assessed during these tests and equaled 150 eV (FWHM) at 6 keV and 380 ns (FWHM) respectively. Another essential component of the setup are the 32 plastic scintillator bars read out by two Silicon Photo Multipliers each. The time resolution of one of these systems was 2.3 ns (FWHM). The system was installed to veto events in the SDDs caused by external ionizing radiation. The detection probability for 500 MeV e^- was tested at the beam test facility at LNF (Italy), were 98 % or these particles were detected. The outcome of all these measurement are fulfilling expectations and suffice for the purpose of the experiment.

After exhaustive tests, the setup was transported to the underground laboratory of Gran Sasso (LNGS). Data was taken from February 2016 until November 2017. An amount of about 142 days of data without current and 81 days with 100 A current were taken. Comparison of the data to Geant4 simulation showed that the majority of the background is induced by γ radiation originating from radioactive isotopes of the rocks of the mountain. The energy resolution around 8 keV, where events from the PEP-violating transition are expected, was measured. For the data without current, it equals 178 eV. For the data with current it is diminished to 189 eV, probably due to electronic noise introduced by the high current. Several analysis techniques for investigating the difference of the two energy spectra, and calculate the probability for a violation of the Pauli Exclusion Principle, were applied. The standard analysis of subtraction of the spectra in a region of interest defined around the expected energy of the forbidden transition yields a new upper limit of 1.87×10^{-29} . This is an improvement to the value set by the VIP experiment by a factor of 2.5.

Acknowledgement

acknowledgement

Contents

1. Introduction	1
2. Physics of the VIP2 experiment	3
2.1. Physics Basics	3
2.1.1. The Pauli Exclusion Principle	3
2.1.2. Quantum Mechanical Angular Momenta	4
2.1.3. The Spin	5
2.1.4. Indistinguishability, Symmetrization Postulate and Supers- election Rule	7
2.1.5. Fermions, Bosons and the Spin-Statistics Connection	11
2.2. Theories of Violation of Spin-Statistics	13
2.2.1. Parastatistics	13
2.2.2. The Ignatiev and Kuzmin Model and Parons	14
2.2.3. Quons	14
2.3. Tests of the Pauli Exclusion Principle	16
2.3.1. Remarks on Testing the Pauli Exclusion Principle	16
2.3.2. Experiments for Testing the Pauli Exclusion Principle	16
2.4. The VIP2 experimental method	19
3. The Measurement Setup	25
3.1. Silicon Drift Detectors and copper target	25
3.1.1. Working principle	26
3.1.2. SDD specifications for the VIP2 experiment	27
3.1.3. Silicon Drift Detectors performance characteristics	29
3.2. Active Shielding	30
3.2.1. Scintillators	30
3.2.2. Silicon Photomultipliers	31
3.3. Cooling system	32
3.4. Data acquisition and slow control systems	34
3.4.1. Signal readout and data acquisition	34
3.4.2. Slow control	36

4. Simulations	39
4.1. Detection Efficiency of PEP-violating Transitions	39
4.2. Background from Cosmic Radiation	41
4.3. Background from Gamma Radiation	44
5. Test Measurements	47
5.1. Test Measurements at LNF	47
5.2. Test Measurements at SMI	48
5.2.1. Water Cooling of Cu Target	49
5.2.2. Argon Cooling of Silicon Drift Detectors	50
5.2.3. Scintillator Energy Deposition Trigger Threshold	51
5.2.4. SDD Energy Resolution	52
5.2.5. SDD Time Resolution	54
5.2.6. Scintillator plus SiPM Time Resolution	54
5.2.7. Detection Efficiency of Cosmic Radiation and Active Shielding Test	56
6. Data Taking at LNGS and Data Preparation	63
6.1. Comparison of Data and Simulations	64
6.2. Effects of 100 A Current	66
6.3. Spectral Lines in the Energy Spectrum	68
6.4. Data Selection	69
6.5. Energy Calibration	71
6.6. Peak Stability and Data Splitting	74
6.7. Scale Linearity and 2 nd Order Correction	76
7. Data Analysis	83
7.1. Spectral Subtraction Analysis	84
7.2. Simultaneous Fit	87
7.3. Bayesian Count Based Analysis	89
7.4. Bayesian Fit Based Analysis	90
8. Summary and Outlook	93
Bibliography	i
Appendices	ix
A. Data Acquisition Layout	xi
B. Code for Simultaneous Fit	xiii

C. Code for Bayesian Analysis	xxi
C.1. Count Based Analysis	xxi
C.2. Fit Based Analysis	xxi

1. Introduction

The Pauli Exclusion Principle (PEP) is a fundamental principle in physics, valid for identical-fermion systems. It was formulated in 1925 by the austrian physicist Wolfgang Pauli. It states that two fermions (particles with half integer spin) can not occupy the same quantum state simultaneously. Examples for fermionic particles are elemenatry particles such as quarks, leptons (electron, muon and tauon) and neutrinos. Composite particles can also be fermions (e.g. protons and neutrons). Electrons, which make up the electronic shell of atoms, are fermions and therefore obey the PEP. For the case of electronic shells the PEP is equivalent to the statement that two electrons cannot have the same principal quantum number n , angular momentum quantum number l , magnetic quantum number m_l and spin quantum number m_s at the same time. This means that two electrons can share the quantum numbers n , l and m_l , as long as they have different spin quantum number m_s ($\pm \frac{1}{2}$).

The PEP forms the basis of the periodic table of elements, as it prevents all electrons in a shell to condense into the ground state. Therefore it is responsible for the occupation of the electronic shells and the chemical properties of elements. It also stabilizes of neutron stars, as the neutron degeneracy pressure, which is caused by the PEP, prevents them from collapsing under their own gravitational pressure. Furthermore it is intimately connected to electric conductivity, which will be described in chapter 2.

Due to the fundamental place of the PEP in quantum field theory, many researches were interested in testing it. In the year 1948, the Pauli Exclusion Principle was tested by Goldhaber and Scharff-Goldhaber [1]. Their experiment was designed to determine if the particles making up β radiation were the same as electrons, but it was later used to test the Pauli Exclusion Principle. The experiment was done by shining electrons from a β source onto a block of lead. The authors thought, if these β particles were different from electrons, they could be captured by the lead atoms and cascade down to the ground state without being subject to the PEP. The X-rays emitted during this cascading process were used to set an upper bound for the probability that the PEP is violated. Another thorough test was

conducted in 1988 by E. Ramberg and G. A. Snow [2]. They introduced a current into a copper conductor. The electrons of the current then had a chance to be absorbed by the copper atoms and form a new quantum state. The experimenters searched for states having a symmetric component in an otherwise antisymmetric state. These states were identified by the X-rays they emitted while decaying to the ground state. The same principle was later employed in the VIP experiment, which was able to set a new upper limit for the probability for the violation of the Pauli Exclusion Principle of:

$$\frac{\beta^2}{2} \leq 4.7 * 10^{-29}$$

([3], [4]). The follow-up experiment VIP2 is currently taking data in the Laboratori Nazionali del Gran Sasso (LNGS). The results, the setup configuration and various other aspects of this experiment will be discussed in the following chapters.

2. Physics of the VIP2 experiment

2.1. Physics Basics

2.1.1. The Pauli Exclusion Principle

To explain the spectra of alkali atoms recorded with a magnetic field (Zeemann effect), Wolfgang Pauli postulated a 4th quantum number for electrons in the early 1920s. The new quantum number was an addition to the quantum numbers already known to that time, which are nowadays called principal quantum number n , angular momentum quantum number l and magnetic quantum number m_l . He named it a “two-valuedness not describable classically” [5]. This 4th quantum number was later called the electron’s spin. Another problem he was working on at that time was the series of integer numbers 2, 8, 18, 32, etc., which was determining the lengths of the lines in what we call the periodic table of elements. It was furthermore known to him that the number of electronic energy levels in an alkali atom were the same as the number of electrons in the closed shell of the rare gas with the same principal quantum number. He used this information to formulate the Pauli Exclusion Principle: The number of electrons in closed subgroups can be reduced to one, if the division of the groups (by giving them values of the four quantum numbers) is carried so far that every degeneracy is removed. An entirely non-degenerate level is closed, if it is occupied by a single electron [5]. This is equivalent to saying that every state corresponding to a set of quantum numbers n , l , m_l and m_s can only be occupied by one electron. Wolfgang Pauli won the Nobel Prize in physics for the formulation of the Pauli Exclusion principle in 1945. It was first formulated for electrons, but later on extended to all fermions.

2.1.2. Quantum Mechanical Angular Momenta

From a classical point of view an angular momentum is defined as: $\vec{L} = \vec{r} \times \vec{p}$. In this formula \vec{L} is the angular momentum, \vec{r} is the vector to the particle from the origin and \vec{p} is the momentum of the particle. The magnetic moment of a particle with charge q moving in a circle with radius r is defined as $\vec{\mu} = I \times \vec{A}$. Here $\vec{\mu}$ is the magnetic moment, $\vec{A} = r^2\pi * e_A$ is the area that the particle's movement is encircling and I is the current. The current the particle generates can be written as:

$$I = \frac{q}{T} = \frac{q}{\frac{2r\pi}{v}} = \frac{qv}{2r\pi} \quad (2.1)$$

Here, v is the particle's velocity and T is the time it needs for one full circle. After dropping the vector arrows due to orthogonality, the magnetic moment can be written as:

$$\mu = IA = \frac{qv}{2r\pi} r^2\pi = \frac{qvr}{2} = \frac{q}{2m} rv m = \frac{q}{2m} L \quad (2.2)$$

Where $\frac{q}{2m} = \frac{\mu}{L}$ is called the gyromagnetic ratio. For electrons formula 2.2 is often rewritten in the form

$$\mu_e = g\mu_B \frac{L}{\hbar} \quad \mu_B = \frac{e\hbar}{2m_e} \quad \hbar = 1.054571800(13) \times 10^{-34} \left[\frac{m^2 kg}{rad \times s} \right] \quad (2.3)$$

where μ_e is the magnetic moment of the electron, m_e is the electron mass and μ_B is the Bohr magneton. The Bohr magneton is the expected ratio between the magnetic moment μ_e and the dimensionless value $\frac{L}{\hbar}$. The *g-factor* parametrizes deviations from the expected value $g = 1$, which could arise if for example the charge density distribution is different from the mass density distribution.

In analogy to classical mechanics, the angular momentum can be written in quantum mechanics as a cross product of the position operator \hat{x} and the momentum operator \hat{p} : $\hat{L} = \hat{x} \times \hat{p}$. In position basis this can be written as

$$\hat{L} = \hat{x} \times \hat{p} = \frac{\hbar}{i} (\vec{x} \times \vec{\nabla}) \quad \vec{\nabla} = \begin{pmatrix} \frac{\partial}{\partial x} \\ \frac{\partial}{\partial y} \\ \frac{\partial}{\partial z} \end{pmatrix} \quad (2.4)$$

In index notation, this operator can be written as follows: $\widehat{L}_i = \epsilon_{ijk} \widehat{x}_j \widehat{p}_k$ with ϵ_{ijk} being the antisymmetric Levi-Civita tensor. The indices i, j, k correspond to the 3 spatial dimensions. \widehat{L}_i and \widehat{L}_j do not commute as

$$[\widehat{L}_i, \widehat{L}_j] = i\hbar \epsilon_{ijk} \widehat{L}_k \quad [\widehat{X}, \widehat{Y}] = \widehat{X}\widehat{Y} - \widehat{Y}\widehat{X} \quad (2.5)$$

Here $[\widehat{X}, \widehat{Y}]$ denotes the commutator of \widehat{X} and \widehat{Y} . For readability, the hats of operators will be omitted from now on. The entries L_i of the angular momentum operator commute with the rotation invariant form $L^2 = L_x^2 + L_y^2 + L_z^2$. This is the operator of the squared norm of the angular momentum. L_i and L^2 are compatible variables and can be measured simultaneously. This also means that

$$[L_i, L^2] = 0 \quad (2.6)$$

For any given system, the following relations for the eigenvalues of these operators hold:

$$L_i |\phi\rangle = m_l \hbar |\phi\rangle \quad m_l \in \dots - 2, -1, 0, 1, 2, \dots \quad (2.7)$$

$$L^2 |\phi\rangle = \hbar^2 l(l+1) |\phi\rangle \quad l \in 0, 1, 2, \dots \quad (2.8)$$

with $|m_l| \leq l$. Considering particles without spin and a Hamiltonian symmetric under rotations of the form $H = \frac{p^2}{2m} + V(r)$ (like the atom), the angular momentum is conserved and commutes with the Hamiltonian

$$[H, L_i] = [H, L^2] = [L_i, L^2] = 0 \quad (2.9)$$

Therefore L_i and L^2 are conserved quantities. For systems without spin, H , L^2 and L_i form a complete set of commuting observables with the corresponding quantum numbers n (principal quantum number), l (angular momentum quantum number) and m_l (magnetic quantum number). Introducing the rotation invariant Coulomb potential for $V(r)$

$$V(r) = -\frac{1}{4\pi\epsilon_0} \frac{q}{r} \quad (2.10)$$

one finds that angular momentum quantum number l always needs to be smaller than the principal quantum number n ($l < n$). Only considering pure Coulomb interaction, the eigenstates with principal quantum number n belonging to the eigenvalue E_n are n^2 -fold degenerate.

2.1.3. The Spin

The spin is an intrinsic form of angular momentum carried by elementary particles. It has a definitive and non-modifiable magnitude for each particle type. This is a difference to the section 2.1.2, where the angular momenta, described by the quantum number l , could change in magnitude. Wolfgang Pauli was the first to propose the concept of spin in 1925. Analogous to the relation between angular momentum and magnetic moment 2.3, the relation between spin and angular momentum can be written as

$$\mu_s = g\mu_B \frac{S}{\hbar} \quad \mu_B = \frac{e\hbar}{2m} \quad (2.11)$$

where μ_s is the magnetic moment of a particle due to its spin and S is the magnitude of this spin. Unlike for angular momenta described in 2.1.2, the value for $g \neq 1$. From the Dirac equation, a value of $g = 2$ can be obtained. Corrections for example from Quantum Electrodynamics further alter this value on the %-level.

Analogous to equation 2.5 and 2.6, commutation relations can be found for the spin:

$$[S_i, S_j] = i\hbar\epsilon_{ijk}S_k \quad (2.12)$$

$$[S_i, S^2] = 0 \quad (2.13)$$

Here S_i are the spin components in one spatial direction and S^2 is the squared norm of the spin. Furthermore, analogous to equations 2.7 and 2.8 following relations hold for the spin:

$$S^2 |\phi\rangle = \hbar^2 s(s+1) |\phi\rangle \quad s \in 0, \frac{1}{2}, 1, \dots \quad (2.14)$$

$$S_i |\phi\rangle = m_s \hbar |\phi\rangle \quad |m_s| \leq s \quad (2.15)$$

Here s is the spin quantum number and m_s is the spin projection quantum number. The big difference between s and its analogon l from the previous chapter is that s can also take half-integer values. Another difference is, that s , unlike l , cannot be changed and is intrinsic for each particle type. Particles with half-integer spin quantum number are called *fermions*, particles with integer spin are called *bosons*. In particular, leptons such as electrons have $s = \frac{1}{2}$ and therefore m_s can take the values $\pm \frac{1}{2}$. For a system containing particles with spin, n , l , m_l and m_s form a complete set of commuting observables. The total angular momentum (\vec{J}) can be defined as the sum of the orbital angular momentum and spin $\vec{J} = \vec{L} + \vec{S}$. Analogous expressions to equations 2.5 - 2.9 hold for the total angular momentum \vec{J} in systems containing particles with spin.

Considering a system containing a particle with $s = \frac{1}{2}$. The basis in which S^2 and S_z are diagonal consists of two states $|s, m_s\rangle = |\frac{1}{2}, \pm \frac{1}{2}\rangle$. These states can be identified with the basis vectors $e_1 = \begin{pmatrix} 1 \\ 0 \end{pmatrix}$ and $e_2 = \begin{pmatrix} 0 \\ 1 \end{pmatrix}$ and are often referred to as “spin-up” and “spin-down” relative to a defined z-direction. The action of operators on these states is as follows:

$$S^2 \left| \frac{1}{2}, \pm \frac{1}{2} \right\rangle = \hbar^2 \frac{1}{2} \left(\frac{1}{2} + 1 \right) \left| \frac{1}{2}, \pm \frac{1}{2} \right\rangle \quad (2.16)$$

$$S_z \left| \frac{1}{2}, \frac{1}{2} \right\rangle = \hbar \frac{1}{2} \left| \frac{1}{2}, \frac{1}{2} \right\rangle \quad (2.17)$$

$$S_z \left| \frac{1}{2}, -\frac{1}{2} \right\rangle = -\hbar \frac{1}{2} \left| \frac{1}{2}, -\frac{1}{2} \right\rangle \quad (2.18)$$

$$S_+ \left| \frac{1}{2}, \frac{1}{2} \right\rangle = 0 \quad S_- \left| \frac{1}{2}, \frac{1}{2} \right\rangle = \hbar \left| \frac{1}{2}, -\frac{1}{2} \right\rangle \quad (2.19)$$

$$S_+ \left| \frac{1}{2}, -\frac{1}{2} \right\rangle = \hbar \left| \frac{1}{2}, \frac{1}{2} \right\rangle \quad S_- \left| \frac{1}{2}, -\frac{1}{2} \right\rangle = 0 \quad (2.20)$$

The *ladder operators* (S_{\pm}) were used in equations 2.19 and 2.20. A ladder operator increases (S_+) or decreases (S_-) the azimuthal quantum number of a state and for an angular momentum \vec{J} with quantum numbers j and m_j defined as

$$J_{\pm} |j, m_j\rangle = \hbar \sqrt{(j \mp m_j)(j \pm m_j + 1)} |j, m_j \pm 1\rangle \quad (2.21)$$

In the mentioned basis, the operators S_x , S_y and S_z can be written as

$$S_x = \frac{\hbar}{2} \begin{pmatrix} 0 & 1 \\ 1 & 0 \end{pmatrix}, \quad S_y = \frac{\hbar}{2} \begin{pmatrix} 0 & -i \\ i & 0 \end{pmatrix}, \quad S_z = \frac{\hbar}{2} \begin{pmatrix} 1 & 0 \\ 0 & -1 \end{pmatrix} \quad (2.22)$$

These are the so called *Pauli matrices*.

2.1.4. Indistinguishability, Symmetrization Postulate and Superselection Rule

The following section is loosely based on [6]. Considering a state $\phi = \phi(1, 2, \dots, i, \dots, j, \dots, N)$, where the variables 1, 2, ... denote the spatial and the spin degrees of freedom. The action of the permutation operator $P_{i,j}$ on this state is defined as:

$$P_{i,j} \phi(1, 2, \dots, i, \dots, j, \dots, N) = \phi(1, 2, \dots, j, \dots, i, \dots, N) \quad (2.23)$$

The indistinguishability of identical particles implies that states that differ only by a permutation of identical particles can not be distinguished by any measurement. In quantum mechanics, a measurement is expressed as the expectation value of a hermitian ¹ operator A . This statement can be expressed for a state ϕ as the following equation:

$$\langle \phi | A | \phi \rangle = \langle \phi | P^\dagger A P | \phi \rangle \quad (2.24)$$

From this equation follows that the permutation operator commutes with every observable, as it holds for every state ϕ and it follows that $P^\dagger A P = A$. Therefore PA

¹A hermitian or self-adjoint operator is an operator for which the relation $A^\dagger = A$ holds. The hermitian conjugation † corresponds to transposition combined with complex conjugation. A hermitian operator has real eigenvalues and eigenvectors for different eigenvalues are orthogonal.

$= AP$ which implies commutation of the two operators. Specifically, the energy of a quantum mechanical system also must not depend on the permutation of identical particles. From above considerations it follows that:

$$[P, H] = 0 \quad (2.25)$$

where H is the Hamiltonian.

An infinitesimal time evolution of a state is given by the Schrödinger equation

$$\partial_t |\phi(t)\rangle = \frac{1}{i\hbar} H |\phi(t)\rangle \Rightarrow |\phi(t + \delta t)\rangle = (1 + \frac{\delta t}{i\hbar} H + O(\delta t^2)) |\phi(t)\rangle \quad (2.26)$$

For a time-independent Hamiltonian H , $n \rightarrow \infty$ infinitesimal time steps between a start time t_0 and time t give the time evolution operator $U(t - t_0)$:

$$|\phi(t)\rangle = U(t - t_0) |\phi(t_0)\rangle \quad U(t - t_0) = e^{-\frac{i}{\hbar}(t-t_0)H} \quad (2.27)$$

As the permutation operator commutes with the Hamiltonian, it also commutes with the time evolution operator U ,

$$[P, U] = 0 \quad (2.28)$$

because of equation 2.27. Therefore, the permutation symmetry of a state is conserved. This is called the *Messiah-Greenberg (MG) superselection rule*. It is important to note that above considerations are only viable for systems where the number of particles is conserved and that the symmetry of a system is not necessarily preserved in systems with a non-constant particle number (see for example [7]).

Considering now a system of 2 particles, in which the state $|\phi(1, 2)\rangle$ is a solution of the Schrödinger equation

$$H |\phi(1, 2)\rangle = E |\phi(1, 2)\rangle \quad (2.29)$$

As the Hamiltonian commutes with the permutation operator, $P_{12} |\phi(1, 2)\rangle = |\phi(2, 1)\rangle$ is also a solution to this equation with the same Hamiltonian H and the same eigenvalue E . All linear combinations of these two functions are also solutions of the equation. The linear combinations $|\Phi\rangle = |\phi(1, 2)\rangle \pm |\phi(2, 1)\rangle$ represent solutions corresponding to positive and negative symmetry with respect to particle exchange.

The situation is a bit more complex for a system with 3 particles. In case the state $|\phi(1, 2, 3)\rangle$ solves the Schrödinger equation, the linear combination:

$$|\phi(1, 2, 3)\rangle + |\phi(1, 3, 2)\rangle - |\phi(3, 2, 1)\rangle \quad (2.30)$$

also solves the Schrödinger equation. For an exchange of particles 1 and 2, this state becomes

$$|\phi(2, 1, 3)\rangle + |\phi(2, 3, 1)\rangle - |\phi(3, 1, 2)\rangle \quad (2.31)$$

The state is not an eigenstate of the permutation operator P_{12} , as it is not the same as the one given in 2.30. Therefore not all solutions of the Schrödinger equation need to be eigenfunctions of the permutation operator. A special case are the linear combinations with negative

$$|\phi(1, 2, 3)\rangle - |\phi(1, 3, 2)\rangle - |\phi(2, 1, 3)\rangle + |\phi(2, 3, 1)\rangle + |\phi(3, 1, 2)\rangle - |\phi(3, 2, 1)\rangle \quad (2.32)$$

and positive

$$|\phi(1, 2, 3)\rangle + |\phi(1, 3, 2)\rangle + |\phi(2, 1, 3)\rangle + |\phi(2, 3, 1)\rangle + |\phi(3, 1, 2)\rangle + |\phi(3, 2, 1)\rangle \quad (2.33)$$

symmetry with respect to particle exchange. These linear combinations are called completely (anti-)symmetric. This means that an application of the permutation operator for any pair of particles gives a negative or positive sign for the state $P|\Phi\rangle = \pm|\Phi\rangle$.

For a general system of N particles, the symmetry of different linear combinations of wave functions are described by *Young diagrams* (see e.g. [8]). A Young diagram represents an irreducible representation of the permutation group ². An example for such diagrams is shown in figure 2.1. Each box of a Young diagram

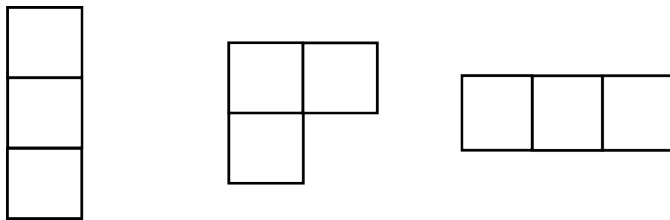


Figure 2.1.: Young diagrams of the S_3 permutation group for antisymmetric (left), mixed (middle) and symmetric (right) permutation symmetry.

symbolizes a particle and the spatial relation of two boxes symbolizes the permutation symmetry of the state with respect to exchange of the particles in the boxes. Two boxes arranged vertically stand for antisymmetric exchange symmetry and two boxes aligned horizontally correspond to symmetric exchange symmetry. From the description of this kind it follows that all states described by a Young

²The permutation group S_N is a group whose elements are the permutations of a set with N elements.

diagram are eigenstates of the permutation operator. In figure 2.1 different exchange symmetries for systems with three particles are shown. It is important to note that there is not only the completely (anti-)symmetric exchange symmetry (left/right side), but also the state with a positive symmetry for the exchange of one pair of particles and negative symmetry for another pair. This state is called a mixed-symmetry state.

The *symmetrization postulate* states that from the 3 different permutation symmetries in figure 2.1, only the left and the right ones are realised in nature [7]. Due to their form they are called the one-dimensional representation of the permutation group. The usual proof of this postulate is like this:

The indistinguishability of identical particles results in the fact that a permutation of two particles should only multiply the wave function only by an insignificant phase factor $e^{i\alpha}$ with α being a real constant.

$$P_{12} |\phi(1, 2)\rangle = |\phi(2, 1)\rangle = e^{i\alpha} |\phi(1, 2)\rangle \quad (2.34)$$

One more application of the permutation operator gives

$$P_{12} P_{12} |\phi(1, 2)\rangle = |\phi(1, 2)\rangle = e^{i\alpha} e^{i\alpha} |\phi(1, 2)\rangle = e^{2i\alpha} |\phi(1, 2)\rangle \quad (2.35)$$

or

$$e^{2i\alpha} = 1 \Rightarrow e^{i\alpha} = \pm 1 \quad (2.36)$$

This proof is incorrect, as it is shown in [8]. One argument against this proof is that the indistinguishability of identical particles only requires the squared norm of the wave function to be invariant under permutations:

$$P_{12} | |\phi(1, 2)\rangle |^2 = | |\phi(1, 2)\rangle |^2 \quad (2.37)$$

For a function to satisfy this relation it is sufficient that it changes under permutations as:

$$P_{12} |\phi(1, 2)\rangle = e^{i\alpha(1,2)} |\phi(1, 2)\rangle \quad (2.38)$$

where 1 and 2 are as in the above formulas the space and the spin coordinates of the two particles. Thus the phase factor can be a function of the permutation and of the coordinates. That means that in general, equations 2.35 and 2.36 do not hold. Consequently the symmetrization postulate states the fact that only the one-dimensional representations of the permutation group meaning the fully (anti-) symmetric states have yet been observed in nature and the solution of the Schrödinger equation can belong to any representation of the permutation group, not only the one-dimensional ones.

2.1.5. Fermions, Bosons and the Spin-Statistics Connection

As mentioned in section 2.1.3, different particles have different intrinsic spin, which cannot be altered. As was shown in 1940 by Wolfgang Pauli [9], the spin of a particle determines which of the two possible representations of the permutation group it belongs to.

Particles with integer spin ($s = 0, 1, 2, \dots$) have symmetric wave functions with respect to particle exchange. These particles are called *bosons* (after Indian physicist Satyendra Nath Bose). Their corresponding Young diagram is of the type on the right side of figure 2.1. Elementary bosonic particles are for example the force carrier particles of strong, weak and electromagnetic interaction: the gluon, the W and Z bosons and the photon. Another example for an elementary boson is the Higgs particle. Composite bosons can be made up out of particles with half integer or with integer spin. Examples for this kind of particles are mesons, which are made up out of two quarks with $s = \frac{1}{2}$.

The occupation number of bosons follows the Bose-Einstein statistics. The expected number of particles in an energy state is in this case:

$$N(E) = \frac{1}{e^{\frac{E-\mu}{kT}} - 1} \quad (2.39)$$

where E is the energy of the state, μ is the chemical potential, k is the Boltzmann constant and T is the absolute temperature. A consequence of this statistics is that more than one bosonic particles can occupy the same quantum state. The commutation relations of creation (a^\dagger) and annihilation (a) operators for bosonic particles in states X and Y are:

$$[a_X, a_Y] = 0 \quad [a_X^\dagger, a_Y^\dagger] = 0 \quad [a_X, a_Y^\dagger] = \delta_{X,Y} \quad (2.40)$$

Particles with half-integer spin ($s = \frac{1}{2}, \frac{3}{2}, \dots$) have antisymmetric wave functions with respect to particle exchange. This means changing the position of two particles multiplies the wave function with a minus sign. These particles are called *fermions* (after the Italian physicist Enrico Fermi). Their corresponding Young diagram is of the type on the left side of figure 2.1. Fermions can be elementary particles like quarks and leptons (e.g. electrons), but also composite particles like neutrons, protons or even atoms.

The occupation number of fermions follows the Fermi-Dirac statistics. The expected number of particles in an energy state is in this case:

$$N(E) = \frac{1}{e^{\frac{E-\mu}{kT}} + 1} \quad (2.41)$$

As the exponential function is always positive, the expected occupation number is always smaller or equal to one. This means that every energy state can only be occupied by one fermion. This is known as the *Pauli Exclusion Principle (PEP)* (see also section 2.1.1). It can be seen that particles with purely fermionic exchange symmetry cannot be in the same state from the considerations of a system consisting of two fermionic particles with two possible states. The unnormalized antisymmetric wave function is:

$$|\Phi_a\rangle = |\phi(1, 2)\rangle - |\phi(2, 1)\rangle \quad (2.42)$$

The wave function for the 2 fermionic particles being in the same state is (in this case in state 1):

$$|\Phi_a\rangle = |\phi(1, 1)\rangle - |\phi(1, 1)\rangle = 0 \quad (2.43)$$

So the antisymmetric wave function of two particles being in the same state is equal to zero. Therefore two fermionic particles can not be in the same state.

The relation described above between a particle's spin and its statistics is called the *Spin-Statistics Connection*. The anticommutation relations of creation (a^\dagger) and annihilation (a) operators for fermionic particles in states X and Y are:

$$\{a_X, a_Y\} = 0 \quad \{a_X^\dagger, a_Y^\dagger\} = 0 \quad \{a_X, a_Y^\dagger\} = \delta_{X,Y} \quad (2.44)$$

From 2.44 it can be seen that adding or removing two particles from a state results in zero (as for example $\{a_X, a_Y\} = a_X a_Y + a_Y a_X = 0$). Consequently not more than one particle can be in the same state for fermions. The action of these operators for fermionic particles on the unoccupied vacuum state $|0\rangle$ and the state occupied by one particle $|1\rangle$ can be written as

$$a|0\rangle = 0 \quad a|1\rangle = |0\rangle \quad a^\dagger|0\rangle = |1\rangle \quad a^\dagger|1\rangle = 0 \quad (2.45)$$

In the literature many proofs for the Spin-Statistic connection exist (e.g. [9], [10]). A clear set of assumptions for this proof was presented by Lüders and Zumino in [11]. The authors present 5 postulates plus gauge invariance as a foundation of their proof:

- Invariance with respect to the proper inhomogeneous Lorentz group (which contains translations, but no reflections)
- Locality - 2 operators of the same field separated by a spacelike interval either commute or anticommute
- The vacuum is the state of the lowest energy

- The metric of the Hilbert space is positive definite
- The vacuum is not identically annihilated by a field

It is worth noting that the mentioned proof also holds for interacting fields. Another interesting point is that the Spin-Statistics connection does not hold for two spatial dimensions. The concept of *anyons*, a class of particles which does not follow bosonic or fermionic statistics, was presented in [12] in this context.

2.2. Theories of Violation of Spin-Statistics

There have been many attempts to find a theory of quantum mechanics which is consistent with a violation of Spin-Statistics. Some of the most important theories will be discussed in the following section.

2.2.1. Parastatistics

The first proper quantum statistical generalization of fermi and bose statistics was done by Green [13], [14]. He noticed that the commutator of the occupation number operator of the state X : $N_X = a_X^\dagger a_X$ with the annihilation and creation operators is the same for fermions and bosons:

$$[N_X, a_Y^\dagger] = \delta_{X,Y} a_Y^\dagger \quad (2.46)$$

As a result, the number operator can be written as:

$$N_X = \frac{1}{2}[a_X^\dagger, a_X]_\pm + const \quad (2.47)$$

The \pm sign denotes the (anti-)commutator for the (bosonic) fermionic case. The expression for the transition operator $N_{X,Y}$, which annihilates a particle in state Y and creates a particle in state X , leads to the trilinear commutation relation ³ for parabose and parafermi statistics:

$$[[a_X^\dagger, a_Y^\dagger], a_Z^\dagger] = 2 \delta_{Y,Z} a_X^\dagger \quad (2.48)$$

These relations have an infinite set of solutions, each of them corresponding to an integer p . The integer p is the order of the parastatistics and gives the number of

³A trilinear form is a function of 3 arguments, in which every argument enters only to first order.

particles that can be in an antisymmetric state in the case of parabosons and the number of particles that can be in a symmetric state in case of parafermions. The case $p = 1$ corresponds to normal fermionic or bosonic statistics. It was shown that the squares of all norms are positive for states satisfying Green's trilinear commutation relation. Nevertheless, the violations introduced by these statistics is large and no precision experiments are needed to rule them out.

2.2.2. The Ignatiev and Kuzmin Model and Parons

In 1987, A. Ignatiev and V. Kuzmin constructed a model of one oscillator with three possible states: a vacuum state with no occupancy, a one particle state and with a small amplitude parametrized by a β a state occupied by two particles [15]. The creation and annihilation operators connect these three states (analogous to 2.45) as:

$$a |0\rangle = 0 \quad a |1\rangle = |0\rangle \quad a |2\rangle = \beta |1\rangle \quad (2.49)$$

$$a^\dagger |0\rangle = |1\rangle \quad a^\dagger |1\rangle = \beta |2\rangle \quad a^\dagger |2\rangle = 0 \quad (2.50)$$

They were able to give trilinear commutation relations for their oscillator. It is worth noting that the authors calculated that the oscillations violating the PEP are suppressed by a factor proportional to β^2 compared to oscillations that do not violate the PEP and vanish for $\beta = 0$. Following these ideas, Mohapatra and Greenberg ([14]) described this model as a modified version of the order-two Green ansatz. They introduced a parameter β giving a deformation of Green's trilinear commutators (see 2.48). For $\beta \rightarrow 1$ the relations reduce to those of the $p = 2$ parafermi field. For $\beta \rightarrow 0$ on the other hand, double occupancy is completely suppressed and fermi theory is obtained. Particles described by this theory were called *parons*. A state of two paronic electrons has the probability to be in a double occupancy state of $\frac{\beta^2}{2}$. It was shown by A. Govorkov in [16] that every alteration of Green's commutation relation (like the one discussed here) necessarily has states with negative squared norms. Thus the model of Igantiev and Kuzmin cannot be extended to become a true field theory.

2.2.3. Quons

The idea of a class of particles called *quons* was described by O. W. Greenberg [17]. The commutator algebra of quons can be obtained as the convex sum of the

fermi and bose commutator algebras

$$\frac{1+q}{2}[a_X, a_Y^\dagger] + \frac{1-q}{2}\{a_X, a_Y^\dagger\} = \delta_{X,Y} \quad (2.51)$$

or

$$a_X a_Y^\dagger - q a_Y^\dagger a_X = \delta_{X,Y} \quad (2.52)$$

In equations 2.51 and 2.52 the parameter q was introduced, which interpolates between a fermionic ($q = -1$) and a bosonic ($q = 1$) commutation relation. For the quonic states to have positive squared norms, this parameter needs to be within $-1 \leq q \leq 1$. For q deviating from ± 1 , the multidimensional representations of the permutation group, which correspond to Young diagrams with more than one row/column, smoothly become more heavily weighted and have a non-zero probability of being realised. That means for a state with two particles, for which only completely symmetric and antisymmetric wave functions are possible, a density matrix ⁴ can be given to represent the mixture of the possible states in the form:

$$\rho = \frac{1+q}{2} |\phi_s\rangle \langle \phi_s| + \frac{1-q}{2} |\phi_a\rangle \langle \phi_a| \quad (2.53)$$

For fermionic quons, the factor q would be close to and slightly larger than -1 . For bosonic quons, the factor q would be close to and slightly smaller than 1 . When the theory of quonic fermions is related to paronic fermions, where the probability of a state with double occupancy is $\frac{\beta^2}{2}$, it follows that

$$\frac{\beta^2}{2} = \frac{1+q_F}{2} \Rightarrow q_F = \beta^2 - 1 \quad (2.54)$$

Quonic particles clearly violate the Spin-Statistics connection. It is worth noting nevertheless, that several properties of relativistic theories do hold, like the CPT theorem for example. But as the Spin-Statistics connection does hold for relativistic theories with the usual properties, some property has to fail. This is the property of locality. It turns out that in this framework, observables separated by spacelike separation ⁵, do not commute.

⁴A density matrix describes a statistical ensemble of several quantum states. This is in contrast to a quantum mechanical mixture of a pure state, described by a state vector.

⁵Points with spacelike separation are not connected by a lightcone and are therefore not causally connected.

2.3. Tests of the Pauli Exclusion Principle

2.3.1. Remarks on Testing the Pauli Exclusion Principle

The question might be asked as to why one should test the PEP and thereby the Spin-Statistics connection, if it can not be violated in a relativistic theory with the usual properties. O. W. Greenberg gives in [14] several “external motivations” which could lead to a possible violation of Spin-Statistics, namely:

- violation of CPT
- violation of locality
- violation of Lorentz invariance
- extra space dimensions
- discrete space and/or time
- noncommutative spacetime

As these items are subjected to active research, it seems plausible also to experimentally test the Spin-Statistics connection. Unfortunately, the level of a possible violation, if it is occurring, is unknown. Also there is no reason, why a possible violation should be as small as experiments find it to be. Another important point when testing the PEP is that one does not search for fermions which are “a bit” different. If this kind of slightly different fermions would exist, the lowest order pair production cross section would double [14]. This is clearly ruled out by experiments. Because of the indistinguishability of identical particles, all fermions should have the same possibility for an admixture of a symmetric state. This is reflected in the use of the density matrix for the description of states in the case of quons.

2.3.2. Experiments for Testing the Pauli Exclusion Principle

According to S. R. Elliott, the various experiments testing the Pauli Exclusion Principle can be grouped into three classes [18], with respect to the kind of fermionic interaction they are investigating:

- Type 1: interactions between a system of fermions and a fermion that has not yet interacted with any other fermion
- Type 2: interactions between a system of fermions and a fermion that has not yet interacted with this given system
- Type 3: interactions between a system of fermions and a fermion within this system

These distinctions between different interactions are necessary due to the MG superselection rule (see also section 2.1.4). This rule forbids changes of the permutation symmetry of a quantum state in a system where the number of particles is constant. The important difference among these classes is that in a type 3 interaction, the superselection rule forbids a change in permutation symmetry as the investigated fermion already has a defined permutation symmetry with the surrounding system and the number of particles in the system does not change. Subsequently the different types of experiments will be discussed and examples will be given:

Type 1 experiments:

The typical experiment of this type uses recently created fermions and lets them interact with the system under investigation. In 1948 Goldhaber and Scharff-Goldhaber [1] produced electrons with a β source and let them capture on Pb atoms. The authors idea was that if the electrons from the β source are not subject to the PEP in the electron shell of the Pb atoms, they could cascade to the ground state and thereby emit photons which would be detected. The lack of these photons was used to set an upper limit on the probability for the violation of the PEP. The fundamental point is that the electrons from the β source have not yet interacted with any system and are therefore necessarily new to the electronic system of the Pb atoms. As they are new to this system, they can form new quantum states with the Pb atoms. Forming states with a symmetric admixture is not forbidden by the MG superselection rule in this case. This is also true, if the electronic state of the atom has previously been in a completely antisymmetric state. Other sources of recently produced fermions can also be pair-production processes and nuclear reactions.

Type 2 experiments:

In this kind of experiments, fermions are brought to a system to interact with it. These fermions have not recently been created, but they have not previously interacted with the system. The typical experiment is the one conducted by Ramberg and Snow [2]. In this experiment, electrons were introduced to a Cu conductor via a current. These current electrons have no previous interaction with the atoms in the conductor. Therefore the same arguments apply as for type 1 experiments and the formation of a state with an admixture of symmetric exchange symmetry between the atoms of the conductor and a conduction band electron is not forbidden by the MG superselection rule.

In case of a symmetric admixture in a quantum state formed between an atom in the conductor and the current electrons, the current electron could cascade to the ground state, thereby emitting photons. The lack of detected photons was used to set an upper limit on the probability for the violation of the PEP. An interesting point is the precise origin of the electrons in the conduction band. In an optimal setup, they are coming from a battery. This would guarantee the newness of the electrons. The drawback is that a high current is hard to maintain in this way. If the power of the current source comes from an AC grid the electrons in the conduction band of the conductor will comprise electrons from the conductor itself and the circuitry connecting it to the power supply.

An interesting idea was put forward by E. Corinaldesi [19], who suggested that the PEP is not a kinematic principle but rather a time-dependent effect of interactions and that newly formed system may undergo PEP violating transitions, whose rate decreases with time. This suggestion could be tested with a type 2 experiment. In [20] it was suggested that this hypothesis can be tested by crossing an electron and a Ne^+ ion beam, and to monitor potential photons from PEP violating transitions.

Type 3 experiments:

A type 3 experiment searches for a PEP violating transition in a stable fermionic system where the number of particles is constant. Notably the considered systems need to change their permutation symmetry in order to undergo these transitions. Therefore type 3 experiments violate the MG superselection rule and their outcome can not be compared to type 1 and type 2 experiments.

Nevertheless, many experiments of this kind have been conducted. Pioneers in this

kind of experiment were Reines and Sobel [21]. They were looking for transitions of L-shell electrons to the already occupied K-shell in iodine atoms. The DAMA/LIBRA experiment conducted an analysis of their data regarding the same process [22]. Nuclear processes were also investigated regarding PEP-violating transitions, for example in [23] by the Borexino collaboration. The experimenters were looking for non-Paulian transitions of nucleons from the 1p to the 1s nuclear shell.

Anomalous Structures

Another type of experiment is to look for anomalous nuclear and atomic structures. In [24] an experiment is reported where nuclear states with three nucleons in the 1s ground state are searched. Non-Paulian atomic states of Be are explored in [25].

Some limits on the probability of a violation of the PEP are summed up in table 2.3.2.

Process	Type	$\frac{\beta^2}{2}$ limit	Reference
anomalous atomic transition	1	3×10^{-2}	[1]
anomalous atomic transition	2	4.7×10^{-29}	[4]
anomalous atomic transitions	3	6.5×10^{-46}	[22]
anomalous nuclear transitions	3	2.2×10^{-57}	[23]

The most stringent limit prior to the VIP2 experiment in a system circumventing the MG superselection rule (type 1 + 2 experiments) is set by the VIP experiment [4]. The experimental method of the VIP and VIP2 experiments will now be described.

2.4. The VIP2 experimental method

As mentioned in section 2.3.2, the change of permutation symmetry of a quantum state is not forbidden by the MG superselection rule, when a fermion, which is new to the studied system (e.g. atom, nucleus), interacts with it. These types of experiments were classified as type 1 and type 2. To the best of our knowledge, the most feasible way to introduce a large number of fermions into a system is by introducing a current into a conductor. The number of electrons introduced in this way is for 1 A $\sim 10^{19}$ per second. While moving through the conductor

with a velocity influenced by the applied electric potential, these electrons have a certain probability to interact with the atoms in the conductor. Due to this interaction, the electrons from the conduction band can form a new quantum state with the electrons in the atom. It is important to mention that the electrons in the conduction band did not have a defined symmetry with respect to the atomic electrons before this interaction happens, as they come from the current source outside of the conductor. This formation of a new quantum state is the reason why this kind of experiment does not violate the MG superselection rule. After the formation of the new state, the former current electron has the possibility to have symmetric permutation symmetry with respect to particle exchange with the other electrons in the electron shell if the PEP can be violated. This electron sees all the states occupied by the atomic electrons as empty and can occupy them. Therefore it will cascade down into the 1s ground state of the atom, emitting photons as it loses energy. These photons are collected for some time with and without a current. As there are no new electrons introduced during the measurement without current, there are also no photons expected in this time. This measurement is used to determine the background of the energy spectrum. From the difference between the energy spectra in the energy regions where one expects photons from the PEP violating transitions, one can calculate the probability for a violation of the Pauli Exclusion Principle in an atom, or set upper bounds for this probability.

For the VIP2 experiment the conducting material is copper (Cu). It has the atomic number 29 and is part of the group 11 in the periodic table of elements together with for example silver (atomic number 47) and gold (atomic number 79). A common feature of these elements is that they are good conductors for electrical currents. Copper has a resistivity at room temperature of $1.68 \times 10^{-8} \Omega m$, silver has $1.59 \times 10^{-8} \Omega m$ and gold has $2.44 \times 10^{-8} \Omega m$, making silver the best conductor of them. Due to its low cost, copper was the obvious choice for this experiment. The mentioned elements are good conductors due to the unpaired electron in the outermost s-shell. The electronic configuration for copper for example is [Ar] $3d^{10}4s^1$. The Fermi energy ⁶ overlaps the 4s orbital [26]. It is a broad band ⁷ which resembles the dispersion relation of free electrons. At finite temperature the electrons of the 4s orbital can move freely in this band (i.e. change their momentum) and be the carrier of the current.

The energies of the mentioned cascading process were calculated for copper atoms in [27] using a self-consistent multiconfiguration Dirac-Fock (MCDF) approach.

⁶The Fermi energy is the energy of the highest occupied energy state of a system at a temperature of 0 K.

⁷An energy band in a solid is a region of allowed states in a $E(\vec{k})$ diagram. Here E is the energy and \vec{k} is the wave vector.

In this case self-consistent is best explained with the help of figure 2.2. It means

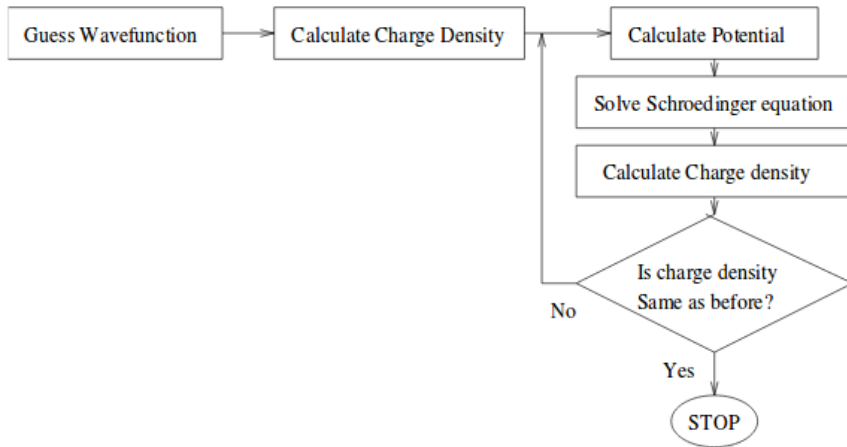


Figure 2.2.: A self-consistent algorithm for calculating the energy of atomic states.

after calculating the potential from a charge density at any step and solving the Schrödinger equation with it, the charge density calculated from the Schrödinger equation needs to be the same as the initial charge density. The term “multi-configuration” comes from the fact that the total wave function is described as a linear combination of configuration state functions, which are related to a specific configuration of electrons. Using the Dirac-Fock approach as opposed to the Hartree-Fock means that relativistic effects are accounted for. The relativistic Breit-Dirac Hamiltonian is used which takes into account all electromagnetic interactions of spin $\frac{1}{2}$ particles including spin-orbit coupling and retardation effects. After self-consistency is achieved, the total energy is corrected by vacuum polarization effects (self energy and vacuum polarization). In the whole procedure the “no pair” approximation is applied which explicitly excludes electron positron pairs.

The original code for this calculation, which was later adapted for the use of the VIP2 experiment, was described in [28]. It calculates the energies of atomic states in an electronic shell in which all but one electron have antisymmetric exchange symmetry. These states violate the PEP. The working principle of the calculation was described as a three step process in [29]:

- Step 1: The functional form of the wave function is selected and defined in terms of certain functions (mostly hydrogen-like wave functions) which are combined with certain parameters.
- Step 2: An expression for the total energy is derived in terms of these functions and parameters.

- Step 3: The variational principle is applied and equations are derived for the valid solutions that are the functions that leave the total energy stationary. In this step self-consistency is checked.

The total wave function must then also obey the Hartree-Fock assumptions, for example that the wave function is antisymmetric with the exception of the one electron which has symmetric exchange symmetry. Furthermore, the total wave function needs to be an eigenfunction of the L^2, L_z, S^2 and S_z operators. The results of these calculations for copper are summed up in table 2.1.

Transition	Transition energy - PEP violating (eV)	Transition energy - normal (eV)	Radiative transition rate (s^{-1})	Multipole Order
$2p_{\frac{3}{2}} \rightarrow 1s_{\frac{1}{2}}$ ($K_{\alpha 1}$)	7748	8048	2.56×10^{14}	E1 + M2
$2p_{\frac{1}{2}} \rightarrow 1s_{\frac{1}{2}}$ ($K_{\alpha 2}$)	7729	8028	2.63×10^{14}	E1
$3p_{\frac{3}{2}} \rightarrow 1s_{\frac{1}{2}}$ ($K_{\beta 1}$)	8532	8905	2.68×10^{13}	E1 + M2

Table 2.1.: Transition rate and energies for PEP violating transitions in copper calculated with the MCDF algorithm [27].

It is interesting to note that while for normal transitions the $K_{\alpha 1}$ transitions has twice the intensity of $K_{\alpha 2}$, the corresponding PEP-violating $K_{\alpha 2}$ has a slightly higher intensity. This is why for future calculations the energy value of the PEP forbidden $K_{\alpha 2}$ line of 7729 eV will be used. Furthermore, as the transition rate of the K_{β} is lower by one order of magnitude, the primary focus of the analysis will be on the K_{α} transitions. Due to the angular momentum selection rules ⁸, the 2s - 1s transition is forbidden, which also holds true for PEP forbidden transitions.

The difference in the transition energies between the normal K-lines and the PEP forbidden K-lines listed in table 2.1 can be explained with figure 2.3. On the left side of the figure a normal 2p to 1s transition is shown. In this transition an electron

⁸The conservation of angular momentum demands $|J_i - J_f| \leq \lambda \leq J_i + J_f$, where $J_{i,f}$ are the initial and final total angular momenta and λ is the photons angular momentum. $\lambda = 0, 1, 2, \dots$ for electric and magnetic monopole, dipole, quadrupole, ... transitions. The change of parity for electric transitions is $(-1)^\lambda$ and for magnetic transitions it is $(-1)^{\lambda+1}$, which ensures the conservation of overall parity. The parity of a state is $(-1)^L$, so it does not change from 2s to 1s. As for electric dipole transitions the parity needs to change, it is electric dipole forbidden.

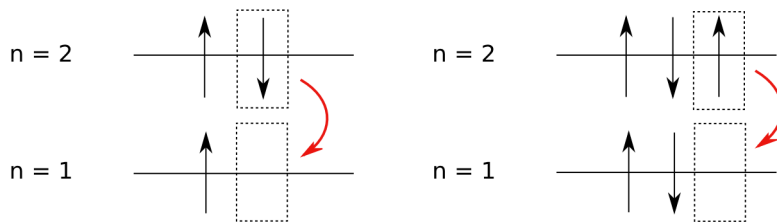


Figure 2.3.: Scheme of normal 2p to 1s transition (left) and a 2p to 1s transition which is violating the PEP (right).

from the 2p shell fills a vacancy in the 1s ground state, thereby losing 8048 eV of energy in the form of a photon. On the right side the corresponding PEP violating transition is shown. The electron undergoing the transition cascades down from the 2p into the 1s shell, but in this case, the 1s shell is occupied with 2 electrons. This is only possible because of the symmetric admixture in the symmetry of the wave function. The two electrons in the 1s ground state shield the core potential more than the one electron in the case of the normal transition. Thereby they reduce the effective nuclear charge, which causes the transition energy to be lower for this transition. In the case of the K α transition for copper, the difference in energy is around 300 eV.

3. The Measurement Setup

As mentioned in chapter 2, the core functionality of the VIP2 experiment is to measure energy spectra in the energy region where the PEP violating K α transition is expected. For this purpose Silicon Drift Detectors are used. They offer an energy resolution good enough for our purpose of separating the energy peak coming from photons from allowed transitions from those coming from PEP-forbidden transitions. These transitions are separated by 300 eV. Furthermore they offer a time resolution $< 1 \mu\text{s}$. This allows the use of an active shielding system, which consists of 32 plastic scintillator bars arranged around the copper target and the SDDs. They are read out by Silicon Photomultipliers. The working temperature of the SDDs was around 100 K. Their temperature was kept constant by a system composed of a helium compressor liquefying argon, which in turn cooled the detectors. A data acquisition and a slow monitor system were in place to collect data and monitor crucial parameters of the experiment. A schematic drawing of the experiment is shown in figure 3.1. All these components will now be described in detail.

3.1. Silicon Drift Detectors and copper target

Silicon Drift Detectors (SDDs) are used in the VIP2 experiment as X-ray detectors. They are mounted as close as 5 mm away from the Cu target in the setup, to reach maximum solid angle coverage.

The Cu target consists of 2 strips with a length of 7.1 cm, a width of 2 cm and a thickness of 50 μm . The strips are connected to a current supply via Cu connectors. In between the 2 strips runs a water cooling line to keep them at a constant temperature even with a high current flowing through them. One SDD array with 3 individual cells is mounted on each side of the target strips.

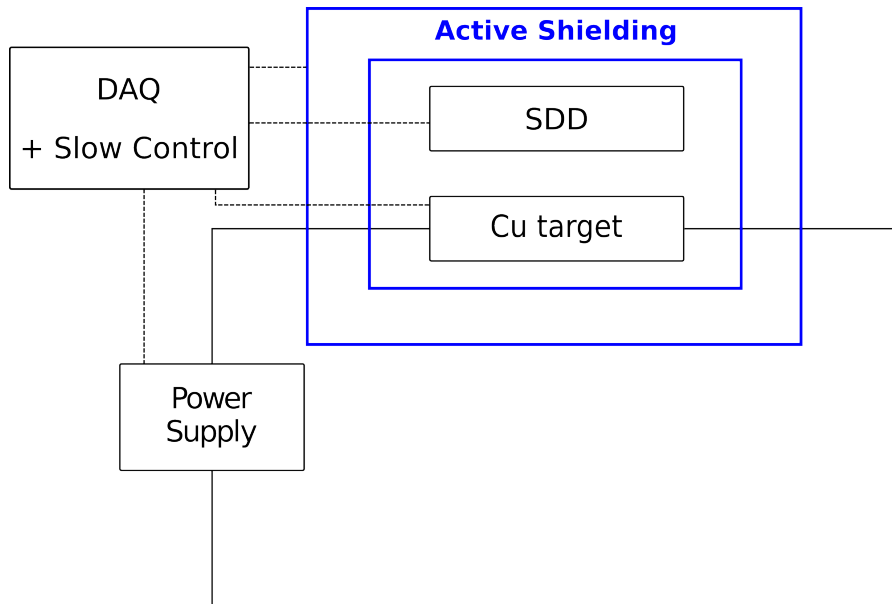


Figure 3.1.: Schematic drawing of the VIP2 experiment.

3.1.1. Working principle

The working principle of Silicon Drift Detectors is based on sideward depletion, which was first introduced in [30]. A schematic drawing of an SDD used for the VIP2 experiment is shown in figure 3.2. On a cylindrical n-type¹ silicon wafer circular p⁺-type silicon contacts are implanted on one flat surface. These contacts are used to apply an increasing reverse bias in order to fully deplete the wafer. The radiation entrance windows is on the opposite side of the concentric contacts and consists of a homogeneous shallow junction, which gives homogeneous sensitivity over the whole surface. When ionizing radiation hits the silicon wafer, electron-hole pairs are generated. The free electrons fall to the lowest point of the potential produced by the concentric electrodes. This lowest point is the anode consisting of a ring close to the middle of the wafer. The amount of electrons generated in the wafer and collected by the anode is proportional to the energy of the radiation. By measuring the amount of charge collected this energy can be calculated. The small size of the anode ensures a small anode capacitance, which is almost independent of the size of the detector [32] and only proportional to the anode's size. As some sources of noise are proportional to the capacitance ????, this reduces the

¹n-type semiconductors are doped with elements that are pentavalent, like phosphorus. This results in an excess of electrons. p-type semiconductors are doped with trivalent elements like boron, which results in an excess of holes.

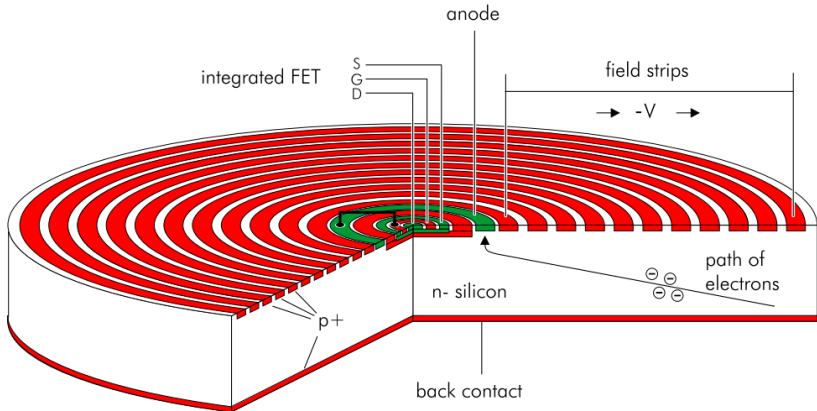


Figure 3.2.: Scheme of a Silicon Drift Detecor [31].

noise and allows shorter shaping times ² which in turn allows high count rates. As a first stage of amplification, a field effect transistor (FET) ³ is integrated in the chip and connected to the anode by a metal strip. Thereby the capacitance between detector and amplifier is minimised and electric pickup noise is mostly avoided. The anode is discharged continuously. This avoids regular dead times of the detector by a repeating reset mechanism.

3.1.2. SDD specifications for the VIP2 experiment

sources of noise -> expected energy and time resolution as a function of temperature

The manufacturer of the employed detectors (PNSensors) produced a manual, from which the information in this section is mainly taken [31]. The SDDs employed in the VIP2 experiment are 2 arrays with 3 detector cells each. Each cell has an active area of 1 cm^2 shaped like a “rounded square” with a diameter of 10.3 mm and a corner radius of 2 mm. The maximum drift path length for electrons originating in a corner is 6.4 mm. The cells have a thickness of 450 μm , which ensures a absorption of $\sim 99\%$ of 8 keV (Cu K α line) X-rays. The 3 cells in an array share a common outermost strip (Rx), a common bulk contact (outer

²Long shaping times can be used in order to cancel out noise.

³A field effect transistor controls the conductivity between the source (S) and the drain (D) via an electric field between the body and the gate (G) of the device.

substrate - Os) and common guard ring systems on both sides of the chips. Each cell has a readout structure in its center and individual back contact (Bc) and separation mesh (back frame, Bf) contacts. The bonding and the way the voltages were adjustable were modified slightly for the VIP2 experiment. The important contacts and the way the respective voltages are adjustable (all SDDs common, all SDDs in an array, each individual SDD cell) are shown in table 3.1. Plots of the front and the back side of the arrays are shown in 3.3 and 3.4. There is a

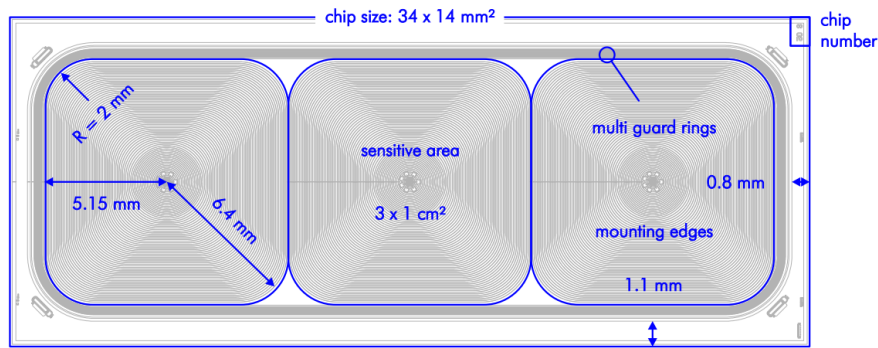


Figure 3.3.: Front side of the SDD array of the VIP2 experiment [31].

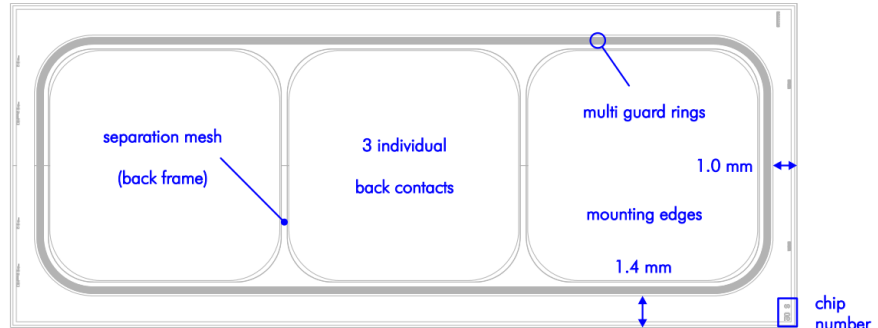


Figure 3.4.: Back side of the SDD array of the VIP2 experiment [31].

total number of 74 concentric electrodes, where the innermost 23 are circular and the ones more on the outside are linear in vertical and horizontal direction with rounded edges. The first and the last ring are biased externally, the others are supplied via a resistive voltage divider.

Contact Name	Abbreviation	Bonding	Nominal Value [31]
Outermost strip	Rx	Common	-240 V
Innermost strip	R1	Common	-15 V
Outer substrate	Os	Common	GND
Inner substrate	Is	Common	GND
Entrance Window	Bc	Cell	-120 V
Separation Mesh	Bf	Array	-140 V

Table 3.1.: Some important contacts of the Silicon Drift Detectors used for the VIP2 experiment.

3.1.3. Silicon Drift Detectors performance characteristics

The energy and time resolution as well as scale linearity are crucial factors in the performance of the SDDs. The possibility of a high event rate would be another point to consider, but as this is not an issue for the VIP2 experiment with count rates of ~ 2 Hz, this point will not be discussed.

The detector linearity is the ratio between produced electron-hole pairs and energy as a function of energy. In case the whole energy of the incident radiation is deposited in the detector and no losses during the charge transport, the number of electrons arriving at the anode only depends on the energy. Consequently the detector response should be perfectly linear with energy.

An advantage of semiconductor detectors with respect to gaseous detectors is the lower energy needed to create an electron-hole pair. At 77 K, this energy is 3.81 eV [33], which is independent of the type and energy of the incident radiation. The amount of charge carriers produced by the same radiation will therefore be one order of magnitude higher than in gaseous detectors. Therefore, semiconductors provide a greatly enhanced energy resolution. On the other side, the energy resolution is limited by noise. One part is the so-called fano noise. It results from a non-constant amount of electron-hole pairs produced for different events with the same energy. The fano factor is defined as:

$$F = \frac{\sigma^2}{\mu} \quad (3.1)$$

Here σ^2 is the variance of the number of produced electron-hole pairs and μ is the average of the number of electron-hole pairs. It is not dependent on energy and for Silicon the value is estimated to be $F = 0.12$ [33]. Another source of noise is the leakage current, which is a small fluctuating current flowing through semiconductor

junctions in case of an applied voltage. The fluctuation in the current appears as noise in the detector. One source of leakage current are thermally created electron-hole pairs originating from recombination and trapping centers in the depletion region. These centers result from impurities in the crystal. This part of the noise can be suppressed by lowering the temperature. Another source of leakage current are surface currents.

In order to reach the best possible energy resolution, an Fe-55 source ⁴ is installed in the VIP2 setup. The photons from the source hit the SDDs directly and also induce K α transitions in a titanium foil located between the source and the detector. These 2 photon sources enable continuous calibration of the energy scale and thereby minimize peak drift effects and optimize the energy resolution.

The time resolution of the SDDs is determined by the drift time of the electrons from their origin to the anode. In [31] the maximum drift time at 150 K for the type of detector used in the VIP2 experiment is estimated to be 600 ns. Due to the temperature dependence of the electron mobility (e.g. increased phonon scattering), the time resolution generally gets worse with rising temperature.

3.2. Active Shielding

how light propagates -> reflectivity -> wrapping; physics of interaction with different radiations maybe in simulations

The active shielding system has the purpose of rejecting SDD events caused by external radiation. This means that whenever a signal in the SDDs is in coincidence with a signal from the scintillators, it can be rejected. The active shielding consists of 32 scintillators read out by 2 Silicon Photomultipliers (SiPMs) each, which are assembled around the copper target and the SDDs. A render of the setup including the active shielding system enclosing the target is shown in figure 3.5.

3.2.1. Scintillators

Scintillators are materials that emit photons after they are excited by ionizing radiation. The scintillators used in the VIP2 experiment are plastic scintillator

⁴An Fe nucleus with 26 protons and 29 neutrons decays via electron capture to Mn-55 with a half-life of 2.737 years. This results in the emission of a photon or an Auger electron.

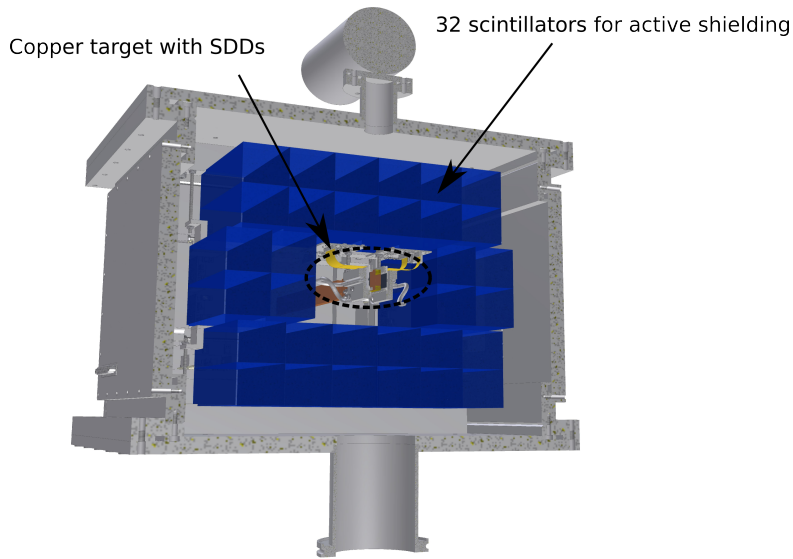


Figure 3.5.: Active shielding system of the VIP2 experiment consisting of 32 scintillators.

bars of the type EJ-200 produced by Eljen Technologies. Their dimensions are 38 mm x 40 mm x 250 mm. The base polymer is polyvinyl toluene [34]. When ionizing radiation passes through the scintillator, electrons in the valence band in so-called molecular orbits are excited [33]. Subsequently the excited states loose their energy via the emission of a photon. A flour is suspended in the polymer matrix to absorb the UV radiation and re-emit it at visible wavelengths. The wavelength of maximum emission is then 425 nm (blue light) and the pulse width is 2.5 ns (FWHM) [34]. The scintillation material has a refractive index of 1.58, meaning that total internal reflection can occur for photons with a flat impact on the surface. Nevertheless light can also escape the scintillator if the impact angle is too steep. To increase the light collection on the SiPMs, the scintillators were wrapped in reflective aluminum foil to reflect stray photon back into the scintillator, while leaving a small air gap in between the foil and the scintillator. To minimize the influence of photons from the environment hitting the SiPMs, a layer of sticky black tape was wrapped around the aluminum foil.

3.2.2. Silicon Photomultipliers

A Silicon Photomultiplier consist of an array of semiconductor pn junctions with a high reverse bias. For the VIP2 experiment, we use the $3 \times 3 \text{ mm}^2$ ASD-SiPM3S-P50 SiPMs manufactured by AdvanSiD. On one end of each scintillator bar, 2

SiPMs are attached with optical glue ??? and connected in series. In that way, as opposed to reading both SiPMs individually, the signal to noise ratio and the time resolution can be improved ??. One SiPM consists of 3600 sequentially connected Silicon avalanche photodiodes (APD) with an area of $50 \times 50 \mu\text{m}$ each. All of them are operated in Geiger mode (an analogy to the Geiger counter), meaning that the reverse bias voltage is higher than the breakdown voltage ⁵. In this mode, the generation of one charge carrier causes an avalanche of charge carriers due to impact ionization. The first charge carrier can be produced by an incident photon undergoing the photoeffect. In the case of the VIP2 experiment, this photon comes from the scintillator. The energy of the optical photons from the scintillator (425 nm \sim 2.9 eV) is enough to generate an electron-hole pair. The spectral response range for the SiPMs used for VIP2 is 350 nm - 900 nm [35], overlapping with the photon spectrum of the scintillator. One APD by itself is a digital device, as it can only decide if a photon hit it or not. Reading all APDs in a SiPM at the same time gives then an analog signal.

The time resolution of a system of scintillator read out by SiPMs is typically on the order of a few ns. This means that it is negligible compared to the time resolution of the SDDs, which is of the order of a few 100 ns.

3.3. Cooling system

he compress: compresses (9.8 bar \rightarrow 22 bar) and cools (warms up due to compression) (to room temp or so) the he gas; also filters out oil mist in the gas in an adsorber and an oil separator \rightarrow + PID control

The Silicon Drift Detectors used for the VIP2 experiment have a working temperature of around 150 K [31]. To reach this temperature, a system of a helium compressor coupled to a pulse-tube refrigerator is used with helium gas as a working medium. The cooling power produced by this system is used to liquefy Argon, which then flows past the SDDs. Thereby it evaporates and cools the detectors down.

As a helium compressor a CNA-21A helium compressor from SHI - (Sumitomo Heavy Industries -) cryogenics was used. This compressor gets \sim 9.8 bar helium gas at room temperature from the cold head. This gas is then compressed to \sim 22 bar and cooled back down to room temperature after it was heated due to the

⁵The breakdown voltage of a diode is the minimum reverse bias voltage to make the diode conductive.

compression. The compressor is air-cooled meaning the helium gas flows through a heat exchanger after compression which is cooled by blowing air with a fan through it. The high pressure helium gas at room temperature is then supplied to a pulse tube refrigerator of the Gifford-McMahon type. The working principle of this type of refrigerator is shown in figure 3.6. The high pressure helium gas is connected

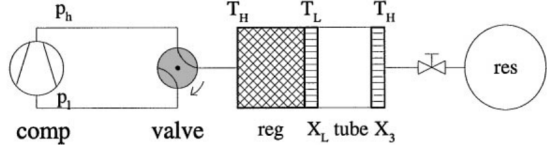


Figure 3.6.: Schematic drawing of a pulse tube refrigerator of the Gifford-McMahon type [36].

to the RP-2620A coldhead which is also manufactured by SHI - cryogenics. The cold head has a valve on its side close to the helium compressor. This valve connects the refrigerator to the high and the low pressure side of the compressor in an alternating way. Coming from the high pressure side of the compressor, the gas first hits a regenerator, at a high temperature (\sim room temperature) T_H . After the regenerator, there is a heat contact X_L to the medium to be cooled at the lower temperature T_L . Thereafter follows the pulse tube where the gas is thermally isolated (adiabatic) and therefore the temperature of the gas depends on its pressure. After the pulse tube a thermal contact to the surroundings is installed. The whole gas volume is coupled to a gas reservoir via a flow resistive valve. The heat exchangers, the regenerator and the pulse tube are suspended in vacuum of $\sim 10^{-5}$ - 10^{-6} mbar.

When the high pressure helium gas flows through the regenerator, it is cooled down to T_L and the regenerator is warmed up to T_H . The gas enters the pulse tube at T_L . Then the pressure is switched to the low pressure of around 10 bar in our case, and the gas flows out of the tube. But due to the lower pressure, the temperature in the tube is now lower than T_L . The gas now flows through the thermal contact X_L . It cools the contact and thereby effectively cools the argon gas X_L it is in thermal contact with. The helium gas then flows through the regenerator at exactly T_L , cooling it to this temperature. The opposite effect occurs at the temperature T_H at X_3 , where heat is dissipated to the environment. The coefficient of performance (ratio between cooling power and compressor power) for an ideal pulse tube refrigerator is $\frac{T_L}{T_H}$, which is lower than the one of a Carnot process $\frac{T_L}{T_H - T_L}$ due to losses in the valve [36].

The cooling power of the pulse tube refrigerator at X_L is used to cool down an aluminum target through which the argon gas flows. The argon condenses and

flows down a pipe which runs past the SDDs, cooling them to their working temperature. Thereby the argon evaporates. Afterwards it is cooled again by the pulse tube refrigerator. A picture of the SDDs with the argon cooling line and a readout board is shown in figure 3.7.

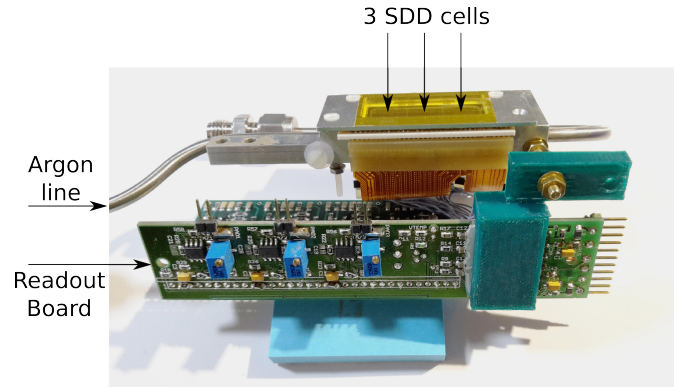


Figure 3.7.: The SDDs with the argon cooling line and the readout board.

The cooling of the pulse tube refrigerator is counteracted by a heating wire controlled by a LakeShore 331 temperature controller. This is done in order to be able to control the temperature of the argon by adapting the heating power. Changes in argon temperature can in this way be compensated with the PID (Proportional Integral Differential) control of the LakeShore 331 on a very short timescale. The vacuum necessary to maintain the necessary cryogenic temperatures is maintained by 2 turbo pumps connected to a common prepump.

3.4. Data acquisition and slow control systems

3.4.1. Signal readout and data acquisition

vme readout; simplified logic without timing = trigger; preamp board?; shaping time and gain of SDDs?; thresholds of sipms - maybe only that we can set them - how big they are -> out into chapter test measurements;

After a first stage of amplification in the preamplifier board in the vacuum chamber, the signals of the 6 SDDs go into a programmable CAEN 568B spectroscopy amplifier. The fast “FOUT” signal goes to a discriminator for making a trigger. An OR of all 6 discriminated SDD signals is going to a CAEN V1190B TDC (Time

to Digital Converter). The programmable “OUT” output of the amplifier is used for spectroscopic signal analysis. The spectroscopic signal is fed into a CAEN V785 peak sensing ADC (Analog to Digital Converter) for digitalizing the signal.

The signal from the 2 SiPMs from each of the 32 scintillators is amplified in a preamplifier board in the vacuum chamber. The analog signal is split thereafter, with one part going to a programmable Constant Fraction Discriminator (CFD) to make a timing signal and the other going to a CAEN V792 QDC (Charge to Digital Converter). Referring to figure 3.5, the 32 scintillators can be grouped into one “outer” one “inner” layer, and more specifically into 8 sub-layers with the indication of their position relative to the target (e.g. “top outer” layer indicates the 8 scintillators above the target, which are closer to the setup box). A signal of one of these layers is an OR of all the discriminated SiPM signals in this layer. The signal of each of these 8 sub-layers and an AND of the outer and inner layer is sent to the TDC.

The digital signal from the discriminators is used for making a trigger for the TDC, ADC and QDC modules. The trigger logic is shown in figure 3.8. It consists of the OR of all 6 SDDs making an OR with the inner AND outer scintillator layer. The AND of the inner and outer scintillator layer triggers on cosmic radiation or

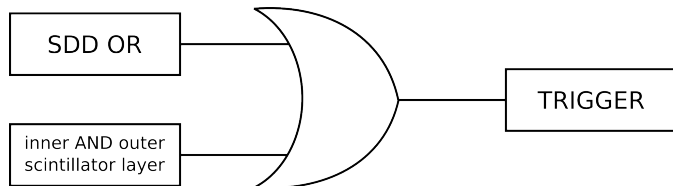


Figure 3.8.: Trigger definition of the VIP2 experiment.

any radiation which produces a detectable signal with high probability in every scintillator it passes through. The OR of the SDD signals includes every SDD event above a certain energy threshold. Also in the case of SDD only trigger (no scintillator AND), the signals (or lack thereof) of all 8 scintillator layers is recorded in the TDC.

The data from ADC, QDC and TDC are read out via a CAEN V2718 VME - PCI bridge to a CAEN A2818 PCI controller. A LabView program is communicating with this controller to record and store the data in binary form.

3.4.2. Slow control

all the values read out/ controlled by slow, and how they are read; also with plugbars

The slow control is a system to monitor and control important parameters of the experiment. A schematic drawing of its layout is shown in figure 3.9. The central

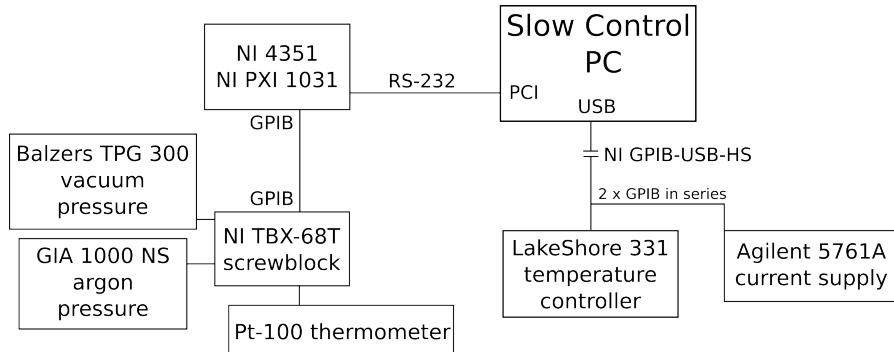


Figure 3.9.: A schematic layout of the slow control system of the VIP2 experiment.

point of the system a PC running a Visual C++ program which communicates with the different sensors and devices via a GPIB and a USB interface and stores the parameter values. The PC can be accessed remotely to control parameters and transfer the stored data. The USB interface is on the one hand connected to a LakeShore 331 temperature controller which regulates the heating of a wire which counteracts the cooling of the cold head and thereby regulates the argon temperature. On the other hand it is connected to an Agilent 5761A current supply which provides the current through the copper target. The GPIB interface is connected to a National Instruments (NI) PXI 1031 chassis with a NI PXI 4351 board. This is then connected via GPIB to a NI TBX-68T screwblock which receives analog signals from several sources, which correspond to pressure and temperature at different points in the setup. Temperature information comes from Pt-100 resistance thermometers and pressure readings come from a cold cathode⁶ for low pressure and piezoresistive sensors⁷ for high pressure. A list of all parameters that can be measured and controlled with the slow control system can be found in table 3.2.

⁶A cold cathode generates electrons via the discharge of a high voltage. The electrons ionize the gas and the number of produced ions is proportional to the gas pressure.

⁷The piezoresistive effect causes the resistance of a material to change under mechanical strain.

All the values listed in this table are stored periodically. An emergency system was in place which periodically checks the values recorded by the slow control. In case specific values exceed certain thresholds, crucial systems like the turbomolecular pumps and the SDDs could be turned off automatically. This was done by the communication with an Energenie EG-PM2-LAN plug which allows the automatic power shutdown of these devices which were attached to it.

Value to measure / control	Measured / Controlled by	Primary readout device	Adjustable
Room temperature	Pt-100	NI PXI 4351	No
Copper bar external temperature	Pt-100	NI PXI 4351	No
Copper bar internal temperature	Pt-100	NI PXI 4351	No
Water cooling pad temperature	Pt-100	NI PXI 4351	No
PCB board 1 temperature	Pt-100	NI PXI 4351	No
PCB board 2 temperature	Pt-100	NI PXI 4351	No
SDD 1 temperature	Pt-100	NI PXI 4351	No
SDD 2 temperature	Pt-100	NI PXI 4351	No
Argon upper line temperature	Pt-100	NI PXI 4351	No
Argon lower line temperature	Pt-100	NI PXI 4351	No
Argon target temperature	Pt-100	NI PXI 4351	No
Argon gas temperature	Pt-100	NI PXI 4351	No
Vacuum pressure	Balzers IKR 050 cold cathode	Balzers TPR-010	No
Argon gas pressure	Keller PAA-21-10	GIA 1000 NS	No
Heater output power	LakeShore 331	LakeShore 331	No
Heater PID settings	LakeShore 331	LakeShore 331	Yes
Argon gas set temperature	LakeShore 331	LakeShore 331	Yes
Current through copper	Agilent 5761A	Agilent 5761A	Yes

Table 3.2.: Summary of parameters measured and controlled by the slow control system.

4. Simulations

geant4 simulations of: the background rejection ratio for cosmics and for gammas; the energy deposition of MiPs in scintillators; the efficiency determination for detecting photons coming from PEP violating transitions

For the purpose of evaluating and verifying several experimental parameters, the complete setup has been modeled in the Geant4 framework [37]. The utilized version of the framework is Geant4.10.2 . All components of the setup were considered in the simulations including the SDDs with metal frames, the copper target and the copper current supply cables, the scintillators and the calibration foils as well as the aluminum vacuum box. The PENELOPE (PENetration and Energy LOss of Positrons and Electrons) model was chosen over the LIVERMORE model for electromagnetic processes. As atomic de-excitation processes were important, fluorescence, auger electron emission and PIXE (Particle induced X-ray emission) were turned on. The simulations were conducted by the collaborator Shi Hexi. A render of the setup is shown in figure 4.1.

4.1. Detection Efficiency of PEP-violating Transitions

One objective of the simulation was to determine the efficiency of the setup. The efficiency is in our case defined as the probability for an X-ray coming from a PEP violating transition (i.e. a photon with an energy of 7.7 keV) originating in one of the two target strips to be detected in a SDD. Two factors contribute to the efficiency. On the one hand the solid angle coverage of the copper target by the SDDs limits the efficiency. Taking into account the fact that the aluminum pad for water cooling between the two copper foils absorbs ~100 % of these photons, the solid angle can be estimated to be ~ 10 % (from the ratio between the area of the target and the area of the SDDs). On the other hand some photons are lost by interactions with the 50 μm Cu target. Here photoabsorption has the by

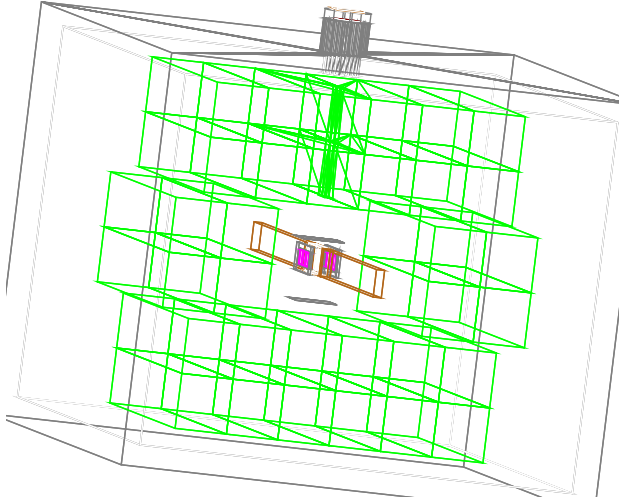


Figure 4.1.: View of the the VIP2 setup in a Geant4 MC simulation.

far largest contribution to this loss. This contribution can be estimated with the attenuation of photons going through half of the target ($25 \mu\text{m}$) which is about 25 %. This gives an estimation for the whole efficiency of about 2.5 %.

To determine the efficiency with a simulation, 10^6 photons with 7.7 keV were simulated with their starting positions randomized in the copper target and their starting directions randomized over 4π solid angle. The result of the simulation is shown in figure 4.2. In the figure all original vertices in one copper target strip (starting points - brown) of photons which deposit all their energy in the SDDs are shown. The last vertices (end point of the track - purple) where the photons lose their energy in the SDDs is also shown. Only photons are counted which deposit all their energy of 7.7 keV in the SDDs. It is evident from the figure, that most photons which are detected by the SDDs originate in the part of the 7.1 cm long target closer (“beneath” in the figure) to the SDDs. This can be explained with the larger solid angle under which these photons see the detector. Only one side

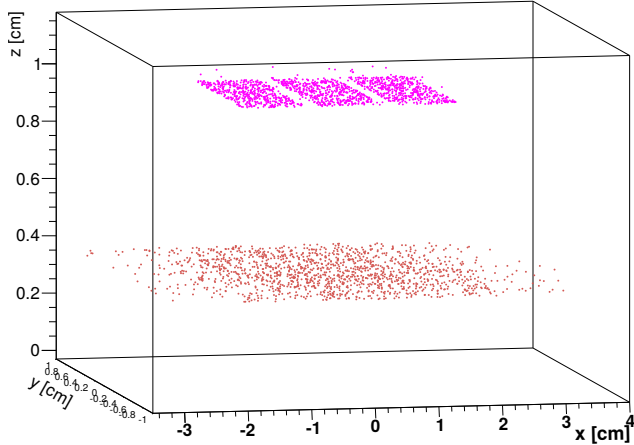


Figure 4.2.: Starting (brown) and end (purple) points of photons originating from the Cu target and hitting the SDDs.

of the simulation result is shown in the figure, as the setup is symmetric and the other side gives the same result. From the 10^6 photons starting from the target, 18,200 were detected by the SDDs. This results in efficiency of 1.82 %, which is close to the estimation of 2.5 % and therefore a plausible result.

4.2. Background from Cosmic Radiation

Cosmic radiation seen at the surface of earth primarily consists of muons [38]. The origin of this radiation is so-called primary cosmic radiation consisting of nuclei which are part of stellar power generation such as hydrogen and helium nuclei. These particles hit earth's atmosphere mainly generating mesons, which then decay into the cosmic radiation seen at the surface of the earth (e.g. muons). The rate of muons integrated over the whole solid angle is $\sim 1 \text{ cm}^{-2} \text{ min}^{-1}$ [38]. For the simulation, 10^7 muons were generated in an area of $50 \text{ cm} \times 35 \text{ cm}$ which had a distance of 20 cm to the target. The particles had 270 GeV energy and their directions were randomized in the lower half-sphere. This energy was chosen as it was reported as the mean energy of the muon spectrum at LNGS in [39]. With the above mentioned rate this corresponds to the background of ~ 4 days. This part of the background only plays a role in the measurements above ground, as it is reduced at the underground laboratory LNGS by several orders of magnitude. The goal of these simulations was to estimate the probability of the rejection of muons by scintillator veto and to estimate the signal rate from this source in the

scintillators and SDDs.

The energy deposit in each scintillator summed up over all scintillators is shown in figure 4.3. A pronounced peak at ~ 8 MeV deposited energy is visible. With a thickness of a scintillator of 4 cm, this corresponds to an energy loss of $2 \frac{\text{MeV}}{\text{cm}}$.

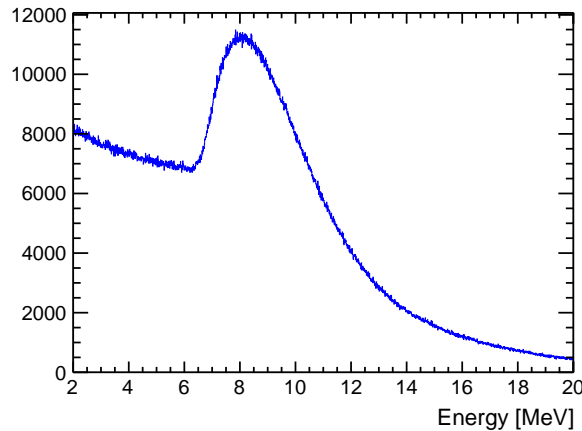


Figure 4.3.: Energy deposit of 270 GeV muons in plastic scintillators.

Furthermore, the trigger rate of the scintillators can be estimated from the rate of $1 \text{ cm}^{-2} \text{ min}^{-1}$ to be $\sim 1.67 \text{ s}^{-1}$ per scintillator. The energy deposit in the SDDs is shown in figure 4.4. The peak in deposited energy is in this case at around 300

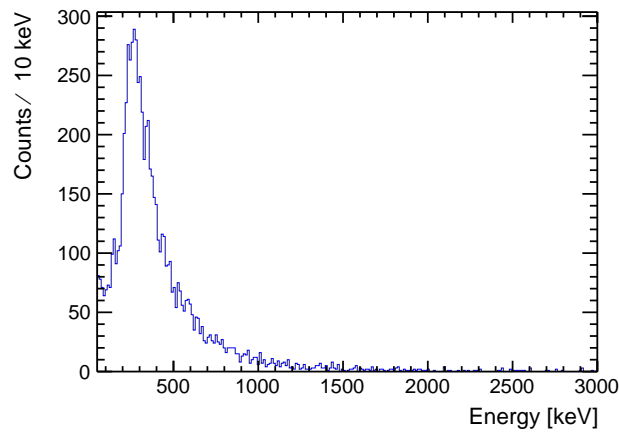


Figure 4.4.: Energy deposit of 270 GeV muons in Silicon Drift Detectors.

make a histogram
really over whole
range

keV. In all 6 SDDs combined there were 7896 hits in 7744 different events. This equates to a rate of 0.0224 Hz or 1 event about every 45 seconds. The energy range of the SDDs is divided into a range of 1 keV - 30 keV and the energy > 30 keV, as everything above this value is in the overflow bin of the ADC. Therefore it makes sense to calculate the rates for these 2 energy ranges. There are 338 hits in the lower energy range, meaning 14 hits per day in each SDD. In the higher energy range there are 7558 hits.

From the 7896 SDD events, 7859 events had an energy deposit of more than 100 keV in the inner and the outer scintillator layer. A signal in boths layers is the condition for a rejection and the threshold of 100 keV will be justified in chapter 5. This means, the background from cosmic rays can be rejected to $\sim 99.5\%$. A low energy spectrum of the SDDs with and without scintillator veto is shown in figure 4.5.

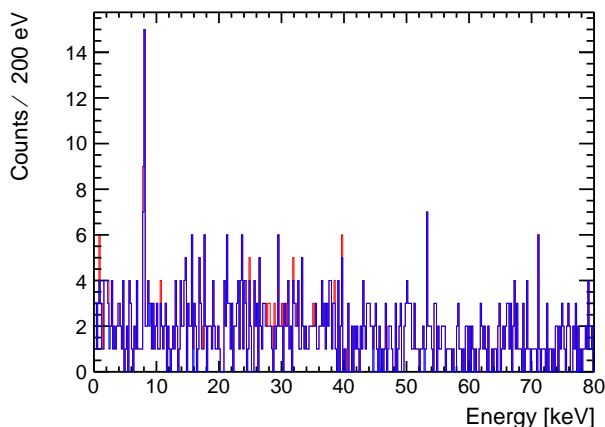


Figure 4.5.: Complete low energy spectrum of the SDDs induced by muons (red) and the part that is also seen by the scintillators (blue).

The underground laboratory LNGS lies at 3800 m water equivalent depth, where the cosmic muon flux is reduced to $3.41 \times 10^{-4} \text{ m}^{-2} \text{ s}^{-1}$ [40]. Compared to $1.67 \times 10^2 \text{ m}^{-2} \text{ s}^{-1}$ given in [38] for the surface of the earth, this is a reduction by a factor of 2×10^{-6} . The values for the event rates due to cosmic muons calculated in the previous section scale accordingly. The expected hit rate for each scintillator is then $\sim 3.4 \times 10^{-6} \text{ Hz}$ or ~ 1 event every 3 days and ~ 2 events per day for all scintillators. The expected event rate for ~ 1 event every 260 days for all 6 SDDs.

4.3. Background from Gamma Radiation

Energy spectrum in scintillators

Energy Spectrum of background

6.3×10^8 into one half-sphere seems to be correct

The background consisting of γ -rays is the dominant background in the underground laboratory LNGS, as cosmic radiation is reduced by almost 6 orders of magnitude. The origin of the γ radiation are long-lived γ -emitting primordial isotopes. They are part of the rocks of the Gran Sasso mountains and the concrete used to stabilize the cavity. The dominant isotopes of this kind are ^{238}U , ^{232}Th and ^{40}K [41] and their decay products. For the simulation 2.5×10^9 γ photons were generated on a surface of 0.945 m^2 , which completely enclosed the setup. The particles energy distribution follows the one reported in [41] in the dominant energy range from 40 - 500 keV, which was modeled by a Landau distribution with a mode at 120 keV and a sigma of 50 keV. The particles directions were randomized in the half sphere towards the setup. In [41] an integral flux of $0.33 \text{ } \gamma \text{ cm}^{-2} \text{ s}^{-1} = 2.85 \times 10^8 \text{ } \gamma \text{ m}^{-2} \text{ day}^{-1}$ was reported, whereas in [42] a flux of $6.3 \times 10^8 \text{ } \gamma \text{ m}^{-2} \text{ day}^{-1}$ was given. For now the data from [41] will be used and later the result of this assumption will be compared with the measured data. In this case the simulated 2.5×10^9 particles correspond to a data taking time of 9.28 days.

The interaction of the photons with the scintillators almost exclusively takes place via inelastic Compton scattering, meaning the photons do not deposit the complete energy. The deposited energy can be as high as 500 keV. In the 9.28 days of the simulated data, there were 184,380 events with an energy deposit in the inner and outer scintillator layer larger than 100 keV. As the trigger condition is a signal in inner and outer layer, the trigger rate from these events is 0.23 Hz or ~ 1 event every 4 seconds in all scintillators. The energy spectrum in the range from 1 keV - 30 keV deposited in the SDDs is shown in figure 4.6. In the figure the Cu $\text{K}\alpha$ and $\text{K}\beta$ lines are visible at 8 - 9 keV as well as the Zr $\text{K}\alpha$ and $\text{K}\beta$ lines at 16 - 18 keV. The Cu lines come from photons from the Cu target and the Zr lines come from photons from the Zr calibration foil. This foil is mounted in the setup for the possibility to conduct an energy calibration of the detectors with an X-ray tube. In the 9.28 days of simulated data, there were 57,617 events in all SDDs with an energy deposit > 1 keV, corresponding to a rate of 0.07 Hz or ~ 1 event every 14 seconds in all SDDs. From these events, 30,581 are in the range between 1 keV - 30 keV, corresponding to a rate of ~ 0.04 Hz. Comparing these rates to the ones induced by cosmic muons at LNGS, it is obvious that γ radiation is the dominant source of background.

From the 57,617 events in all SDDs with an energy deposit > 1 keV, 604 events have an energy deposit in the inner and outer scintillator layer and can therefore be rejected. The rejection ratio is therefore $\sim 1\%$. A plot of the full energy

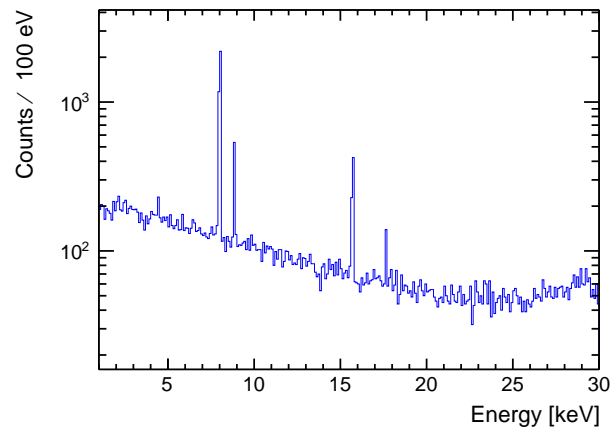


Figure 4.6.: Monte Carlo simulation of the energy spectrum induced by γ rays and detected by SDDs. Cu and Zr lines are visible at ~ 8 keV and ~ 16 keV respectively.

spectrum seen by the SDDs with the part that can be rejected is shown in figure 4.7.

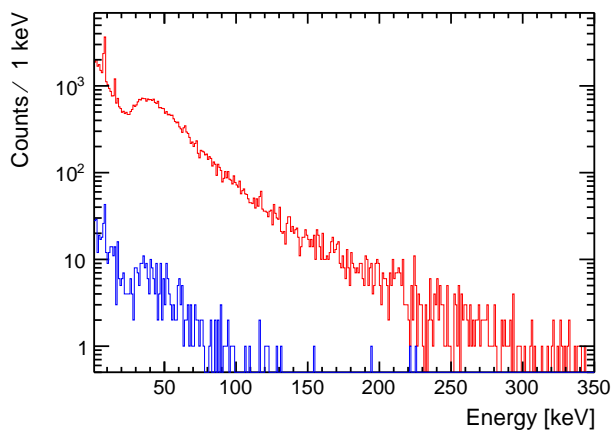


Figure 4.7.: The full energy spectrum introduced in the SDDs by γ radiation (red), with the part that can be rejected by scintillator veto (blue).

5. Test Measurements

scintillator + sipm detection ratio for cosmics (smi) and for 500 mev electrons (lnf test beam); background rejection at smi (tdc+qdc correlation) -> test of the functionality of the daq; sdd time resolution tests, sdd energy resolution determination (-> thereby also testing the cryogenics); tests with high current and water cooling; determination of the energy deposit threshold for the scintillators

time resolution sipms: $\text{tr} \rightarrow \text{Draw}((\text{tdc}[14]-\text{tdc}[1])-(\text{tdc}[14]-\text{tdc}[7])) \text{ h}(800, -400, 400), \text{tdc}[1]>0$ and $\text{tdc}[7]$)

5.1. Test Measurements at LNF

First measurements with the scintillators read out by SiPM were done at the Beam Test Factory (BTF) at Laboratori Nazionali di Frascati (LNF). This facility is connected to the linear accelerator of the DAΦNE collider and provides a 500 MeV electron or positron beam. The test setup is shown in figure 5.1, The scintillators

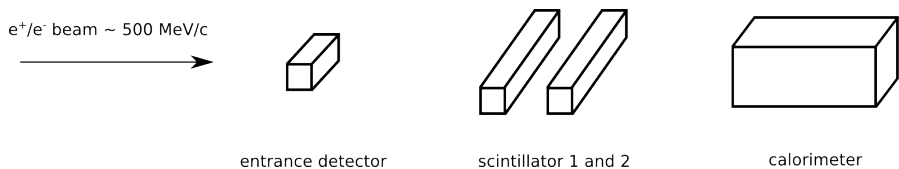


Figure 5.1.: The setup for testing the plastic scintillators with SiPM readout at the Beam Test Facility.

were the ones later on used in the VIP2 experiment, namely plastic scintillator bars of $25 \text{ cm} \times 4 \text{ cm} \times 3.8 \text{ cm}$. The trigger is defined as signal in the calorimeter AND a signal in the entrance detector, for which another scintillator was used. In case both of these detectors have a signal, both scintillators also need to have a signal because the triggering particle necessarily passes through them. The detection efficiency for any of the two scintillators is defined as the fraction of total triggers,

for which each scintillator produces a signal over threshold. Furthermore 3 different beam positions relative to the SiPM readout have been set, as shown in figure 5.2. The detection efficiency was larger than 98 % for all the beam hit position but

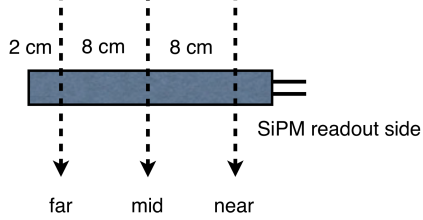


Figure 5.2.: 3 different beam positions for the tests of the scintillators at the Beam Test Factory.

no clear dependence on the hit position could be found. For each measurement the analog data from the SiPMs was converted to a digital signal in a QDC. The distribution of this signal in each case followed a Landau distribution. The most probable value of this distribution was dependent on the beam hit position and it was decreasing with increasing distance between the hit position in the readout. This means the scintillation light losses over the length of the scintillator have a measurable effect. Due to the 16 cm difference in beam hit position, the signal was decreased further away from the SiPM readout to 93 % and 87 % for the 2 scintillators respectively. The signals from the SiPMs were converted into time stamps by a TDC. By comparing these time stamps to a reference time stamp from the trigger, a time resolution of 2.6 ns (FWHM) could be estimated.

5.2. Test Measurements at SMI

smi data: 3 days and 19.5 hours

After first tests at LNF, the setup box as well as the scintillators and 2 SDD arrays which originally belonged to the SIDDHARTA experiment were transported to the Stefan Meyer Institute in Vienna in summer 2014. Tests were done with the SDDs in a smaller setup, but due to problems with Wi-Fi signals, which were probably picked up due to the similarity of Wi-Fi wavelength (~ 12 cm) and setup geometry, these tests were abandoned. Further tests were conducted with an adapted readout board in the final setup box, which was larger and therefore less likely to pick up Wi-Fi signals. The scintillators were wrapped in aluminum foil and black tape and 2 SiPMs were attached to a surface with optical glue and read out in series.

The functionality of each system of scintillator read out by 2 SiPMs was tested by connecting it the signals to an oscilloscope and checking the signals. The slow control was set up including the current supply, the temperature controller and the Pt-100 temperature sensors with their positions described in 3.4.2. The PID values of the LakeShore331 temperature controller were adjusted to ensure stable operation. The data acquisition system was set up and connected to the signals from the SDDs and the scintillators. The gain and shaping time of each SDD channel was adjusted in the CEAN 568B spectroscopy amplifier. After all these parts were tested individually, they were assembled and long term tests were conducted which will be described subsequently.

5.2.1. Water Cooling of Cu Target

One of the first tests done in order to ensure adequate cooling of the Cu target also in the case of a high current. The cooling of the target is done by water flowing through the cooling pad between the 2 copper target foils. The temperature was measured on each foil with a Pt-100 temperature sensor. 2 different measurements were done, with a high current once with and once without water cooling. The outcome is shown in figure 5.3.

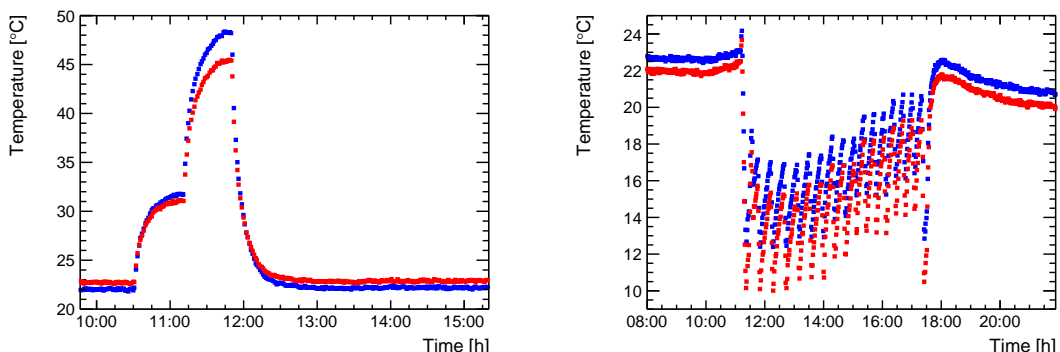


Figure 5.3.: The temperature of the 2 Cu target foils with a high current without water cooling (left) and with water cooling (right).

The left figure shows the temperatures without the water cooling with a current of 40 A (starting at $\sim 10:30$) and a current of 80 A (starting at $\sim 11:15$). The temperature rises to ~ 45 °C, well above room temperature. As even higher current of 100 A is projected, it is not an option not to use water cooling. On the right picture the temperature of the Cu target with water cooling is shown. In this case the current was varied gradually from 80 A (starting at $\sim 13:00$) to 180 A

(starting at $\sim 16:00$). In this case the temperature can be stabilized below room temperature even for a current as high as 180 A. Consequently similar temperatures of the target can be achieved for data taking with and without current.

5.2.2. Argon Cooling of Silicon Drift Detectors

maybe add argon target + argon pressure correlation; tr->Draw("slow[3]:slow[15]", "text")
which metal?

The argon cooling of the SDDs was tested in many the test runs at the Stefan Meyer Institute. The Pt-100 temperature sensors were mounted on the metal support structure of the SDDs, which is in thermal contact with the detectors. During these data taking periods, the temperature of the detectors could be kept constant at around -170 °C, except for short periods of higher temperature, with a duration of a few minutes typically. The temperature for both SDD arrays during 1 day of data taking is shown in figure 5.4. As the scheduled operation temperature

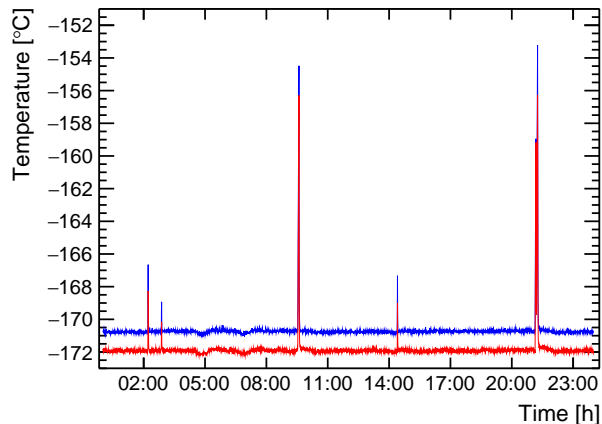


Figure 5.4.: Temperature of the 2 SDD arrays during 1 day of data taking at the Stefan Meyer Institute.

is 150 K [31] (~ -120 °C), which is still higher than during the periods with higher temperature, the performance characteristics of the detectors are not affected by these changes. But nevertheless this problem was solved in the measurement at the Gran Sasso National Laboratory (LNGS) by adding a bit more Argon to the cooling system, which ensured stable data taking conditions at a SDD temperature of around 100 K.

5.2.3. Scintillator Energy Deposition Trigger Threshold

To find out the minimum energy that needs to be deposited in the scintillators by ionizing radiation in order for the event to be detectable, we used a Caesium-137 ¹ source shining directly into plastic scintillators used in the VIP2 experiment parallel to their length axis. A 2 mm aluminum plate was mounted between the source and the scintillator in order to shield the β -radiation from the source. The scintillators were read out by 2 serially connected SiPMs on the opposite side of the source. The pulse-height spectrum of the SiPMs was recorded with an oscilloscope. The setup was modeled in the Geant4 framework and the energy deposited in the scintillator was recorded. The deposited energy was smeared in the simulation by 10 % to account for the finite resolution of the detection system. The pulse-height spectrum from the oscilloscope and the MC-spectrum are shown in figure 5.5. The

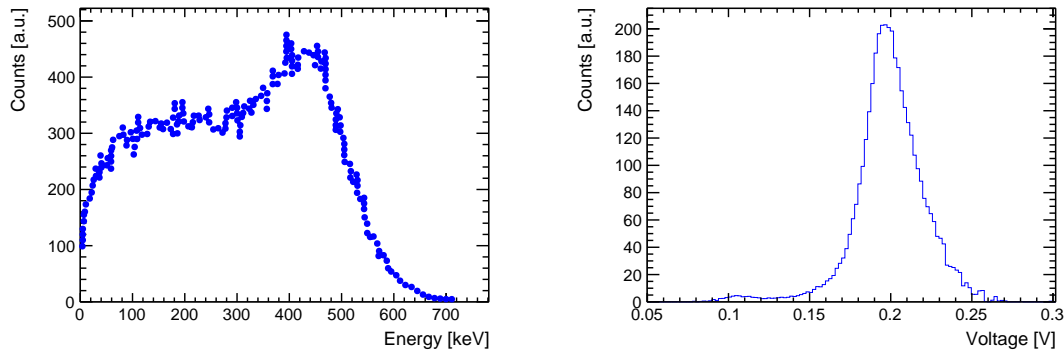


Figure 5.5.: The spectrum of energy from a Cs-137 source deposited in the scintillator from MC-simulations (left) and the pulse-height spectrum recorded with an oscilloscope (right).

pulse-height spectrum was recorded once with and once without the source. The subtracted spectrum was calculated in order to get the isolated spectrum from the source without events from external radiation. This subtracted spectrum is shown in the plot.

In the energy region of ~ 80 keV - ~ 4 MeV (which includes the photons from the Cs-137 source) the dominant energy-loss mechanism for photons in a plastic scintillator is the Compton effect [33]. Therefore not the whole energy of the photons is deposited in the detector. The falloff in the MC-spectrum corresponds

¹Cs-137 decays to a metastable Barium-137 state via β -decay with a half-life of about 30 years. This state then decays into a stable state via emission of a 662 keV photon.

to the Compton edge ². The single Compton edge of 662 keV photons is at 478 keV, higher energies in the MC-spectrum come from Multi-Compton processes and from the smeared energy resolution.

The falloff in the pulse height spectrum at ~ 200 mV corresponds to this Compton edge. The part below ~ 180 mV is partly cut from the spectrum due to the trigger settings of the oscilloscope and does not have any physical meaning. From this measurement a relation between deposited energy and output pulse height of:

$$\frac{\text{Energy}}{\text{Pulse Height}} \approx \frac{500 \text{ keV}}{200 \text{ mV}} = 2.5 \frac{\text{keV}}{\text{mV}} \quad (5.1)$$

Furthermore the threshold settings in the experiment at LNGS were set to about 40 mV. They could not be set lower than this, as at lower thresholds the rate of dark counts rises and this needs to be avoided. With $2.5 \frac{\text{keV}}{\text{mV}}$ a threshold of 40 mV corresponds to a deposited energy of 100 keV. This energy is used as a threshold for MC simulations, which were discussed in chapter 4. For the measurements at SMI the SiPM thresholds were set higher, as at this point the goal was to detect events induced by cosmic radiation, which have a typical energy deposit of a few MeV.

There are a few assumptions going into this calculation, as for example the linearity of the relation between deposited energy and output pulse height. Therefore the value of 100 keV energy deposition threshold at LNGS should be viewed as an estimation rather than a fixed value.

5.2.4. SDD Energy Resolution

The following tests of the functionality of all parts are extracted from a data taking period from 23. October 2015 - 27. October 2017, corresponding to 4 days of data taking time. There was no current flowing through the copper target during this data taking period.

To achieve the optimal energy resolution, the voltage values for the photon entrance window (B_c) and the separation mesh (B_f) (see chapter 3.1) were adjusted, before this data taking period, starting from the values used in the SIDDHARTA setup for these SDD cells. The values used are summed up in tables 5.1 and 5.2.

²When a photon scatters on a charged particle, the energy it transfers to the charged particle depends on the angle between incoming and outgoing photon. The maximum energy is transferred when the photon changes direction by 180° . As a photon can not deposit more energy in a single process, this energy marks an “edge” in the detected spectrum.

Rx	R1	Bf (SDDs: 1,2,3)	Bf (SDDs: 4,5,6)
-250 V	-16 V	-137 V	-144 V

Table 5.1.: Voltages for outer and inner SDD rings as well as for the separation meshes of the 2 SDD arrays.

Bc1	Bc2	Bc3	Bc4	Bc5	Bc6
-134 V	-121 V	-143 V	-133 V	-137 V	-144 V

Table 5.2.: Voltages for the photon entrance windows for SDDs 1-6.

After optimizing the voltage settings, the energy resolution was determined from the data taken in the data taking period in October 2015. The results are shown in table 5.3.

	SDD 1	SDD 2	SDD 3	SDD 4	SDD 5	SDD 6
FWHM @ 6 keV	148 eV	150 eV	147 eV	147 eV	156 eV	158 eV

Table 5.3.: Energy resolution (FWHM) of the SDDs @ 6 keV.

The typical statistical error of the Full Width Half Maximum (FWHM) energy resolution is 1-2 eV for this amount of data for one SDD. These energy resolutions are close to the design resolution of 150 eV (FWHM) at 6 keV given in [31]. Furthermore an approximate Fano factor of 0.137 with a statistical error of 0.007 was found. The summed up energy spectrum is shown in figure 5.6.

The Mn K α and K β lines (5.9 keV and 6.5 keV) from the Fe-55 source and the Ti K α and K β lines (4.5 keV and 4.9 keV) from the Ti calibration foil are visible. The Mn and Ti K α lines are used to find the energy scale. Details to the calibration procedure will be given in chapter 6. Furthermore the Silicon K α escape peak ³ is visible 1.7 keV below its main peak at around 2.8 keV. The Cu K α line at 8 keV is caused by external radiation hitting the Cu parts and creating vacancies in the 1s shell which are subsequently filled by electrons from the 2s shell. As the thermal energy at room temperature (\sim 25 meV) is orders of magnitude smaller than the gap between the 1s and the 2s shell (\sim 8 keV), the creation of a vacancy in the 1s shell is reliant on an external energy source. All the expected peaks are therefore visible in the spectrum and the functionality of all 6 SDDs could be established.

³An Si K α photon escapes the detector. Its energy is therefore not converted into electron/hole pairs and is missing in the spectrum.

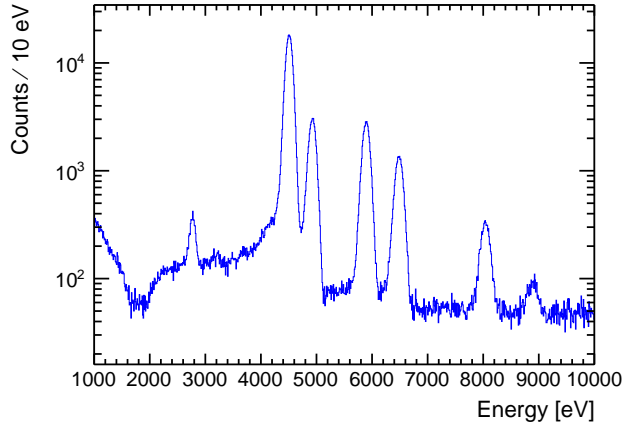


Figure 5.6.: Energy spectrum corresponding to 4 days of data taken at SMI.

5.2.5. SDD Time Resolution

For the measurement of the time resolution of the Silicon Drift Detectors, the arrival times of the digitized signals from the SDD “OR” and the SiPM “OR” at the TDC were compared. For details about the DAQ system see figure A.1 or section 3.4. As mentioned in 5.1, the time resolution of the scintillators read out by SiPMs is smaller than the one of the SDDs by around 2 orders of magnitude and is neglected here. The events in which both SDDs and scintillators give a signal are mainly caused by charged particles which first hit the scintillators and then either directly hit the SDDs or cause secondary radiation (e.g. bremsstrahlung in the scintillators), which in turn hits the SDDs. In either case the time difference of the actual hits of the radiation in scintillators and SDDs is also negligible compared to the time resolution of the SDDs. The difference in arrival times at the TDC between the 2 signals are shown in figure 5.7. The plot corresponds to all events with scintillator and SDD coincidence for the data taking period of 4 days at SMI. The time resolution was found to be around 380 ns (FWHM). This is in agreement with the specification of a time resolution $\leq 1 \mu\text{s}$ given in [31]. Furthermore the mean delay of the arrival of the SDD signal is 290 ns.

5.2.6. Scintillator plus SiPM Time Resolution

For the mentioned 4 day data taking period, the difference in arrival times of signals from the adjoining “bottom inner” and “bottom outer” layer are shown in

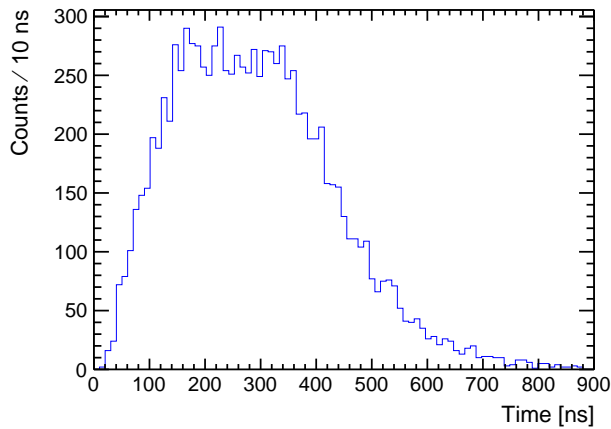


Figure 5.7.: Arrival time of the signal of Silicon Drift Detectors relative to the signal from the SiPMs corresponding to a time resolution of ~ 380 ns (FWHM).

figure 5.8. The distribution of the difference of the arrival times can approximately

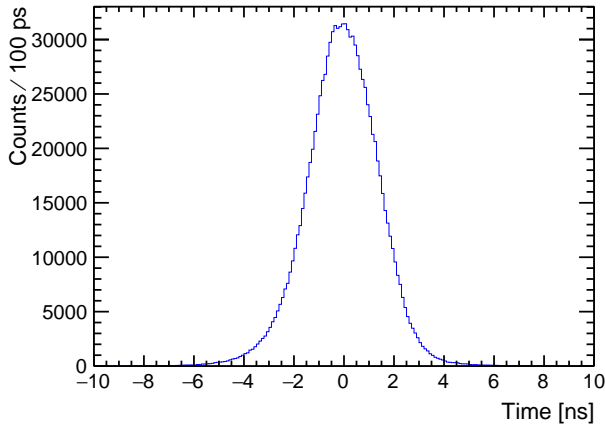


Figure 5.8.: Difference of arrival times of 2 different scintillator layers.

modeled by a gaussian distribution with a sigma of 1.38 ns or a FWHM of 3.25 ns. Assuming the time resolution is the same for both of these layers, this results in a sigma of 0.98 ns and a FWHM 2.3 ns for each layer and therefore also for each scintillator plus SiPM readout system.

5.2.7. Detection Efficiency of Cosmic Radiation and Active Shielding Test

0.993677 0.933823 0.93452

The data used for this test is again from the 4 day data taking period in October 2015 at SMI. The test was done in order to determine if particles from cosmic radiation going through the scintillators and potentially also through the SDDs were missed. The first step was to determine if any scintillator read out 2 SiPMs gave less signals than other scintillators. For this purpose the QDC spectra, which correspond to the charge deposited in the scintillator in each event, of each scintillator were investigated. One of these spectra with 2 different scales is shown in figure 5.9.

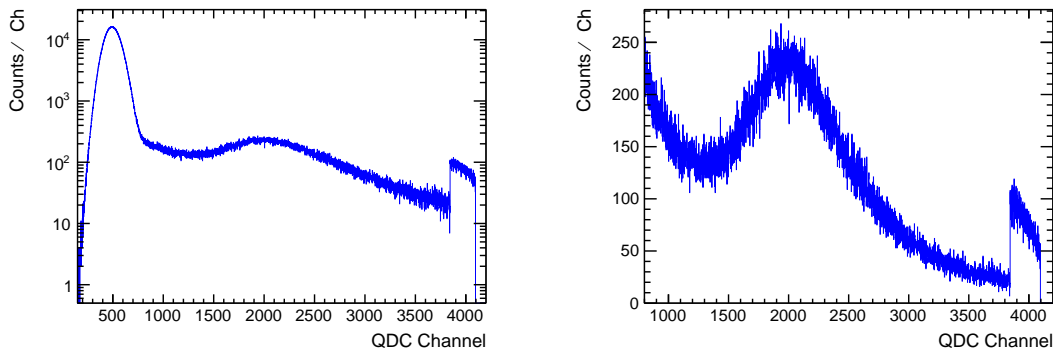


Figure 5.9.: Spectrum of charge collected by the QDC for 1 scinillator once in logarithmic scale (left) and once in linear scale (right).

The left figure shows a large peak on the left side. In these events the collected charge was low so it can be deduced that no ionizing radiation hit the scintillator. Starting from the about channel 800 there is a bump in the spectrum. For these events the collected charge was high and it can be said that there was probably ionizing radiation hitting this scintillator. To approximately determine the number of events in each scintillator, a threshold channel is introduced, above which all events where counted as signal events. This channel was determined as the 3σ deviation from the mean value of the “No-Signal” gaussian distribution. In this case the threshold channel is 800. It is interesting to compare the collected charge distribution to the distribution of energy deposited in the scintillators by cosmic radiation, which is shown in figure 4.3. The peak in the QDC spectrum at channel 2000 corresponds to a deposited energy of around 8 MeV.

The distribution of the counts determined in this way is shown in figure 5.10. The histogram is filled at positions corresponding to the positions of the scintillators in the setup, as they are shown in figure 3.5. One thing to note is that scintillators on the edge of the setup have less counts on average. This is due to the fact that for an event to be triggered, the inner and outer scintillator layer need to have a signal. Taking into account the angular distribution of cosmic radiation which is $\propto \cos^2(\theta)$ [38], there is a chance of particles hitting for example the scintillator in column 1 and layer 5, but not hitting any other scintillator, not generating an event. This effect does not play a role for more central scintillators, like for example the one in column 3 and layer 4. For all these scintillators the number of hits is about 380.000 on average, which corresponds to a rate of 1.1 Hz in each scintillator. Comparing this rate to the 1.67 Hz extracted from [38], it is obvious that the system of scintillators does not detect a part of the cosmic ray spectrum. This might be due to the shielding of the aluminum enclosure and the multistory building above the setup. But from this plot one can say that all scintillators are working and giving signals.

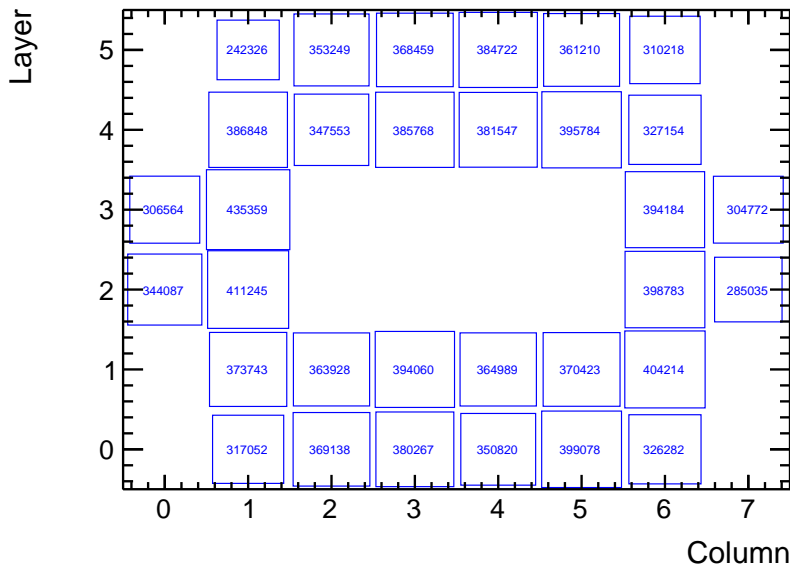


Figure 5.10.: The number of signals in each scintillator for a data taking period of 4 days.

To evaluate the detection efficiency for ionizing radiation in the energy region the scintillators should be sensible to, events were investigated in which at least 3 of the 4 scintillator layers with 6 scintillators had a signal. For these events the probability was measured that also the 4th layer had a signal. It turned out to be \sim

90 %. A reason for this number not being higher might be that a part of the events are introduced by γ radiation, for which the detection efficiency is very low as was mentioned in 4.3. This radiation could introduce events in some scintillators, while in others it does not interact. Another factor might be differences in gain settings of the SiPMs and trigger threshold settings for the SiPM signals. These differences can again lead to radiation triggering signals in some scintillators, while in others it does not.

To ensure that the active shielding system is working as expected, it is interesting to look at hit patterns. For this purpose all events for which one specific scintillator has a signal are selected and then all events (from the previously selected events) every other scintillator has are counted. In figure 5.11 a hit pattern for the

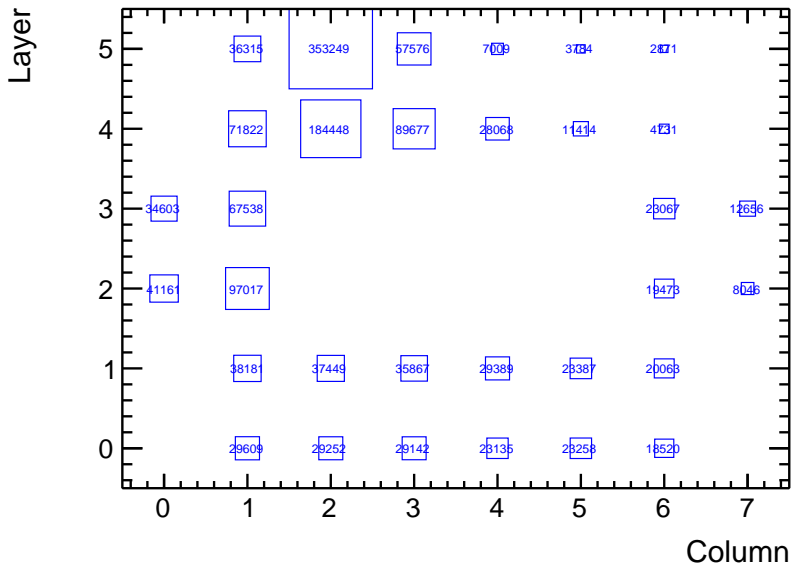


Figure 5.11.: Hit pattern for scintillator in column 2 and layer 5.

scintillator in column 2 and layer 5 is shown. It can be seen that for most events in this scintillator, the scintillator below also has an event, meaning most particles go through the setup almost vertically. Other scintillators not being directly below the specific scintillator get hit less often. The distribution resembles the $\cos^2(\theta)$ distribution of cosmic radiation mentioned in [38]. As the hit patterns for all scintillators look as expected, it can be assumed that all scintillators are connected properly and working fine. Another test was done comparing the SDD spectrum of the events rejected by scintillator veto to the expected spectrum introduced in the SDDs by cosmic muons, which was already shown in figure 4.5. The expectation

was that these spectra should be similar as a big part of the signals introduced by cosmic muons is rejected as they also trigger a signal in the scintillators. These rejected signals should be similar to the the signals in the SDDs introduced by muons. The 2 spectra are shown in figure 5.12. The first thing to note is that the

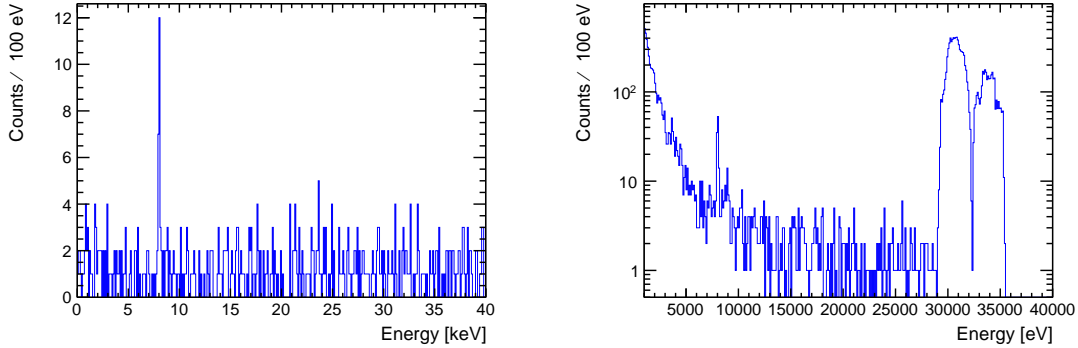


Figure 5.12.: The energy spectrum corresponding to 4 days of data introduced by cosmic radiation above ground from simulation (left) and measured (right).

peak at around 30 - 35 keV in the measured spectrum is artificial, as it is the upper end of the energy scale of the 6 SDDs. Every event with higher energy than that is filled in overflow bins. The overflow bins of the 6 SDDs correspond to slightly different energies, which makes the peak spread out over several keV. The second thing to note is that in the energy region from about 15 - 25 keV the 2 spectra are quite similar with about 1 count per 100 eV. In the energy range where the scintillator veto is crucial, the region of the forbidden Cu K α transition below 15 keV, there are more SDD hits rejected than there are predicted hits from cosmic radiation (consider the logarithmic scale on the right figure). This probably means that the scintillator veto can also reject at least a small part of the γ radiation which is present in the laboratory. Consequently the system is not only capable for what it was designed, namely detecting high energy ionizing radiation, but also detecting γ radiation.

Finally it is interesting to look at the amount of hits in the SDDs which are in coincidence with a scintillator signal. The complete spectrum together with the rejected events are shown in figure 5.13. It is obvious that only a small fraction of the SDD events can be rejected by scintillator veto. For example in the region of the the Cu lines from 7 - 10 keV a fraction of $\sim 1\%$ of events is seen in the scintillators. This rejection ratio mean that the vast majority of counts in this energy region is caused by external photons, which can only be rejected to a

check if there is a
change when a cut
on the sdd multi-
plicity is set.

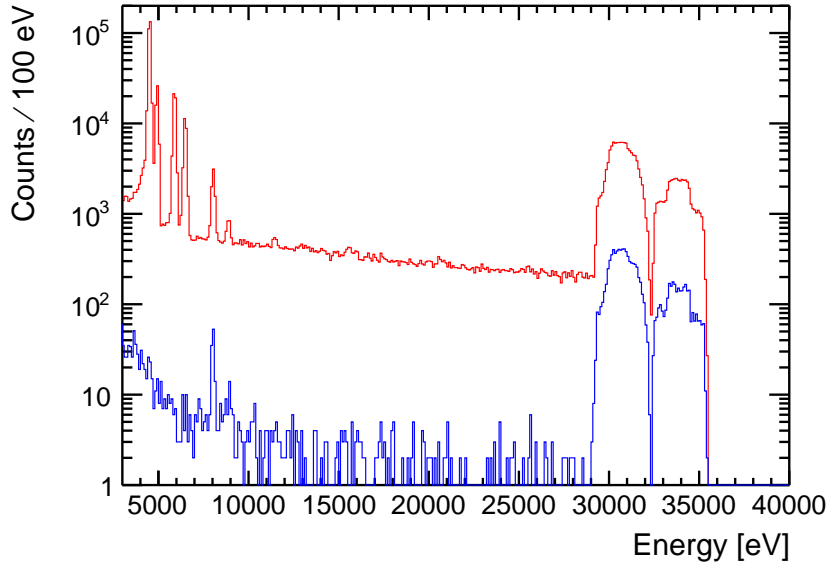


Figure 5.13.: The full energy spectrum corresponding to 4 days of data at SMI (red) and the part of the spectrum rejected by scintillator veto (blue).

small part. For this kind of radiation a rejection ratio of about 1 % was already reported as a result of simulations in section 4.3. For the part below 7 keV the Fe-55 source inside the setup contributes most of the counts, which can not be rejected. Therefore it does not make sense to calculate a rejection ratio for this energy region. The higher the energy the higher is the contribution of charged particles, with a high detection efficiency in the scintillators, to the SDD events. In the overflow bins of the SDDs, corresponding to an energy higher than around 30 keV, the rejection ratio is 6.5 %. The fact that the contribution of charged particles to the background is proportional to the energy can be seen comparing figures 4.4 and 4.7. While the peak contribution of charged particles is at around 300 keV, the contribution from external γ radiation is high from $\sim 0 - 70$ keV or so, with a maximum on the low energy side.

The test of the active shielding system has shown that the detection of charged particles works with > 90 % efficiency. All scintillators were found to work properly and contribute to the rejection of external radiation. But as the main background at SMI apparently comes from γ radiation, the background rejection ratio is as low as 1 % in the energy region of the forbidden transition. As all tests mentioned above gave the expected results it can be concluded that all detectors and parts of the data acquisition are working as expected. Crucial parameters of the experimental

setup like SDD scale linearity and peak position stability will be discussed in the the following chapter.

6. Data Taking at LNGS and Data Preparation

After exhaustive tests at the Stefan Meyer Institute, the setup of the VIP2 experiment was transported to the Laboratori Nazionali del Gran Sasso (LNGS) of INFN in November 2015. The laboratory is located beneath the Gran Sasso mountains in the Italian Abruzzo region. The Apennine mountains above the laboratory provide a natural shielding from cosmic radiation corresponding to 3800 m water equivalent depth [40]. The flux of cosmic muons in the underground laboratory is reduced compared to the flux above ground by about 6 orders of magnitude (see also chapter 4). The dominant background radiation for the experiment therefore does not come from cosmic radiation, but from γ radiation originating from radioactive isotopes like ^{238}U , ^{232}Th or ^{40}K and their decay products. These isotopes are part of the rocks and the concrete used to stabilize the cavity. The background reduction due to the shielding of the mountains is crucial for improving the final limit on the probability for the violation of the Pauli Exclusion Principle the experiment is able to set, as this limit is proportional to the square root of the background. A comparison of the spectra taken at Stefan Meyer Institute and at LNGS is shown in figure 6.1. The counts in the energy region of the forbidden transition at about 7.7 keV, just below the Cu $\text{K}\alpha$ peak, are reduced by a factor of 5. In the region below 7 keV, the counts do not change drastically, as in this energy region most of the events are caused by X-rays from the Fe-55 source and the titanium calibration foil. These counts are similar, as the source rate is the same at SMI and LNGS (apart from a slight decrease in the rate of the source due to its half-life of 2.7 years).

After some tests in November 2015 and a break over the Christmas holidays, the first data without current was taken in February 2016. After a period of further tests and maintenance and a data taking break in summer 2016, the first data with current was taken in October 2016. Data taking continued with various breaks for maintenance until November 2017 when problems with the argon cooling forced a stop. Parts of the VIP2 setup were then brought back to SMI for fixing these problems and to exchange the SDDs for ones with a larger active area and easier

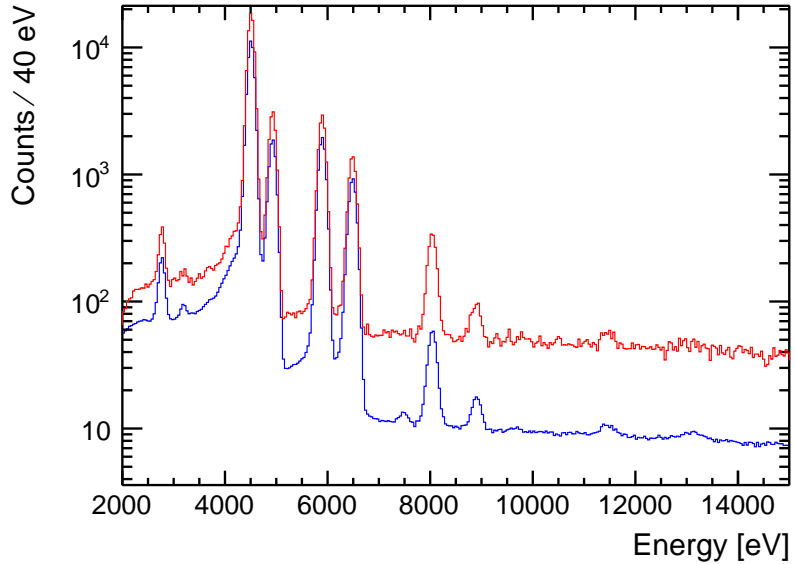


Figure 6.1.: The complete spectra from SMI (red) and LNGS (blue) both scaled to 1 day of data taking time.

cooling (see for example [43]). The maintenance and experiment upgrade is still ongoing at the time this thesis is written (January 2018). Until the end of July 2017, a total of 116 days and 20 hours of data without current and 81 days and 10 hours of data with a current of 100 A have been taken at LNGS. After a break during summer 2017 which was used for maintenance, around 25 more days of data without current were taken until November 2017. Switching the current on during this period was not possible due to the problems with argon cooling. These 25 days of data are not included in this work.

6.1. Comparison of Data and Simulations

To check if the data corresponds to expectations, it is interesting to compare it to the simulations discussed in chapter 4. The measured counts above 7 keV together with the counts expected from simulations is shown in figure 6.2. The basis for the calculations was the γ spectrum reported in [42] with $6.3 \times 10^8 \gamma \text{ m}^{-2} \text{ day}^{-1}$. The good agreement between the measured data and the simulation based on this result favors it over the result reported in [41], where about half the γ flux was reported. This also shows that by far the largest contribution to the counts in

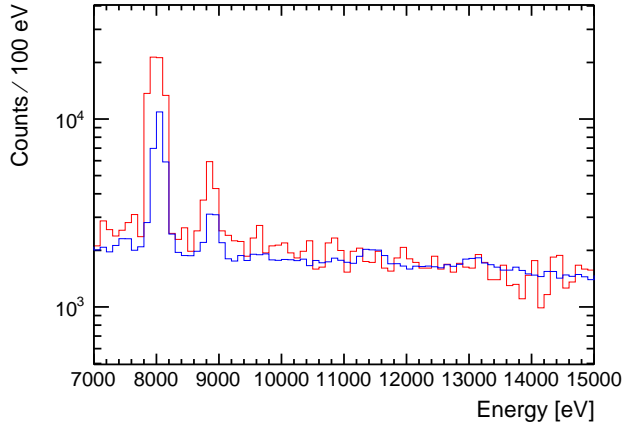


Figure 6.2.: The simulated spectrum introduced by γ radiation (red) scaled to the same data taking time (81 days 10 hours) as the data with current (blue).

the region of the Pauli-forbidden transition at 7.7 keV comes from the γ radiation originating in the surrounding rocks of the underground laboratory.

The scintillator rejection rate of 1 % predicted by simulations can also be compared to the measured data. The spectra taken with and without current are shown in figure 6.3 together with the counts that can be rejected by scintillator veto. The

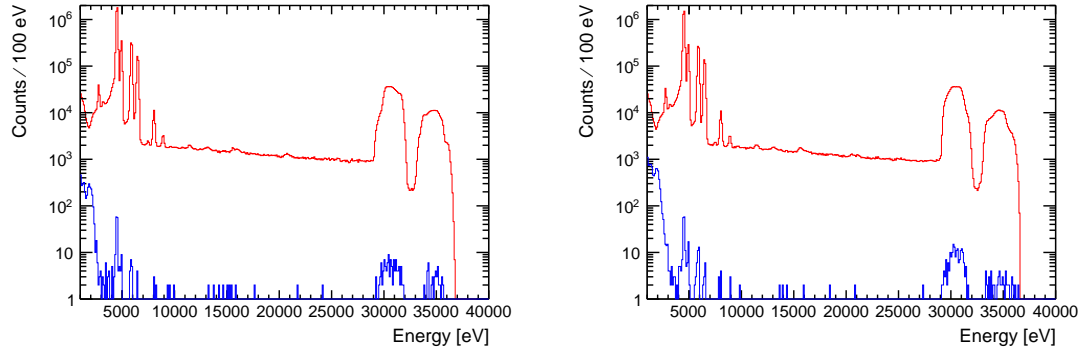


Figure 6.3.: The complete spectrum without current (left) and with current (right) in red taken at LNGS with the respective counts rejected by scintillator veto in blue.

rejection ratio for the counts above 7 keV is 0.02 % for the data with and without current. The 2 datasets were separated for this analysis in order to check for

maybe only show
>7 keV not to show
accidentals

noise effects that might be introduced by the 100 A current. These effects were not observed. Comparing this outcome to simulations, a rejection rate of 0.02 % points to a minimum energy deposition of 200 keV in inner and outer scintillator layer to produce a veto signal. This value of 200 keV is double the value of 100 keV estimated for this threshold in chapter 5. But as this values is an estimation rather than a calculation, 200 keV can be accepted as the threshold value, despite this discrepancy. The trigger logic of inner AND outer scintillator layer instead of triggering on any scintillator signal was kept in order to avoid triggers from SiPM dark counts. As the trigger condition was an AND of the 2 layers, both layers would need to have a dark count in order to produce a dark count trigger. As these correlated dark counts are much more unlikely than single dark counts, they can be suppressed in this way.

The rate of high energy charged particles impinging on the setup can be estimated from the spectra of scintillator signals recorded by the QDC. Events with high energy deposited in one scintillator can be attributed to these particles, as their energy deposition is typically higher than the one from γ radiation. This is difficult for 2 reasons: Firstly the count rate of high energy charged particles is very low, on the order of a few counts per week per scintillator. Secondly the separation between events caused by γ radiation and charged particles is not unambiguous. Nevertheless a rate of 1 event per scintillator every 3 days can be estimated from the data. This is in good agreement with the rate given in [40] of $3.41 \times 10^{-4} \text{ m}^{-2} \text{ s}^{-1}$.

6.2. Effects of 100 A Current

The 100 A current flowing through the Cu conductor affects the measurements in several ways. One effect is that the heat produced by the current in turn heats the SDDs, which are mounted about 0.5 cm away from the Cu strip. The temperature of the Cu strips is stabilized by a water cooling system and the temperature of the SDDs is kept constant by argon cooling (see also chapter 3). These cooling systems counteract any temperature change of the detectors. The measured SDD temperatures are shown in figure 6.4. The x-axis of this and similar upcoming plots spans a time from February 2016 until July 2017. Each data point corresponds to a measurement at one time for each day of data taking time. This is also valid for all similar upcoming plots. From the figures it can be seen that the 100 A current (red data points) only raises the temperature of the metal frame of the SDDs by about 0.2 - 0.4 °C compared to the measurements without current (blue data points). The temperature of the detectors themselves might be affected more than shown

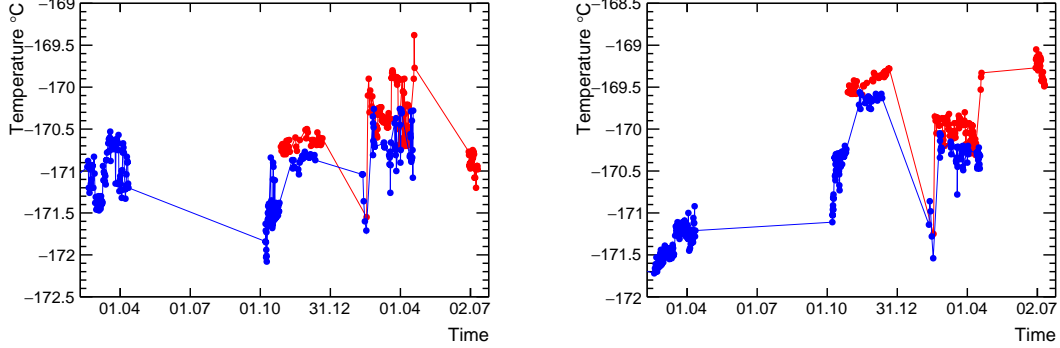


Figure 6.4.: Temperature measured on the metal frame of SDDs 1-3 (left) and on the metal frame of SDDs 4-6 (right). Data points with 100 A current are shown in red and data points without current are shown in blue. The x-axis spans a time from February 2016 until July 2017.

in the plots, but as there is no possibility to measure it directly it is impossible to be certain. Nevertheless it shows that the SDD environment can be stabilized at cryogenic temperature even with high currents. It is worth mentioning that the problems with suddenly rising temperature of the SDDs (see also chapter 5) were overcome during the measurements at LNGS by filling more argon gas into the system.

Another interesting effect of the 100 A current is that it influences the energy resolution of the silicon detectors. A plot of the energy resolution of one SDD at 6 keV for different times of measurement with and without current is shown in figure 6.5. The resolution gets worse in times when the current is turned on by about 20 eV (FWHM). This effect might be caused by the temperature rise in the SDDs mentioned above. The dependence of energy resolution on temperature was for example reported in [32]. The change in temperature of the detectors would have to be higher than the 0.4 °C measured on their metal holder. The same effect of peak broadening due to a current was also reported in [18], where it was attributed to electronic noise introduced by the current. The energy resolution at 6 keV measured at LNGS with and without current for the complete data taking time are shown in table 6.1 for each single SDD and for the spectrum resulting from the summation of all single SDDs. The energy resolution changes by about 10 eV at 6 keV when turning on the current for the summed up spectrum. The same effect also occurs at an energy of 8 keV where the Pauli-forbidden transition is expected.

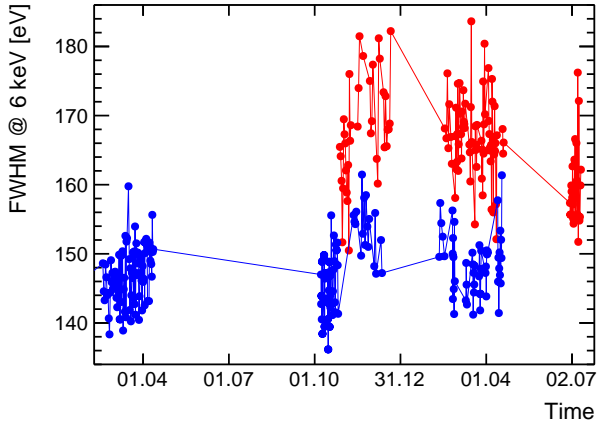


Figure 6.5.: Energy resolution (FWHM) at 6 keV for SDD 1 without current (blue) and with current (red).

current	SDD 1	SDD 2	SDD 3	SDD 4	SDD 5	SDD 6	Sum
0 A	159 eV	151 eV	151 eV	149 eV	157 eV	163 eV	155 eV
100 A	177 eV	165 eV	166 eV	155 eV	160 eV	169 eV	165 eV

Table 6.1.: Energy resolution (FWHM) of the single SDDs and their sum at 6 keV. Typical statistical uncertainty for the amount of data going into this calculation is 0.5 eV.

6.3. Spectral Lines in the Energy Spectrum

The low background at LNGS gives the opportunity to study possible spectral lines from elements occurring in the equipment surrounding the detectors. Conclusions from this analysis might be used to improve future MC simulations of the setup. The complete energy spectrum taken at LNGS corresponding to about 198 days of data is shown in figure 6.6. The most prominent peaks are the Cu K α and Cu K β peaks. The corresponding photons originate from the Cu conductor next to the SDDs. Another peak of certain origin is the Ni K α peak at 7.5 keV. Nickel is for example used in stainless steel, from which the tubes of the argon cooling system and other parts of the setup are made. The Zirconium spectral lines come from a 15 μ m thick Zirconium foil mounted above the SDDs, which was initially mounted for calibration with an X-ray tube. The anode of this tube is made out of tungsten (W), from which the W L-lines might be coming from. Several other lines are drawn in the figure, which were suggested in [6]. As the 2 sources of calibration are Ti K α and Mn K α at 4.5 keV and 5.9 keV respectively, the energy

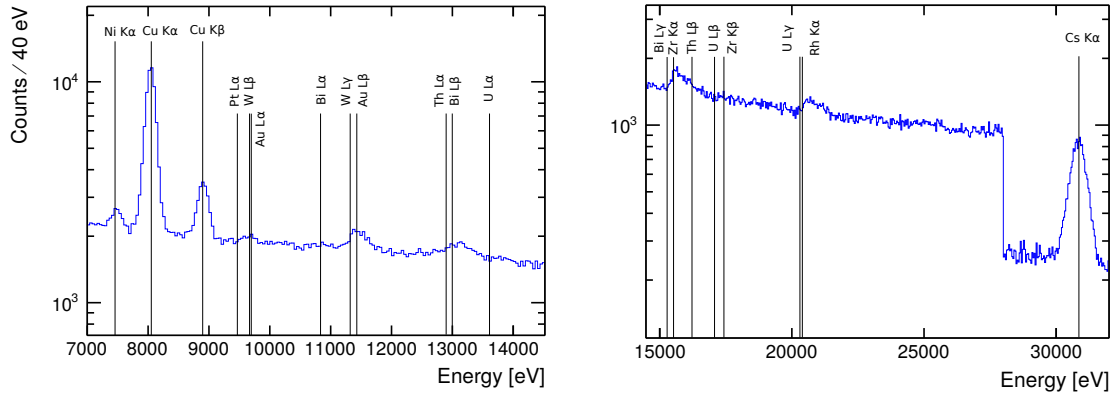


Figure 6.6.: Energy spectrum corresponding to 198 days of data taken at LNGS with candidates for spectral lines. The drop at 28 keV is artificial as above this energy all but 2 SDDs are in overflow.

calibration has a higher uncertainty for higher energies further away from these lines. This effect limits the possibility to accurately determine the spectral lines with higher energy.

6.4. Data Selection

The selection of correct events is important in the VIP2 experiment. First SDD events were discarded which occurred in coincidence with an active veto signal. This was already discussed in chapter 6.1 for example.

Furthermore events were neglected which occurred in a time of a higher than normal background rate. Excluding any possible source of background, which causes events in the energy region of the forbidden Cu K α transition, is important as it complicates finding candidate events from this transition. Figure 6.7 shows the rate of events with an energy deposit above 7 keV in any SDD. The rate of events with an energy lower than that is dominated by events caused by the Fe-55 source. The left picture corresponds to the complete dataset. A period of higher event rate by a factor of about 2 in the time around the 11. February 2016 is visible. The reason for this increase is not clear. These data were left out in the data analysis. The same event rate without these data is shown in the right picture of figure 6.7. The rate is stable throughout the whole period, which was then used for the analysis. It is interesting to look at the rate of events with an energy smaller than 7 keV, which are caused by the Fe-55 source mainly. Due to

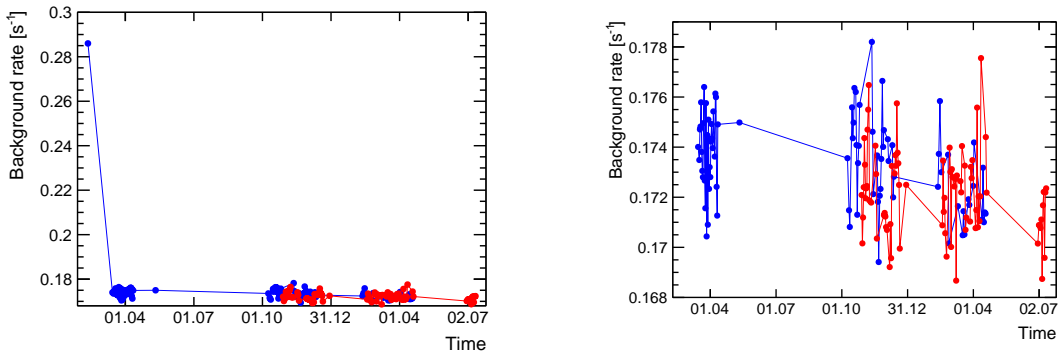


Figure 6.7.: The rate of events with an energy deposit larger than 7 keV for the complete dataset (left) and for the cleaned dataset (right). Each dot corresponds to 1 day of data.

its half-life, events from the source decrease by a factor of 0.68 in the course of the data taking of 1 year and 5 months.

Events in the SDDs originating from a Pauli-forbidden transition are expected to hit only one SDD as only one photon is produced in the course of this process. Therefore all events with a multiplicity larger than one can be excluded when looking for those photons. The distribution of SDD hit multiplicity is shown in figure 6.9. The vast majority of events has an ADC multiplicity of one, from which in turn the vast majority comes from the Fe-55 source. Additionally there are events caused by the environmental γ radiation and possibly events from non-Paulian transitions in the spectrum with 100 A current. All these are used for the analysis. Events with SDD multiplicity 2-5 are caused by high energy γ radiation causing hits in several SDDs, for example by generating multiple secondary photons. Another possibility of signals in 2 SDDs is a hit of any energy on the border of one SDD, where a part of the generated charge is transferred to the neighboring SDD. That events of this kind exist can be seen for example in figure 6.10. Here the charge generated by a photon either directly from the Fe-55 source or the Ti foil is split and drifts to the anodes of two neighboring SDDs. The energy equivalent to the total deposited charge equals the energy of one of the calibration lines. Consequently these lines run diagonally through the figure. Low energy parts are cut from the figure to enhance visibility. The vast majority of events with SDD multiplicity 6 are caused by noise. This can be stated with certainty as their rate is fluctuating with time. It is also dependent on parameters it should not be connected with, like the SiPM trigger rate.

[add multiplicity
larger than 7 keV?](#)

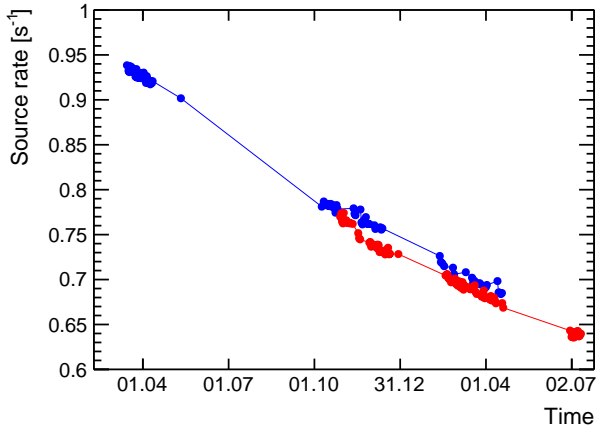


Figure 6.8.: The rate of counts caused by the Fe-55 source for the data with current (rate) and without current (blue). It is decreasing due to the half-life of Fe-55 of 2.7 years.

6.5. Energy Calibration

As the goal of the VIP2 experiment is to count events in the energy region of the Pauli-forbidden Cu K α transition, the determination of the energy of each SDD hit is of utmost importance. Assigning for example an energy of 7.7 keV to an event coming from a photon from a normal Cu K α transition at 8.05 keV changes the outcome of the experiment and has to be avoided. Furthermore the energy resolution should be kept as small as possible close to the intrinsic energy resolution of the detectors. A drift of the peak position is one of the effects that leads to a deterioration of the energy resolution.

details about fit
(root, minuit, likelihood,...)

An energy calibration of the detector is the conversion from the primary spectrum in ADC channels into energy in electron volt. For this purpose the position of the Mn K α and Ti K α peak are determined in the primary spectrum. As the energies of these peaks are known, a linear relation between ADC channel and energy can be calculated. The ADC channel of every event is then scaled according to this linear relation into an energy. To determine the position of the peaks as precisely as possible, the complete spectrum is fit, taking into account all features of a real detector. This fit function will now be discussed. In the fitting procedure, the relation for the energy resolution which is only dependent on Fano and constant

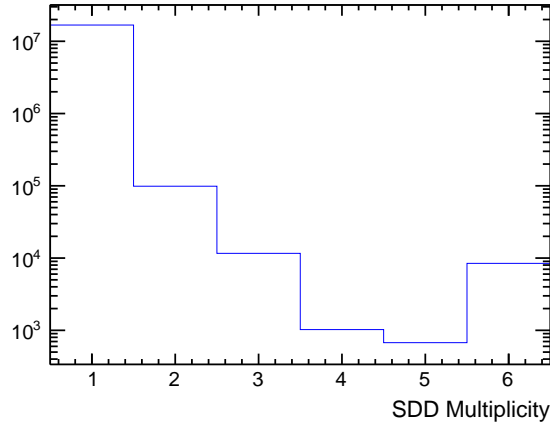


Figure 6.9.: Distribution of SDD hit multiplicity for the complete dataset taken at LNGS.

noise is assumed (see also chapter 3.1):

$$\sigma(E) = \omega \sqrt{W^2 + \frac{FE}{\omega}} \quad (6.1)$$

In equation 6.1, ω is the energy needed to create an electron hole pair in silicon, which is 3.81 eV at 77 K [33]. W denotes the contribution to noise independent from energy and F is the Fano factor.

Photons from a monoenergetic source cause a complex spectrum in a real detector. For silicon detectors they were described for example in [44] and [45]. The main feature is the *Gaussian peak*, corresponding to the case in which all electrons that are produced by the incident photon are collected at the anode. The width of this Gaussian is determined by the intrinsic detector resolution and the natural linewidth. The natural line shape is a Lorentzian with a width of typically a few eV FWHM [46]. The intrinsic detector resolution gives rise to a Gaussian line shape with a width of about 100 - 200 eV FWHM, depending on the energy. The real line shape is then a convolution of these two shapes, which would be a Voigt function. As the intrinsic detector resolution is by far larger than the natural linewidth, the latter contribution is small and the shape can be approximated by a Gaussian function. On the low energy side of the main Gaussian peak, there is a structure in the spectrum which is caused by incomplete collection of the charge generated by the detected radiation. The effects contributing to these structures are summed up in [44]. Qualitatively they can be described by an exponential *tail* energetically right below the main peak and a *shelf* extending from the main peak

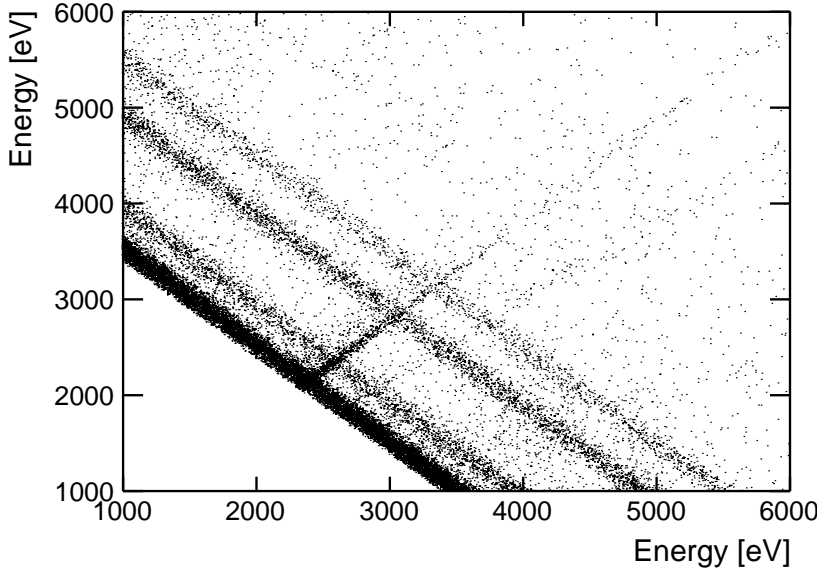


Figure 6.10.: Energy correlation between 2 neighboring SDDs. The Ti and Mn lines are visible on lines with a constant sum of energy due to cross talk between adjoining detectors.

to zero energy. A *truncated shelf* extending from the energy of the main peak to smaller energy has also been described, but it was not used here. Furthermore a photon from a Si K α transition has a high chance of escaping the detector. These photons can originate from a photoelectric effect induced by the primary photon. These events are then seen as a so-called *escape peak* 1.74 keV (Si K α energy) below the main peak. *Pile-Up effects do not play a role as the event rate is as low as about 1-3 Hz at LNGS.* The mathematical structure of all the mentioned components is shown in equations 6.2 - 6.5 and is similar to the one used in [45]. The number i denotes the number of the ADC channel.

$$\text{Gaussian peak } (i) = \frac{\text{Gain}}{\sigma} \times \exp\left(-\frac{(i - i_0)^2}{2 \times \sigma^2}\right) \quad (6.2)$$

$$\text{Tail } (i) = \text{Gain} \times tR \times tN \times \exp\left(\frac{i - (i_0 - tSh)}{\sigma_{tail} * tSl}\right) \times \text{erf}\left(\frac{1}{\sqrt{2} * tSl} + \frac{i - (i_0 - tSh)}{\sqrt{2} * \sigma_{tail}}\right) \quad (6.3)$$

$$\text{Escape } (i) = \text{Gain} \times eR \times \frac{1}{\sigma_E} \times \exp\left(-\frac{(i - (i_0 - SiK\alpha))^2}{2 \times \sigma_{escape}^2}\right) \quad (6.4)$$

$$\text{Shelf } (i) = \text{Gain} \times sR \times \frac{1}{2} \times \text{erf}\left(\frac{i - i_0}{\sqrt{2} \times \sigma}\right) \quad (6.5)$$

Is that true?

Here $\text{erf}()$ denotes the error function. A schematic drawing of the structure of a monoenergetic peak in the detected spectrum is shown in figure 6.11. The

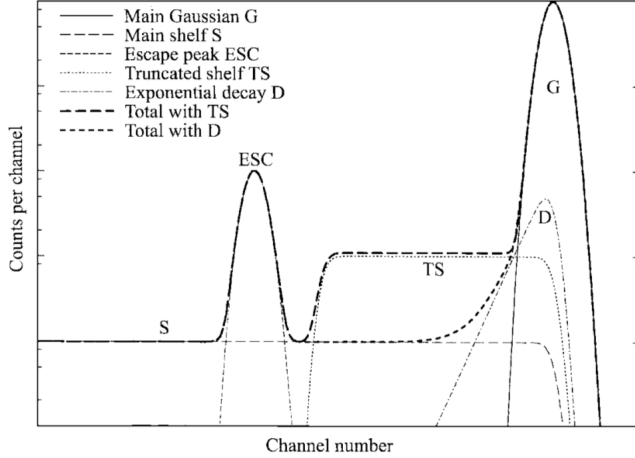


Figure 6.11.: Detected spectrum from monoenergetic incident radiation with a structure described in the text [44].

parameters used in equations 6.2 - 6.5 are described in detail in table 6.2. The parameters are fit for the Mn $K\alpha_1$, $K\alpha_2$, $K\beta$ and for the Ti $K\alpha_1$, $K\alpha_2$, $K\beta$ lines. The gain ratio of the $K\alpha_2$ to $K\alpha_1$ lines is fixed to 0.51 for Mn and to 0.5 for Ti. The sum of all the functions is obviously fit to the data together with a linear part representing the background. The positions of the Mn $K\alpha_1$ and Ti $K\alpha_1$ are used to find the linear relation between ADC channels and energy. When the amount of data is high enough, the Cu $K\alpha_1$, $K\alpha_2$ and $K\beta$ lines are fit in a similar way. Other lines shown in figure 6.6 are not taken into account in the fitting procedure due to too low statistics. A typical fit with residuals is shown in figure 6.12. The reduced χ^2 of the shown fit is 1.3. From the fit the linear relation between energy and ADC channel can be derived. It is shown in figure 6.13.

6.6. Peak Stability and Data Splitting

The fitting procedure described in the chapter 6.5 can be used to determine the stability of the peak positions for the Mn and Ti peaks. The data taken at LNGS was analyzed in this way. The result for one SDD is shown in figure 6.14, where each data point represents about one day of data. The peak position changes by about 20 ADC channels in the course of the data taking. This is a typical value similar for all six SDDs. As one ADC channel corresponds to about 9 eV in the

Parameter Name	Parameter Description	Fit Parameter
Gain	Gain of the main Gaussian peak	Yes
σ	Detector energy resolution at the energy of the Gaussian peak	calculated from Fano and constant noise
σ_{tail}	Detector energy resolution at the energy of the peak of the exponential tail	calculated from Fano and constant noise
σ_{escape}	Detector energy resolution at the energy of the escape peak	calculated from Fano and constant noise
i_0	ADC channel of the main peak	Yes
tR	Ratio of the exponential tail to the main peak	Yes
tN	Norm of the exponential tail	No
tSh	Shift of the exponential tail to the low energy side	Yes
tSl	Slope of the exponential tail	Yes
eR	Ratio of escape peak to the main peak	Yes
SiK α	Energy of the Si K α transition (1.74 keV)	No
sR	Ratio of the shelf to the main peak	Yes

Table 6.2.: Parameters going into the fit of a signal produced by monoenergetic radiation.

final energy spectrum, the peak position changes by about 180 eV. In the case of the SDD for which the peak position is shown in the figure (SDD 3), the energy resolution at 6 keV (FWHM) would change from 151 eV for a small data set to 179 eV for the whole data taking period. As the energy resolution needs to be kept as small as possible in order to determine possible events in the energy region of the Pauli-forbidden transition as accurately as possible, the data needs to be divided into subsets for calibration. The strategy for determining the energy of each event as well as possible is as follows:

Finding the optimal time for the subsets of data means to minimize the energy resolution at about 8 keV, where the non-Paulian transition is expected. There are two effects that need to be considered: Firstly the intrinsic energy resolution of the detector together with the drift of the energy scale with time gives a large contribution to the detector resolution. This contribution can be estimated with formula 6.1 and the measured resolutions from the Ti and Mn lines. This effect will contribute less when the time of the data subset is low, as the effect of the peak drift is then minimized. This can be seen from the right image in figure 6.15.

The second contribution to the uncertainty in the determination of energy of an event around 8 keV comes from the statistical uncertainty of the peak position of the Ti K α_1 and Mn α_1 calibration lines given by the fit. Taking into account the relation between ADC channels and energy as well as these statistical errors, the energy uncertainty at 8 keV can be calculated with error propagation. This contribution to the uncertainty increases with decreasing data taking time, as the statistical error of the calibration lines increases in this case. It is shown in the left image of figure 6.15. The numbers in the figure correspond to an average over all 6 SDDs and were calculated from a dataset of 30 days from LNGS without current, which was divided into subsets of 0.1, 0.25, 0.5, 1, 2 and 4 days. The above mentioned uncertainties were calculated for every subset and averaged. The Cu K α line itself can not be used for calibration due to its low event rate.

The variances of the two contributions can be added as:

$$\sigma_{tot} = \sqrt{\sigma_{det}^2 + \sigma_{stat}^2} \quad (6.6)$$

why is it so good?

and the result is shown in figure 6.16 . The results for all 6 SDDs have been averaged for this figure. The minimum energy resolution was found for a data taking time of 0.25 days or 6 hours. Therefore the data taken at LNGS was divided into parts with 6 hours each. As an interrupt of continuous data taking caused a mandatory stop for this part of data, some parts had to be longer. For example a continuous data taking period of 14 hours was divided into one part with 6 hours and another one with 8 hours. In this manner 198 days and 7 hours of data were divided into 618 parts. For each of them each of the six SDDs was calibrated separately and added up to two energy spectra, one with and one without current.

6.7. Scale Linearity and 2nd Order Correction

With the Ti and Mn K α lines as two sources of calibration it is not possible to determine if the relation between ADC channel and energy is linear over the whole spectral range. But for cases in which the Cu K α line has enough events to determine the position of its peak, it is possible to investigate it. This is possible for example for the 4 days of data taken at SMI, for which the spectrum of one SDD is shown in figure 6.12. The relation between ADC channel and energy for this fit is shown in figure 6.13. To determine the scale linearity, it is interesting to look at the difference of the position of the peaks determined by the fit to their position calculated from the position of the two calibration lines. This is the equivalent of the distance between the red line (which runs through the Ti K α_1 and the Mn

$\text{K}\alpha_1$ peaks) and the data points corresponding to the fit positions of the peaks. This plot is shown in figure 6.17. For a perfectly linear scale, the points should all be at zero deviation. As the Ti and Mn $\text{K}\alpha_1$ peaks are used for calibration, their deviation from the expected position is zero by definition. It is important to note that the fitted position of the Cu $\text{K}\alpha_1$ peak deviates by about 1.5 channels from the position it should be according to the position of the calibration lines. The same effect was observed in the data taken at LNGS. This hints to a not perfectly linear scale and the necessity to introduce 2nd order corrections into the linear relation of ADC channel to energy calculated from the position of the two calibration peaks. The formula for the 2nd order correction is shown in equation 6.7.

$$i(E) = C_1 + C_2 \times E + C_3 \times E^2 \quad (6.7)$$

Here C_1 and C_2 are the coefficients in the relation between ADC channel (i) and energy (E) calculated from the two calibration lines. To calculate the coefficient C_3 for the data from LNGS, the whole data taken there was first scaled to energy like it was described in chapters 6.5 and 6.6 for each SDD. The peak position of the Cu $\text{K}\alpha_1$ position was determined. C_3 was then determined for each SDD so that the energy scale was changed in such a way that this peak was at the correct energy. This had to be done for the complete dataset at once, as the subsets of data mentioned in chapter 6.6 do not have enough data to determine the position of the Cu $\text{K}\alpha_1$ peak. The position of this peak with a linear scale and a 2nd order scale is shown in tables 6.3 and 6.4. From the tables it can be seen that the peak

Cu $\text{K}\alpha_1$ position	SDD 1	SDD 2	SDD 3	SDD 4	SDD 5	SDD 6	Sum
Linear Scaling	8062.7 eV	8047.5 eV	8066.5 eV	8061.4 eV	8065.5 eV	8063.3 eV	8062.8 eV
2 nd order correction	8046.4 eV	8047.1 eV	8047.4 eV	8049.3 eV	8049.7 eV	8047.1 eV	8048.0 eV

Table 6.3.: Cu $\text{K}\alpha_1$ peak position with linear scaling and with 2nd order scale correction for the data without current. Statistical errors are around 2 eV for single SDDs and 1 eV for the sum of all six SDDs.

position of the Cu $\text{K}\alpha_1$ peak is at its correct position in the energy spectrum of 8047.8 eV. The spectra acquired by the steps described in the chapters 6.4 - 6.7 were then used for calculating the upper limit for the probability for a violation for the Pauli Exclusion Principle.

Cu K α_1 position	SDD 1	SDD 2	SDD 3	SDD 4	SDD 5	SDD 6	Sum
Linear Scaling	8068.6 eV	8052.7 eV	8058.9 eV	8063.4 eV	8068.5 eV	8063.9 eV	8064.6 eV
2 nd order correction	8046.9 eV	8047.2 eV	8048.0 eV	8049.7 eV	8048.9 eV	8047.2 eV	8048.0 eV

Table 6.4.: Cu K α_1 peak position with linear scaling and with 2nd order scale correction for the data with current. Statistical errors are around 2 eV for single SDDs and 1 eV for the sum of all six SDDs.

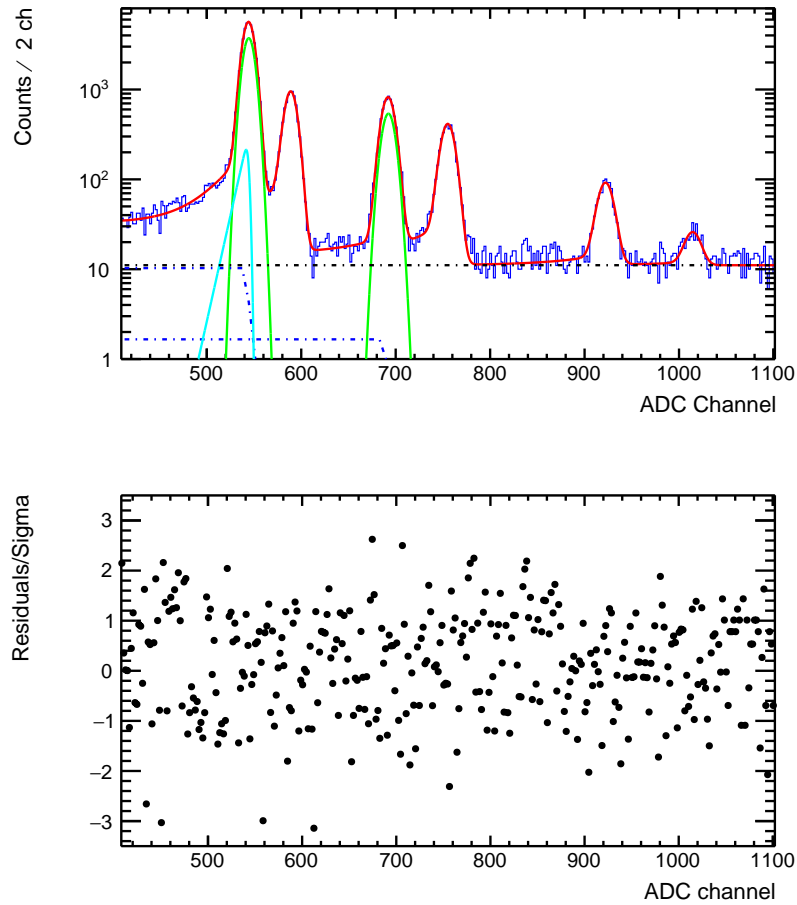


Figure 6.12.: Fit of data taken at SMI (blue) with the complete fit function (red). Some of the constituents of the fit function are shown like Ti and Mn K α_1 peaks (green), constant background (black, dashed), Ti K α_1 exponential tail (cyan) and the shelf functions of Ti and Mn K α_1 (blue, dashed). Residuals are shown below.

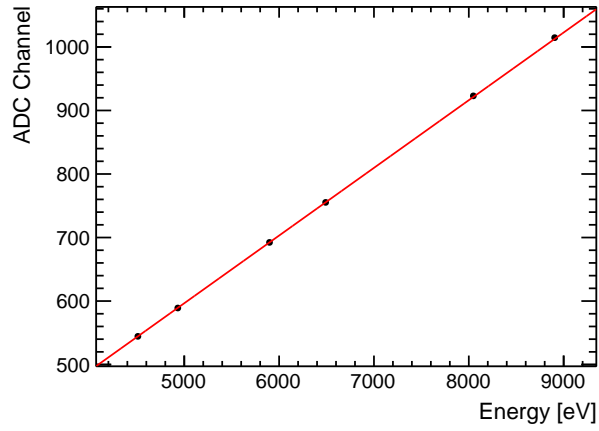


Figure 6.13.: The relation between ADC channel and energy for 1 SDD derived from Ti K α_1 and Mn K α_1 as 2 sources of calibration. Ti K β , Mn K β as well as Cu K α_1 and K β lines are also shown.

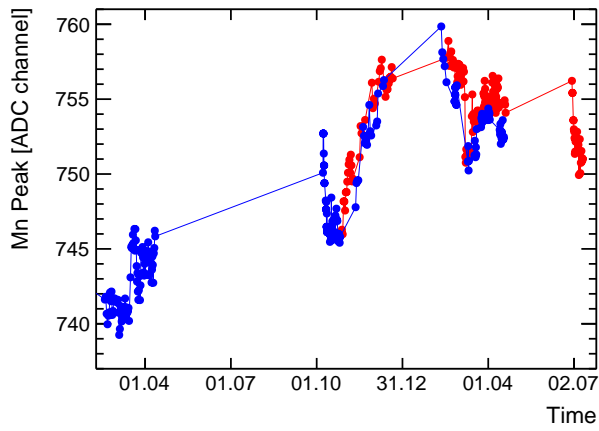


Figure 6.14.: The position of the Mn K α_1 peak for SDD 3 during the data taking at LNGS without current (blue) and with current (red). Typical statistical error is 1 ADC channel.

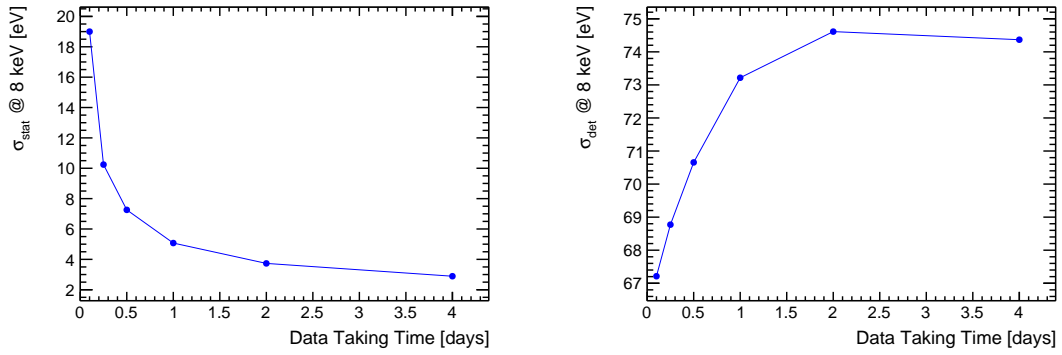


Figure 6.15.: Energy determination uncertainty at 8 keV due to statistical error of the position of the calibration lines as a function of data taking time (left). Energy resolution at 8 keV taking peak drift effects into account (right).

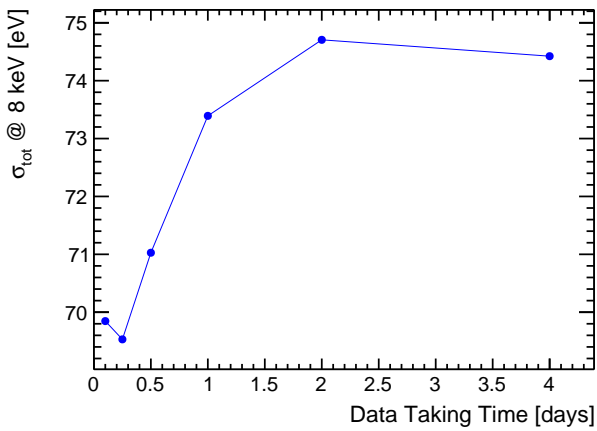


Figure 6.16.: The total uncertainty in the energy determination at 8 keV as a function of the data taking time.

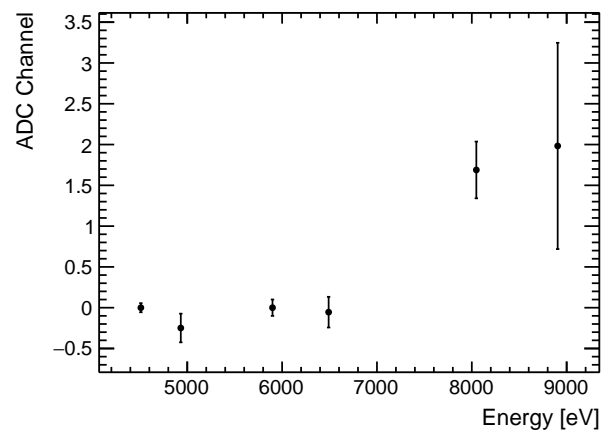


Figure 6.17.: The difference in ADC channels of the fitted position of the peaks to the position calculated with the two calibration lines.

7. Data Analysis

The data acquired with the procedures described in chapter 6 were analyzed using several techniques. The final spectra in the energy region of the PEP-violating transition with and without current are shown together with fit and residuals in figures 7.1 and 7.2. The Cu and Ni lines were fit like it was described in chapter 6.5.

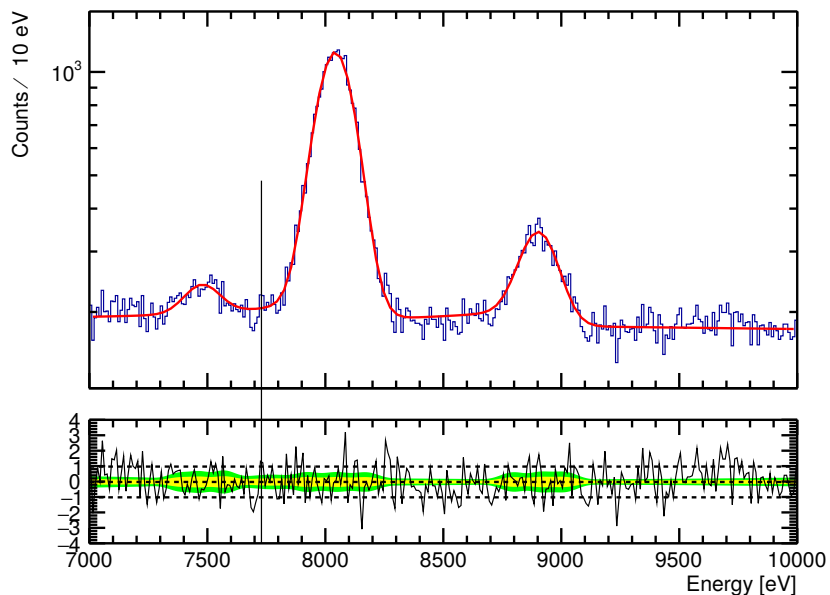


Figure 7.1.: Data taken with current on together with the fit. In the lower pad the fit residuals divided by the square root of the fit function are shown. The position of the PEP violating transition is marked in black.

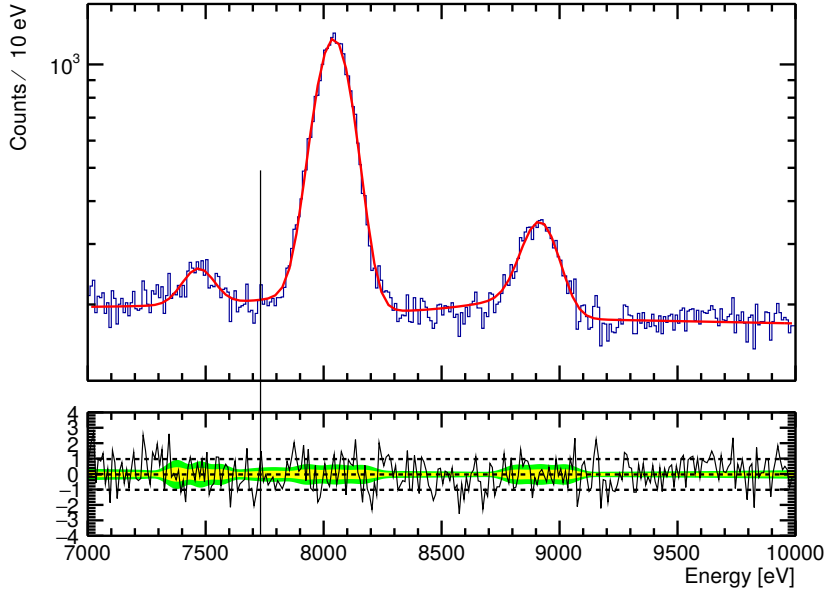


Figure 7.2.: Data taken without current together with the fit. In the lower pad the fit residuals divided by the square root of the fit function are shown. The position of the PEP violating transition is marked in black.

7.1. Spectral Subtraction Analysis

One approach to calculate the upper limit for the probability of the violation of the PEP from two energy spectra recorded with and without current was described by E. Ramberg and G. A. Snow in [2]. The basic principle is to look for an excess of events in the energy region of the Pauli-forbidden transition in the spectrum taken with current compared to the spectrum without current (see also chapter 2.4). If the PEP can be violated, photons from this transition are expected to occur and introduce this difference between the two spectra. From the difference or the lack thereof, and experimental parameters, the probability for the violation of the PEP or an upper limit for it can be calculated. This analysis has been presented for a subset of the data in [47].

Using the same notation as in the publications about the VIP2 experiment, the number of possible detected events from PEP-violating transitions ΔN_x is related to the probability that the PEP is violated in an atom $\frac{\beta^2}{2}$ (see also chapter 2.2) as

shown in equation 7.1.

$$\Delta N_x \geq \frac{\beta^2}{2} N_{new} \frac{N_{int}}{10} (\text{detection efficiency}) \quad (7.1)$$

Here N_{new} is the number of new electrons introduced by the current. It can be calculated from the magnitude of the current (I), the data taking time (Δt) and the electronic charge (e) as follows:

$$N_{new} = \frac{1}{e} \sum (I \Delta t) \quad (7.2)$$

N_{int} is the number of scattering reaction a single electron undergoes during the passage of the Cu target. It is of the order of $\frac{D}{\mu}$, where D is the length of the target and μ is the mean free path length of electrons in Cu. The probability for absorption of the electron in the case of a scattering is assumed to be larger than 10 % [2], which introduces the factor $\frac{1}{10}$ and the greater or equal sign in the equation. The detection efficiency is the probability for a 7.7 keV photon produced in the target to be detected. This probability includes photon absorption in the target and the finite solid angle covered by the SDDs. The equation can then be rewritten as:

$$\Delta N_x \geq \frac{\beta^2}{2} \frac{1}{10} \frac{D \sum (I \Delta t)}{\mu e} (\text{detection efficiency}) \quad (7.3)$$

or

$$\frac{\beta^2}{2} \leq \frac{10 \mu e}{D \sum (I \Delta t)} \frac{\Delta N_x}{(\text{detection efficiency})} \quad (7.4)$$

The values for these parameters used in the analysis are summed up in table 7.1. Inserting these values into equation 7.4, the relation between amount of counts

μ	D	I	Δt	detection efficiency
$3.91 \times 10^{-6} \text{ cm}$ [18]	7.1 cm	100 A	81 days 10 hours	1.82 % 4

Table 7.1.: Values for the experimental parameters for the analysis of the VIP2 data.

from non-Paulian transitions and the probability for the violation of the PEP can be obtained:

$$\frac{\beta^2}{2} \leq \frac{\Delta N_x}{1.46 \times 10^{31}} \quad (7.5)$$

The number of detected counts ΔN_x needs to be determined from the energy spectra with and without current. To avoid problems with normalization, a dataset from the data without current was selected with the same data taking time as the data with current (81 days 10 hours). ΔN_x was calculated as the difference in

counts in the region of interest (ROI) around the non-Paulian Cu K α transition. As the center of this region the energy of the forbidden Cu K α_2 transition of 7729 eV (see chapter 2.4) is usually taken. As its width the FWHM of the Cu K α line of the spectrum with current is assumed. The energy resolutions at 8 keV for the spectra of the sum of all 6 SDDs with and without current were determined by fitting the Cu lines in the same way as it was done for the calibration lines of Ti and Mn (see chapter 6.5):

$$\text{FWHM (8 keV)} = 188.5 \pm 1.86 \text{ eV} \quad \text{with current} \quad (7.6)$$

$$\text{FWHM (8 keV)} = 177.7 \pm 1.73 \text{ eV} \quad \text{without current} \quad (7.7)$$

maybe redo fit with
RIE

To account for a theoretical uncertainty of 10 eV of the energy of the PEP-violating transition [48], the width of the ROI was chosen as 200 eV instead of 188.5 eV. It spans the energy range from 7629 eV - 7829 eV. The energy region around the Pauli-forbidden transition of the two spectra consisting of the sum of all six SDDs for the spectra with and without current are shown in figure 7.3. On the right side

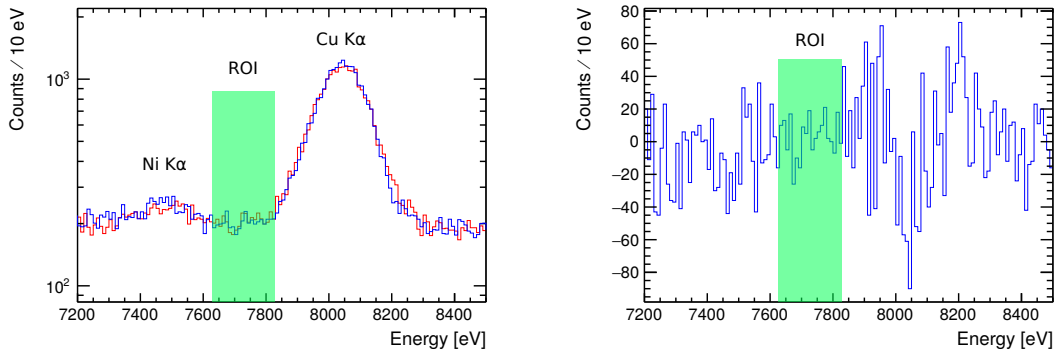


Figure 7.3.: Spectrum with current (red) and without current (blue) around the region of interest (green) on the left. The subtracted spectrum is shown on the right.

of the figure the spectrum without current was subtracted from the spectrum with current. No significant peak structure can be made out in this figure around the 7729 eV of the forbidden transition. From these spectra ΔN_x can be calculated as the difference between the counts in the ROI in the spectrum with current and the spectrum without current:

- with I = 100 A: $N_X = 4119 \pm 64$
- with I = 0 A: $N_X = 4056 \pm 64$

- for the subtracted spectrum: $\Delta N_X = 63 \pm \sqrt{64^2 + 64^2} = 63 \pm 91$

The statistical error on the counts in the ROI in the spectra with and without current are calculated as \sqrt{N} when N are the counts, as the number of events are distributed according to a Poisson distribution with mean N . [more information?](#)

The statistical error of ΔN_X is the square root of the sum of variances of N_X . The number of events from PEP-violating transitions is compatible with zero within 1σ . An upper limit on the probability for a violation of the PEP can be set using 3σ as the upper limit of ΔN_X resulting in a 99.7 % C.L.:

$$\frac{\beta^2}{2} \leq \frac{3 \times 91}{1.46 \times 10^{31}} = 1.87 \times 10^{-29} \quad (7.8)$$

This value is an improvement by a factor of 2.5 compared to the results of the VIP experiment of 4.7×10^{-29} given in [4].

7.2. Simultaneous Fit

[Another approach to determining the upper limit on the probability for the violation of the PEP is the simultaneous fit of the signal \(with current\) and the background \(without current\) spectrum.](#) This method was applied in the analysis of kaonic atomic precision spectroscopy data in [49]. A global χ^2 function was defined for the fits of the two histograms of the energy spectra which was minimized for both spectra at the same time. A Gaussian distribution was added to the fit function of the signal histogram at 7729 eV, which represents the contribution from non-Paulian transitions. Its position was fixed, its width was the same as the one of the Cu K α line of the signal histogram and its gain was a free parameter.

[add plot with difference between fit function and with current hist](#)

For the background function, a 1st order polynomial was chosen. The two parameters for this function were free and common for the fits of both histograms. The position of the Cu K α , Cu K β and Ni K α lines were kept fixed to their physical values. All other parameters like the widths and the gain of these lines were free parameters and independent for both histograms. With this method, the estimated number of candidate events and its error can directly be obtained from the converged minimum χ^2 fit. In this case the MINUIT package of the CERN ROOT software framework with MINOS error estimation was used. Special care was taken that the crucial error assessment was not perturbed by boundaries of fit parameter ranges. The results of this fit are shown in figure 7.4. The fit corresponds to a reduced χ^2 of 1.27.

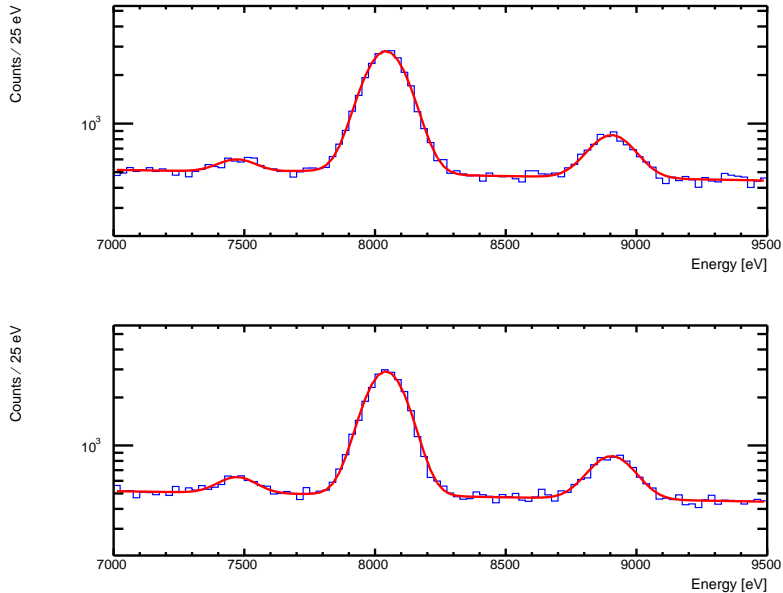


Figure 7.4.: The fits obtained by a simultaneous fit of the signal histogram with current (above) and the background histogram (below) with a few common parameters.

This method has a few advantages compared to the subtraction method described in chapter 7.1. On the one hand the definition of a region of interest is not necessary. In the simultaneous fit function this is not needed, as the fit makes use of a wide energy range for the determination of the parameters of the global fit function, from which the number of candidate PEP-violating events is calculated. On the other hand the error of the gain of the Gaussian representing the forbidden transition takes into account uncertainties of the other fit parameters. These uncertainties are usually not evaluated using the subtraction method.

The fit result for the number of detected photons from PEP-violating transitions was 102 ± 79 . This is more than 1σ away from but not enough to claim a discovery. This is why more data is needed to prove or disprove this excess. In the meantime the error of the gain of the Gaussian can, in analogy to the subtraction method, be used to set a 3σ upper limit of detected photons from PEP-violating transitions of 3×79 . With formula 7.5 the upper limit for the violation of the PEP can be calculated:

$$\frac{\beta^2}{2} \leq \frac{3 \times 79}{1.46 \times 10^{31}} = 1.63 \times 10^{-29} \quad (7.9)$$

7.3. Bayesian Count Based Analysis

The Bayes' theorem links the estimate of a parameter (*a-priori distribution*, f_0) with the probability to find the measured data given a certain value for this parameter (*likelihood function*, L) to calculate the probability distribution for this parameter given the measured data (*a-posteriori distribution*, f). For a measured quantity X and a parameter λ that shall be estimated from these data it can be written as:

$$f(\lambda|X) = \frac{L(X|\lambda)f_0(\lambda)}{\int L(X|\lambda)f_0(\lambda)d\lambda} \quad (7.10)$$

For a detailed discussion of the uses of this theorem in particle physics see for example [50].

The following model was described in [51]. In the case of the VIP2 data the measured data can be interpreted as the number of counts X in a certain energy region which is distributed according to a Poisson distribution characterized by the parameter λ .

$$L(X|\lambda) = \frac{\lambda^X e^{-\lambda}}{X!} \quad (7.11)$$

This is the likelihood function of the number of counts X given a parameter λ . The width of the energy region is arbitrary, as any two energy regions can be combined and the sum of their counts will again be distributed according to a Poisson distribution. As non-informative prior for λ a flat uniform distribution larger than zero was chosen. This encodes the fact, that there can not be a negative amount of events from PEP-violating transitions. The posterior for λ can be written with the Bayes theorem as:

$$f(\lambda|X) = \frac{\frac{\lambda^X e^{-\lambda}}{X!} f_0(\lambda)}{\int_0^\infty \frac{\lambda^X e^{-\lambda}}{X!} f_0(\lambda) d\lambda} \quad (7.12)$$

As the integral over a Poisson distribution is one, the normalization integral equals one and the posterior for λ is:

$$f(\lambda|X) = \frac{\lambda^X e^{-\lambda}}{X!} \quad (7.13)$$

This is a Gamma distribution characterized by the parameters a (*shape parameter*) = $X + 1$ and b (*scale parameter*) = 1. The mean of λ is equal to $ab = X + 1$, the variance is $ab^2 = X + 1$ and the mode is $(a - 1)b = X$. In the case of data without current and therefore with no signal, the only contribution to the number of events in the region of interest are background events, which we now call X_{bg}

with a distribution parameter λ_{bg} . For the histogram with current there are two contributions to the number events in the ROI X_s , namely from background events and from signal events from the PEP-violating transition X_{sg} . The counts coming from background is seen as drawn from a Poisson distribution with the same parameter as the one from the histogram without current λ_{bg} , and the amount of signal counts is drawn from a distribution parametrized by λ_{sg} . The likelihood function for the signal histogram is then:

$$L(X_s|\lambda_{sg}, \lambda_{bg}) = \frac{(\lambda_{sg} + \lambda_{bg})^{X_s} e^{-(\lambda_{sg} + \lambda_{bg})}}{X_s!} \quad (7.14)$$

Applying Bayes' theorem with a constant positive prior for λ_{sg} , the distribution of this parameters as a function of X_s and λ_{bg} can be obtained:

$$f(\lambda_{sg}|X_s, \lambda_{bg}) = \frac{(\lambda_{sg} + \lambda_{bg})^{X_s} e^{-\lambda_{sg}}}{\int_0^\infty (\lambda_{sg} + \lambda_{bg})^{X_s} e^{-\lambda_{sg}} d\lambda_{sg}} \quad (7.15)$$

The normalization integral does not reduce to one but equals $e^{\lambda_{bg}} \Gamma(1 + X_s, \lambda_{bg})$, as the integration variable is λ_{sg} and not $(\lambda_{bg} + \lambda_{sg})$. The distribution of λ_{sg} was calculated numerically by sampling λ_{bg} according to its distribution obtained from X_{bg} (see equation 7.13). The Mathematica software framework was used [52]. The code is listed in C. Counts in the ROI with current X_s were equal to 4119 and counts in the ROI without current X_{bg} were equal to 4056 (see also chapter 7.1).

The confidence interval corresponding to a 99.7 % C.L. spans $0 < \lambda_{sg} < 310$. With equation 7.5, the upper limit on the probability for a violation of the PEP can be calculated:

$$\frac{\beta^2}{2} \leq \frac{310}{1.46 \times 10^{31}} = 2.13 \times 10^{-29} \quad (7.16)$$

The posterior probability density (P.P.D.) and the cumulative distribution function (C.D.F.) of the posterior probability of the parameter λ_{sg} are shown in figure 7.5. From the C.D.F. an upper limit for λ_{sg} at 99.7 % confidence level of about 310 can be estimated.

7.4. Bayesian Fit Based Analysis

The RooFit [53] and RooStats [54] frameworks were used to calculate an estimation for the number of events from PEP-violating transitions using not only the number of counts in the ROI, but the information from the complete histogram. In a first step the histogram without current was fit. The background level was extracted

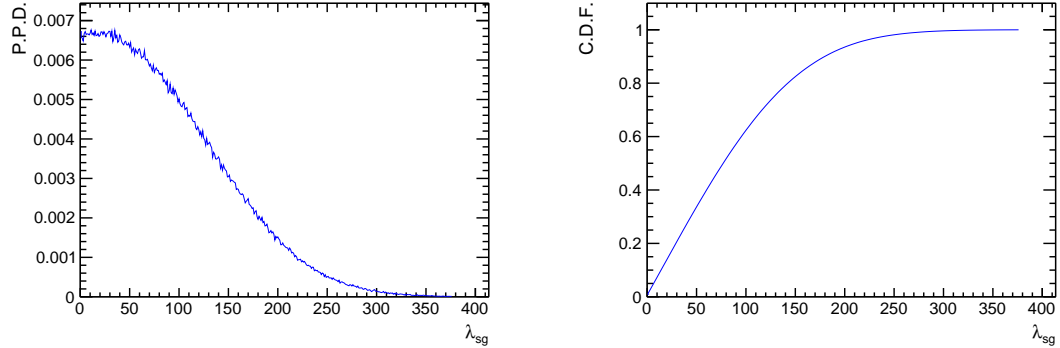


Figure 7.5.: The posterior probability density (left) and cumulative distribution function (right) of λ_{sg} for a flat positive prior.

as a first order polynomial including its errors. Then the histogram with current was fit with the parameters for the background taken from the previous fit and kept constant. The fit of the histogram with current included a Gaussian function with a fixed mean of 7729 eV and the same width as the main Cu K α peak. The outcome of this fit was used as an input for a RooStats::BayesianCalculator. The number of signal events at 7729 eV was the parameter of interest. A uniform distribution for values larger than zero was used as its a-priori distribution. The two parameters of the first order polynomial of the background were treated as the nuisance parameters and were marginalized using a MC integration method. Parts of the code are shown in C. The posterior density for the amount of signal events is shown in figure 7.6. The upper limit of the parameter of interest corresponding to a 99.7 % confidence level is at 365 signal events. With formula 7.5, the upper limit for the probability for a violation of the PEP can be calculated:

$$\frac{\beta^2}{2} \leq \frac{365}{1.46 \times 10^{31}} = 2.51 \times 10^{-29} \quad (7.17)$$

normalization?

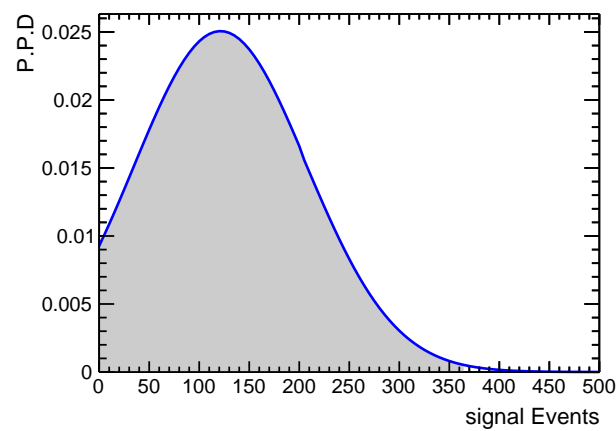


Figure 7.6.: The posterior probability density for the number of events from PEP-violating transitions for a flat positive prior.

8. Summary and Outlook

The goal of this work was to conduct the most stringent test of Spin-Statistics and specifically the Pauli Exclusion Principle for electrons in an experiment circumventing the Messiah-Greenberg superselection rule. For this purpose the VIP2 (Violation of the Pauli Principle) experimental setup was built and tested at Stefan Meyer Institute and was later brought to the underground laboratory LNGS in Italy for data taking. The predecessor experiment VIP set an upper limit for the probability for the violation of the PEP of 4.7×10^{-29} [4]. A violation of the PEP can be detected in the VIP2 experiment by searching for photons from a Cu conductor, which are coming from Pauli-forbidden 2p to 1s transitions. These transitions have a slightly lower transitions energy than normal transitions, because they can have 2 electrons in the ground state already before the transition happens. The second electron increases the shielding of the potential of the nucleus and thereby reduces the transition energy by around 300 eV. These transitions are expected when a current is flowing through the Cu conductor. The limit on the PEP is calculated from an excess of photons in this energy region in the histogram recorded with a current compared to the histogram without current.

The core part of the setup are Silicon Drift Detectors (SDDs) recording the photon spectrum from the Cu conductor. An active shielding system consisting of plastic scintillators read out by Silicon Photomultipliers was installed around these detectors to veto events caused by external ionizing radiation. These systems were exhaustively tested first at LNF in Italy and at SMI together with the cooling system of the SDDs and the slow control and data acquisition systems. The results are summed up in table 8.1. The argon cooling kept the temperature of the SDDs at about 100 K. The functionality of the slow control and the data acquisition systems was verified. A current through the Cu conductor of up to 180 A was tested and a stable target temperature of about 20 °C was verified under these conditions. The data taken at SMI and LNGS corresponds to the results predicted by Geant4 simulations in several aspects:

- The simulated SDD hit rate of cosmic radiation corresponds to the measured rate of events rejected by scintillator veto at SMI.

Active Shielding			SDDs		
Detection Efficiency			Time Resolution	Energy Resolution	Time Resolution
500 MeV e ⁻	Cosmic Radiation	γ Radiation	FWHM	FWHM @ 6 keV	FWHM
98 %	> 90 %	< 1 %	2.3 ns	150 eV	380 ns

Table 8.1.: Results of the test measurements at LNF and at SMI for the active shielding and the SDDs.

- The scintillator hit rate of cosmic radiation estimated from simulations corresponds to the measured rate of events with high QDC values at LNGS.
- The constant part of the background spectrum measured at LNGS is equivalent to the one obtained by simulations of high energy photon radiation.

The final analyzed data corresponds to 81 days and 10 hours with a 100 A current and the same amount of data without current for all six SDDs. The upper limit for the probability for a violation of the PEP was calculated from the difference in the energy region of the PEP-forbidden transition at 7729 eV of these two spectra. Several techniques were used to calculate the 99.7 % C.L. upper limit, which give slightly different values:

1. Difference of counts in the region of interest of the two histograms. The upper limit is calculated from the statistical error of this difference, assuming a Poisson distribution for the number of counts in each energy bin.
2. Simultaneous fit of the two spectra, with an additional signal Gaussian function in the histogram with current. The upper limit is calculated from the statistical error of the gain of this Gaussian.
3. Difference of counts in the region of interest of the two histograms using Bayesian statistics. The upper limit is calculated from the posterior distribution, which uses a flat positive prior distribution and a Poisson distribution as likelihood function.
4. A fit of the histogram with current including a Gaussian function at the energy of the PEP-forbidden transition is done, using the background function obtained from the histogram without current. From the result of this fit and the data a posterior distribution for the amount of signal counts is calculated using a flat positive prior.

The results of these different methods are summed up in table 8.2. For comparison

	1. Spectrum Subtraction	2. Simultaneous Fit	3. Bayesian Subtraction	4. Bayesian Fit
Upper Limit $\frac{\beta^2}{2}$	1.87×10^{-29}	1.63×10^{-29}	2.13×10^{-29}	2.51×10^{-29}

Table 8.2.: Results for the upper limit for the violation of the PEP using different analysis techniques.

with other publications about this and related experiments, the limit from the spectrum subtraction of:

$$\frac{\beta^2}{2} \leq 1.87 \times 10^{-29} \quad (8.1)$$

can be used. This result represents an improvement on the limit set by the VIP experiment by a factor of 2.5.

The VIP2 setup is currently (February 2018) at the Stefan Meyer Institute for testing and mounting new SDDs with a larger active area (23 cm^2) and a larger operating temperature of around 230 K, which enables the use of Peltier cooling [43]. After the work at SMI is finished, the setup will be transported to LNGS, where further data will be taken with an additional passive shielding consisting of Pb and Cu blocks of 5 cm thickness. After around 3 more years of data taking, the anticipated new upper limit for the probability of the violation of the Pauli Exclusion Principle will be on the order of 10^{-30} - 10^{-31} . Or else, a violation of the Pauli Exclusion Principle will be discovered.

Bibliography

- [1] M. Goldhaber and Gertrude Scharff-Goldhaber. Identification of Beta-Rays with Atomic Electrons. *Physical Review*, 73(12):1472–1473, jun 1948.
- [2] Erik Ramberg and George A Snow. Experimental limit on a small violation of the Pauli principle. *Physics Letters B*, 238(2):438–441, 1990.
- [3] C Curceanu, S Bartalucci, A Bassi, S Bertolucci, M Bragadireanu, M Cargnelli, A Clozza, S Di Matteo, S Donadi, J-P Egger, C Guaraldo, M Iliescu, T Ishiwatari, M Laubenstein, J Marton, E Milotti, D Pietreanu, M Poli Lener, T Ponta, A Rizzo, A Romero Vidal, A Scordo, D L Sirghi, F Sirghi, L Sperandio, O Vazquez Doce, E Widmann, and J Zmeskal. Experimental tests of Quantum Mechanics: from Pauli Exclusion Principle Violation to spontaneous collapse models. *Journal of Physics: Conference Series*, 361:012006, 2012.
- [4] C. Curceanu, S. Bartalucci, S. Bertolucci, M. Bragadireanu, M. Cargnelli, S. Di Matteo, J. P. Egger, C. Guaraldo, M. Iliescu, T. Ishiwatari, M. Laubenstein, J. Marton, E. Milotti, D. Pietreanu, T. Ponta, A. Rizzo, A. Romero Vidal, A. Scordo, D. L. Sirghi, F. Sirghi, L. Sperandio, O. Vazquez Doce, E. Widmann, and J. Zmeskal. Experimental tests of quantum mechanics: Pauli Exclusion Principle Violation (the VIP experiment) and future perspectives. *Journal of Physics: Conference Series*, 306(1):012036, 2011.
- [5] W. Pauli. Nobel Prize lecture: Exclusion principle and quantum mechanics, 1946.
- [6] L. Sperandio. *New experimental limit on the Pauli Exclusion Principle violation by electrons from the VIP experiment*. PhD thesis, 2008.
- [7] A M L Messiah and O W Greenberg. Symmetrization Postulate and Its Experimental Foundation. *Physical Review*, 136(1B):B248—B267, 1964.
- [8] I. G. Kaplan. The Pauli Exclusion Principle. Can It Be Proved? *Foundations*

- of Physics*, 43(10):1233–1251, 2013.
- [9] W Pauli. The Connection Between Spin and Statistics. *Phys. Rev.*, 58(8):716–722, 1940.
 - [10] J. Schwinger. Spin, Statistics and the TCP Theorem. *Proceedings of the National Academy of Sciences of the United States of America*, 44(2):223–228, 1958.
 - [11] G. Luders and B. Zumino. Connection between Spin and Statistics. *Physical Review*, 110(6):1450–1453, 1958.
 - [12] A. Stern. Anyons and the quantum Hall effect—A pedagogical review. *Annals of Physics*, 323:204–249, 2008.
 - [13] H. S. Green. A generalized method of field quantization. *Physical Review*, 90(2):270–273, 1953.
 - [14] O. W. Greenberg. Theories of violation of statistics. *AIP Conference Proceedings*, 545(1):113–127, 2000.
 - [15] A.Yu. Ignatiev and V.A. Kuzmin. IS SMALL VIOLATION OF THE PAULI PRINCIPLE POSSIBLE? *International Centre for theoretical physics (Preprint)*, 87(13), 1987.
 - [16] A.B. Govorkov. Can the Pauli principle be deduced with local quantum field theory? *Physics Letters A*, 137(1-2):7–10, may 1989.
 - [17] O. W. Greenberg. Particles with small violations of Fermi or Bose statistics. *Physical Review D*, 43(12):4111–4120, 1991.
 - [18] S R Elliott, B H LaRoque, V M Gehman, M F Kidd, and M Chen. An Improved Limit on Pauli-Exclusion-Principle Forbidden Atomic Transitions. *Foundations of Physics*, 42(8):1015–1030, 2012.
 - [19] Corinaldesi and E. MODEL OF A DYNAMICAL THEORY OF THE PAULI PRINCIPLE. *Nuovo Cim.*, 43:937, 1967.
 - [20] Abner Shimony. Proposed Experiment to Test the Possible Time Dependence of the Onset of the Pauli Exclusion Principle. *Quantum Information Processing*, 5(4):277–286, aug 2006.
 - [21] F. Reines and H. W. Sobel. Test of the Pauli Exclusion Principle for Atomic

Electrons. *Physical Review Letters*, 32(17):954–954, apr 1974.

- [22] R. Bernabei, P. Belli, F. Cappella, R. Cerulli, C. J. Dai, A. D’Angelo, H. L. He, A. Incicchitti, H. H. Kuang, X. H. Ma, F. Montecchia, F. Nozzoli, D. Prosperi, X. D. Sheng, and Z. P. Ye. New search for processes violating the Pauli exclusion principle in sodium and in iodine. *The European Physical Journal C*, 62(2):327–332, jul 2009.
- [23] G. Bellini, S. Bonetti, M. Buizza Avanzini, B. Caccianiga, D. D’Angelo, D. Franco, M. Giammarchi, P. Lombardi, L. Ludhova, E. Meroni, L. Miramonti, L. Perasso, G. Ranucci, A. Re, Y. Suvorov, J. Benziger, L. Cadonati, A. Pocar, F. Calaprice, A. Chavarria, F. Dalnoki-Veress, C. Galbiati, A. Goretti, Andrea Ianni, M. Leung, B. Loer, R. Saldanha, J. Xu, C. Carraro, S. Davini, E. Guardincerri, G. Manuzio, M. Pallavicini, S. Perasso, P. Rissi, C. Salvo, G. Testera, S. Zavatarelli, H. De Kerret, D. Kryn, M. Obolensky, D. Vignaud, A. Derbin, V. Muratova, A. Etenko, E. Litvinovich, I. MacHulin, A. Sabelnikov, M. Skorokhvatov, S. Sukhotin, K. Fomenko, O. Smirnov, A. Sotnikov, O. Zaimidoroga, S. Gazzana, C. Ghiano, Aldo Ianni, G. Korga, D. Montanari, A. Razeto, R. Tartaglia, M. Goeger-Neff, T. Lewke, Q. Meindl, L. Oberauer, F. Von Feilitzsch, Y. Winter, M. Wurm, C. Grieb, S. Hardy, M. Joyce, S. Manecki, L. Papp, R. S. Raghavan, D. Rountree, R. B. Vogelaar, W. Maneschg, S. Schönert, H. Simgen, G. Zuzel, M. Misiaszek, M. Wojcik, F. Ortica, and A. Romani. New experimental limits on the Pauli-forbidden transitions in C12 nuclei obtained with 485 days Borexino data. *Physical Review C - Nuclear Physics*, 81(3):034317, mar 2010.
- [24] E Nolte, T Brunner, T Faestermann, A Gillitzer, G Korschinek, D Muller, B Schneck, D Weselka, V N Novikov, A A Pomansky, A Ljubicic, D Miljanic, and H Vonach. Accelerator mass spectrometry for tests of the Pauli exclusion principle and for detection of beta beta decay products. *Journal of Physics G: Nuclear and Particle Physics*, 17(S):S355, 1991.
- [25] D Javorsek, M Bourgeois, D Elmore, E Fischbach, D Hillegonds, J Marder, T Miller, H Rohrs, M Stohler, and S Vogt. New experimental test of the pauli exclusion principle using accelerator mass spectrometry. *Physical review letters*, 85(13):2701–4, 2000.
- [26] G. Hilscher. *Festkörperphysik 1*. 2009.
- [27] S Di Matteo and L Sperandio. VIP Technical Note IR - 4. Technical report, 2005.

- [28] J. V. Mallow, J. P. Desclaux, and A. J. Freeman. Dirac-Fock method for muonic atoms: Transition energies, wave functions, and charge densities. *Physical Review A*, 17(6):1804–1809, 1978.
- [29] C. Curceanu. EVALUATION OF THE X-RAY TRANSITION ENERGIES FOR THE PAULI-PRINCIPLE-VIOLATING ATOMIC TRANSITIONS IN SEVERAL ELEMENTS BY USING THE DIRAC-FOCK METHOD. 2013.
- [30] Emilio Gatti and Pavel Rehak. Semiconductor drift chamber - An application of a novel charge transport scheme. *Nuclear Instruments and Methods In Physics Research*, 225(3):608–614, sep 1984.
- [31] P Lechner and H Soltau. Silicon Drift Detectors for SIDDHARTA - Mounting, Bonding and Testing. Technical report.
- [32] M Cargnelli, M Bragadireanu, M Catitti, C Fiorini, T Frizzi, H Fuhrmann, F Ghio, B Girolami, C Guaraldo, M Iliescu, T Ishiwatari, K Itahashi, M Iwasaki, P Kienle, T Koike, P Lechner, P Levi Sandri, V Lucherini, A Longoni, J Marton, T Ponta, D L Sirghi, F Sirghi, H Soltau, L Struder, E Widmann, and J Zmeskal. Silicon drift detectors for hadronic atom research - SIDDHARTA. *Proceedings, International Conference on Exotic Atoms and Related Topics (EXA 2005)*, pages 1–8, 2005.
- [33] W. Leo. *Techniques for Nuclear and Particle Physics Experiments*. 2 edition, 1993.
- [34] Eljen Technology. <http://www.eljentechnology.com/>.
- [35] AdvanSiD. AdvanSiD ASD-SiPM3S-P. Technical report, 2012.
- [36] A. T.A.M. De Waele. Pulse-tube refrigerators: principle, recent developments, and prospects. *Physica B: Condensed Matter*, 280(1-4):479–482, 2000.
- [37] S. Agostinelli, J. Allison, K. Amako, J. Apostolakis, H. Araujo, P. Arce, M. Asai, D. Axen, S. Banerjee, G. Barrand, F. Behner, L. Bellagamba, J. Boudreau, L. Broglia, A. Brunengo, H. Burkhardt, S. Chauvie, J. Chuma, R. Chytracek, G. Cooperman, G. Cosmo, P. Degtyarenko, A. Dell'Acqua, G. Depaola, D. Dietrich, R. Enami, A. Feliciello, C. Ferguson, H. Fesefeldt, G. Folger, F. Foppiano, A. Forti, S. Garelli, S. Giani, R. Giannitrapani, D. Gibin, J. J. Gomez Cadenas, I. Gonzalez, G. Gracia Abril, G. Greeniaus, W. Greiner, V. Grichine, A. Grossheim, S. Guatelli, P. Gumplinger, R. Hamatsu, K. Hashimoto, H. Hasui, A. Heikkinen,

- A. Howard, V. Ivanchenko, A. Johnson, F. W. Jones, J. Kallenbach, N. Kanaya, M. Kawabata, Y. Kawabata, M. Kawaguti, S. Kelner, P. Kent, A. Kimura, T. Kodama, R. Kokoulin, M. Kossov, H. Kurashige, E. Lamanna, T. Lampen, V. Lara, V. Lefebure, F. Lei, M. Liendl, W. Lockman, F. Longo, S. Magni, M. Maire, E. Medernach, K. Minamimoto, P. Mora de Freitas, Y. Morita, K. Murakami, M. Nagamatu, R. Nartallo, P. Nieminen, T. Nishimura, K. Ohtsubo, M. Okamura, S. O’Neale, Y. Oohata, K. Paech, J. Perl, A. Pfeiffer, M. G. Pia, F. Ranjard, A. Rybin, S. Sadilov, E. di Salvo, G. Santin, T. Sasaki, N. Savvas, Y. Sawada, S. Scherer, S. Sei, V. Sirotenko, D. Smith, N. Starkov, H. Stoecker, J. Sulkimo, M. Takahata, S. Tanaka, E. Tcherniaev, E. Safai Tehrani, M. Tropeano, P. Truscott, H. Uno, L. Urban, P. Urban, M. Verderi, A. Walkden, W. Wander, H. Weber, J. P. Wellisch, T. Wenaus, D. C. Williams, D. Wright, T. Yamada, H. Yoshida, and D. Zschiesche. GEANT4 - A simulation toolkit. *Nuclear Instruments and Methods in Physics Research, Section A: Accelerators, Spectrometers, Detectors and Associated Equipment*, 506(3):250–303, 2003.
- [38] T. K. Gaisser and T. Stanev. Cosmic Rays. *The European Physical Journal C*, 15(1-4):150–156, 2000.
- [39] M. Ambrosio, R. Antolini, A. Baldini, G. C. Barbarino, B. C. Barish, G. Battistoni, Y. Becherini, R. Bellotti, C. Bemporad, P. Bernardini, H. Bilokon, C. Bower, M. Brigida, S. Bussino, F. Cafagna, M. Calicchio, D. Campana, M. Carboni, R. Caruso, S. Cecchini, F. Cei, V. Chiarella, B. C. Choudhary, S. Coutu, M. Cozzi, G. de Cataldo, H. Dekhissi, C. de Marzo, I. de Mitri, J. Derkaoui, M. de Vincenzi, A. di Credico, O. Erriquez, C. Favuzzi, C. Forti, P. Fusco, G. Giacomelli, G. Giannini, N. Giglietto, M. Giorgini, M. Grassi, A. Grillo, F. Guarino, C. Gustavino, A. Habig, K. Hanson, R. Heinz, E. Iarocci, E. Katsavounidis, I. Katsavounidis, E. Kearns, H. Kim, S. Kyriazopoulou, E. Lamanna, C. Lane, D. S. Levin, P. Lipari, N. P. Longley, M. J. Longo, F. Loparco, G. Mancarella, G. Mandrioli, A. Margiotta, A. Marini, D. Martello, A. Marzari-Chiesa, M. N. Mazziotta, D. G. Michael, P. Monacelli, T. Montaruli, M. Monteno, S. Mufson, J. Musser, D. Nicolò, R. Nolty, C. Orth, G. Osteria, O. Palamara, V. Patera, L. Patrizii, R. Pazzi, C. W. Peck, L. Perrone, S. Petrera, P. Pistilli, V. Popa, A. Rainò, J. Reynoldson, F. Ronga, C. Satriano, E. Scapparone, K. Scholberg, A. Sciubba, P. Serra, M. Sioli, G. Sirri, M. Sitta, P. Spinelli, M. Spinetti, M. Spurio, R. Steinberg, J. L. Stone, L. R. Sulak, A. Surdo, G. Tarlè, M. Vakili, C. W. Walter, and R. Webb. Measurement of the residual energy of muons in the Gran Sasso underground laboratories. *Astroparticle Physics*, 19(3):313–328, 2003.

- [40] G. Bellini, J. Benziger, D. Bick, G. Bonfini, D. Bravo, M. Buizza Avanzini, B. Caccianiga, L. Cadonati, F. Calaprice, C. Carraro, P. Cavalcante, A. Chavarria, A. Chepurnov, D. D'Angelo, S. Davini, A. Derbin, A. Etenko, F. von Feilitzsch, K. Fomenko, D. Franco, C. Galbiati, S. Gazzana, C. Ghiano, M. Giammarchi, M. Goeger-Neff, A. Goretti, L. Grandi, E. Guardincerri, C. Hagner, S. Hardy, Aldo Ianni, Andrea Ianni, D. Korablev, G. Korga, Y. Koshio, D. Kryn, M. Laubenstein, T. Lewke, E. Litvinovich, B. Loer, F. Lombardi, P. Lombardi, L. Ludhova, I. Machulin, S. Manecki, W. Maneschg, G. Manuzio, Q. Meindl, E. Meroni, L. Miramonti, M. Misiaszek, D. Montanari, P. Mosteiro, V. Muratova, L. Oberauer, M. Obolensky, F. Ortica, K. Otis, M. Pallavicini, L. Papp, L. Perasso, S. Perasso, A. Pocar, R. S. Raghavan, G. Ranucci, A. Razeto, A. Re, A. Romani, A. Sabelnikov, R. Saldanha, C. Salvo, S. Schönert, H. Simgen, M. Skorokhvatov, O. Smirnov, A. Sotnikov, S. Sukhotin, Y. Suvorov, R. Tartaglia, G. Testera, D. Vignaud, R. B. Vogelaar, J. Winter, M. Wojcik, A. Wright, M. Wurm, J. Xu, O. Zaimidoroga, S. Zavatarelli, and G. Zuzel. Cosmic-muon flux and annual modulation in Borexino at 3800 m water-equivalent depth. *Journal of Cosmology and Astroparticle Physics*, 08:049, 2013.
- [41] M. Haffke, L. Baudis, T. Bruch, A. D. Ferella, T. Marrodán Undagoitia, M. Schumann, Y. F. Te, and A. Van Der Schaaf. Background measurements in the Gran Sasso Underground Laboratory. *Nuclear Instruments and Methods in Physics Research, Section A: Accelerators, Spectrometers, Detectors and Associated Equipment*, 643(1):36–41, 2011.
- [42] C. Bucci, S. Capelli, M. Carrettoni, M. Clemenza, O. Cremonesi, L. Gironi, P. Gorla, C. Maiano, A. Nucciotti, L. Pattavina, M. Pavan, M. Pedretti, S. Pirro, E. Previtali, and M. Sisti. Background study and Monte Carlo simulations for large-mass bolometers. *European Physical Journal A*, 41(2):155–168, 2009.
- [43] J. Marton and A. Pichler. Pauli Exclusion Principle test with electrons at LNGS - Continuation of FWF P25529-N20. Technical report, 2017.
- [44] J. L. Campbell, Leonard McDonald, Theodore Hopman, and Tibor Papp. Simulations of Si(Li) x-ray detector response. *X-Ray Spectrometry*, 30(4):230–241, 2001.
- [45] S. Okada. E570 analysis summary. Technical report.
- [46] M. Krause and Oliver J. Natural Widths of Atomic K and L Levels, K-alpha X-Ray Lines and Several KLL Auger Lines. *Journal of Physical and Chemical*

Reference Data, 8(2), 1979.

- [47] Catalina Curceanu, Hexi Shi, Sergio Bartalucci, Sergio Bertolucci, Massimiliano Bazzi, Carolina Berucci, Mario Bragadireanu, Michael Cargnelli, Alberto Clozza, Luca De Paolis, Sergio Di Matteo, Jean-Pierre Egger, Carlo Guaraldo, Mihail Iliescu, Johann Marton, Matthias Laubenstein, Edoardo Milotti, Marco Miliucci, Andreas Pichler, Dorel Pietreanu, Kristian Pisicchia, Alessandro Scordo, Diana Sirghi, Florin Sirghi, Laura Sperandio, Oton Vazquez Doce, Eberhard Widmann, and Johann Zmeskal. Test of the Pauli Exclusion Principle in the VIP-2 Underground Experiment. *Entropy*, 19(7):300, 2017.
- [48] S. Bartalucci, S. Bertolucci, M. Bragadireanu, M. Cargnelli, M. Catitti, C Curceanu (Petrascu), S Di Matteo, J-P P. Egger, C. Guaraldo, M. Iliescu, T. Ishiwatari, M. Laubenstein, J. Marton, E. Milotti, D. Pietreanu, T. Ponta, D. L. Sirghi, F. Sirghi, L. Sperandio, O Vazquez Doce, E. Widmann, and J. Zmeskal. New experimental limit on the Pauli exclusion principle violation by electrons. *Physics Letters B*, 641(1):18–22, 2006.
- [49] M. Bazzi, G. Beer, G. Bellotti, C. Berucci, A.M. Bragadireanu, D. Bosnar, M. Cargnelli, C. Curceanu, A.D. Butt, A. D’Uffizi, C. Fiorini, F. Ghio, C. Guaraldo, R.S. Hayano, M. Iliescu, T. Ishiwatari, M. Iwasaki, P. Levi Sandri, J. Marton, S. Okada, D. Pietreanu, K. Pisicchia, A. Romero Vidal, E. Sbardella, A. Scordo, H. Shi, D.L. Sirghi, F. Sirghi, H. Tatsuno, O. Vazquez Doce, E. Widmann, and J. Zmeskal. K-series X-ray yield measurement of kaonic hydrogen atoms in a gaseous target. *Nuclear Physics A*, 954:7–16, oct 2016.
- [50] Olaf Behnke, Kevin Kröninger, and Thomas Schörner-Sadenius. *Data Analysis in High Energy Physics*.
- [51] K Piscicchia, C Curceanu, and E Milotti. Bayesian model for the analysis of the VIP data. 2010.
- [52] Wolfram Research. Mathematica 10.4, 2016.
- [53] Wouter Verkerke and David Kirkby. The RooFit toolkit for data modeling. 2003.
- [54] Lorenzo Moneta, Kevin Belasco, Kyle Cranmer, Sven Kreiss, Alfio Lazzaro, Danilo Piparo, Gregory Schott, Wouter Verkerke, and Matthias Wolf. The RooStats Project. 2010.

Appendices

A. Data Acquisition Layout

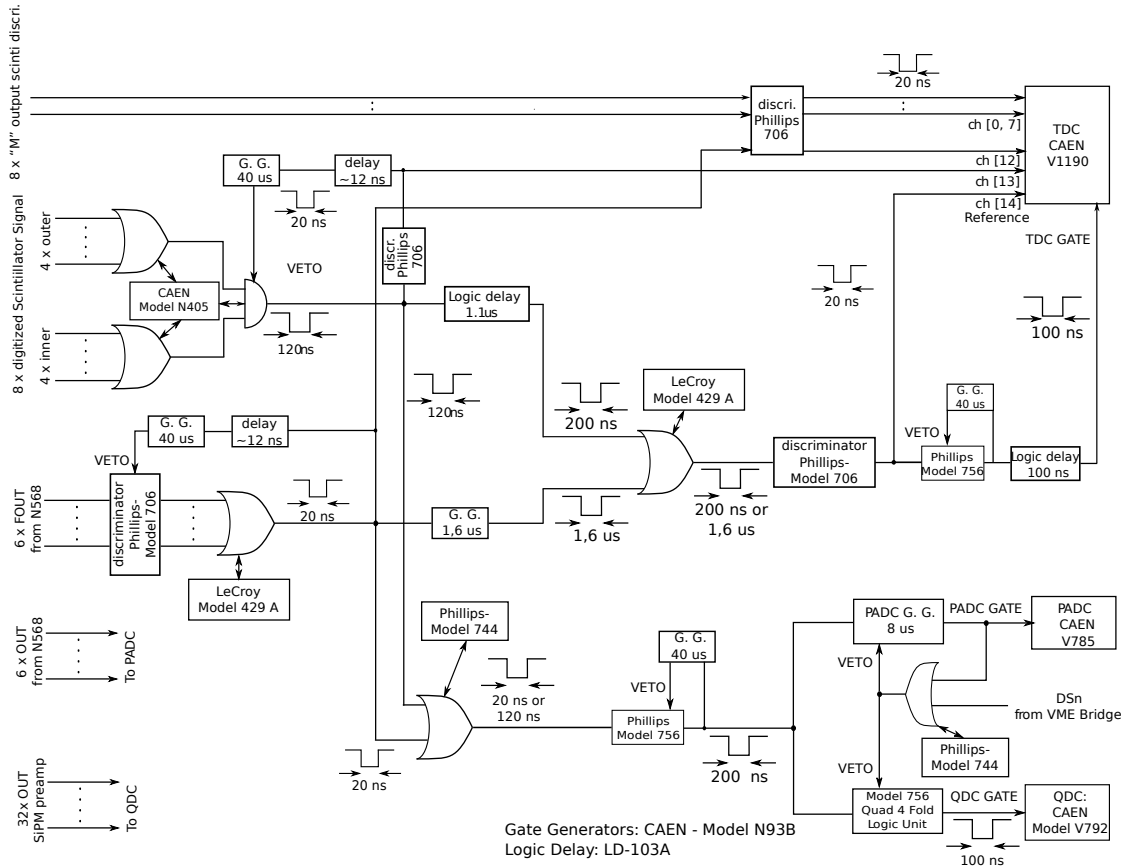


Figure A.1.: Layout of the data acquisition system for the VIP2 experiment

B. Code for Simultaneous Fit

```
Double_t funcBg(Double_t *x, Double_t *par){

    // fit of the region of roi, nickel, and cu ka kb
    // this is for fitting an already scaled histogram

    Double_t xx = x[0];

    //par[0] = background constant
    //par[10] = background slope

    Double_t back = par[0] + (xx - 7000) * par[10];

    //par[1] = cu ka1 gain
    //par[2] = cu ka1 mean
    //par[3] = cu ka1 sigma

    Double_t cuKa1 = par[1]/(sqrt(2*TMath::Pi())*par[3])*TMath::Exp
        ↪ ((xx-par[2])*(xx-par[2]))/(2*par[3]*par[3]));

    Double_t cuKa2Gain = par[1] * 0.51;
    Double_t cuKa2Mean = par[2] - 19.95;

    Double_t cuKa2 = cuKa2Gain/(sqrt(2*TMath::Pi())*par[3])*TMath::
        ↪ Exp(-((xx-cuKa2Mean)*(xx-cuKa2Mean))/(2*par[3]*par[3]));

    //par[4] = cu kb gain
    //par[5] = cu kb mean
    //par[6] = cu kb sigma
```

```

Double_t cuKb = par[4]/(sqrt(2*TMath::Pi())*par[6])*TMath::Exp
    ↪ (-((xx-par[5])*(xx-par[5]))/(2*par[6]*par[6]));

//par[7] = ni ka1 gain
//par[8] = ni ka1 mean
//par[9] = ni ka1 sigma

Double_t niKa1 = par[7]/(sqrt(2*TMath::Pi())*par[9])*TMath::Exp
    ↪ (-((xx-par[8])*(xx-par[8]))/(2*par[9]*par[9]));

Double_t niKa2Gain = par[7] * 0.51;
Double_t niKa2Mean = par[8] - 17.3;

Double_t niKa2 = niKa2Gain/(sqrt(2*TMath::Pi())*par[9])*TMath::
    ↪ Exp(-((xx-niKa2Mean)*(xx-niKa2Mean))/(2*par[9]*par[9]));

Double_t roiCuFunc = back + cuKa1 + cuKa2 + cuKb + niKa1 + niKa2
    ↪ ;
}

return roiCuFunc;
}

Double_t funcSigBg(Double_t *x, Double_t *par){

    // fit of the region of roi, nickel, and cu ka kb
    // this is for fitting an already scaled histogram

    Double_t xx = x[0];

    //par[0] = background constant
    //par[10] = background slope

    Double_t back = par[0] + (xx - 7000) * par[10];

    //par[1] = cu ka1 gain
    //par[2] = cu ka1 mean
}

```

```

//par[3] = cu ka1 sigma

Double_t cuKa1 = par[1]/(sqrt(2*TMath::Pi())*par[3])*TMath::Exp
    ↪ (-((xx-par[2])*(xx-par[2]))/(2*par[3]*par[3]));

Double_t cuKa2Gain = par[1] * 0.51;
Double_t cuKa2Mean = par[2] - 19.95;

Double_t cuKa2 = cuKa2Gain/(sqrt(2*TMath::Pi())*par[3])*TMath::
    ↪ Exp(-((xx-cuKa2Mean)*(xx-cuKa2Mean))/(2*par[3]*par[3]));

//par[4] = cu kb gain
//par[5] = cu kb mean
//par[6] = cu kb sigma

Double_t cuKb = par[4]/(sqrt(2*TMath::Pi())*par[6])*TMath::Exp
    ↪ (-((xx-par[5])*(xx-par[5]))/(2*par[6]*par[6]));

//par[7] = ni ka1 gain
//par[8] = ni ka1 mean
//par[9] = ni ka1 sigma

Double_t niKa1 = par[7]/(sqrt(2*TMath::Pi())*par[9])*TMath::Exp
    ↪ (-((xx-par[8])*(xx-par[8]))/(2*par[9]*par[9]));

Double_t niKa2Gain = par[7] * 0.51;
Double_t niKa2Mean = par[8] - 17.3;

Double_t niKa2 = niKa2Gain/(sqrt(2*TMath::Pi())*par[9])*TMath::
    ↪ Exp(-((xx-niKa2Mean)*(xx-niKa2Mean))/(2*par[9]*par[9]));

//par[11] = forbidden gauss gain
// mean of forbidden transition fixed at 7729 eV

Double_t forbGauss = par[11]/(sqrt(2*TMath::Pi())*par[3])*TMath
    ↪ ::Exp(-((xx-7729)*(xx-7729))/(2*par[3]*par[3]));

Double_t roiCuFunc = back + cuKa1 + cuKa2 + cuKb + niKa1 + niKa2
    ↪ + forbGauss;

```

```

        return roiCuFunc;
    }

struct GlobalChi2 {
    GlobalChi2( ROOT::Math::IMultiGenFunction & f1, ROOT::Math::
        ↪ IMultiGenFunction & f2) :
        fChi2_1(&f1), fChi2_2(&f2) {}

    // parameter vector is first background (in common 1 and 2) and
    // then is signal (only in 2)
    double operator() (const double *par) const {
        double p1[11]; // p1 is for background = without current
        ↪ histogram
        p1[0] = par[0]; // bg constant ..common parameter
        p1[1] = par[1]; // cu ka1 gain ... free
        p1[2] = par[2]; // cu ka1 mean ... fixed
        p1[3] = par[3]; // cu ka1 sigma ... free
        p1[4] = par[4]; // cu kb gain ... free
        p1[5] = par[5]; // cu kb mean ... fixed
        p1[6] = par[6]; // cu kb sigma ... free
        p1[7] = par[7]; // ni ka1 gain ... free
        p1[8] = par[8]; // ni ka1 mean ... fixed
        p1[9] = par[9]; // ni ka1 sigma ... free
        p1[10] = par[10]; // background slope ... common

        double p2[12]; // parameters for the fit with signal with
        ↪ current
        p2[0] = par[0]; // bg constant ..common parameter
        p2[1] = par[11]; // cu ka1 gain ... free
        p2[2] = par[12]; // cu ka1 mean ... fixed
        p2[3] = par[13]; // cu ka1 sigma ... free
        p2[4] = par[14]; // cu kb gain ... free
        p2[5] = par[15]; // cu kb mean ... fixed
        p2[6] = par[16]; // cu kb sigma ... free
        p2[7] = par[17]; // ni ka1 gain ... free
        p2[8] = par[18]; // ni ka1 mean ... fixed
        p2[9] = par[19]; // ni ka1 sigma ... free
        p2[10] = par[10]; // background slope ... common

```

```

    p2[11] = par[20]; // forbidden gauss gain ... free
    return (*fChi2_1)(p1) + (*fChi2_2)(p2);
}

const ROOT::Math::IMultiGenFunction * fChi2_1;
const ROOT::Math::IMultiGenFunction * fChi2_2;
};

Double_t combinedFit(Int_t reBin) {

    TFile *fIN = new TFile("energyHistograms.root");
    Int_t nPar = 21;
    Int_t lowerL = 7000;
    Int_t upperL = 9500;

    TH1F *hSB = (TH1F*)fIN->Get("withCurrentSum");
    TH1F *hB = (TH1F*)fIN->Get("noCurrentSmallSum");

    // setting the initial parameters for the fit
    Double_t parInit[21] = { 510. * reBin/25 , 310000. * reBin/25 ,
        ↪ 8047.78 , 75. , 79000. * reBin/25 , 8905.29 , 80. , 14900.
        ↪ * reBin/25 , 7478.15 , 72. , -0.02 , 312000. * reBin/25 ,
        ↪ 8047.78 , 80. , 78500. * reBin/25 , 8905.29 , 78. , 12000.
        ↪ * reBin/25 , 7478.15 , 71. , 0. };

    hSB->Rebin(reBin);
    hB->Rebin(reBin);

    TF1 *fB = new TF1("fB", funcBg, lowerL, upperL, 11 );
    TF1 *fSB = new TF1("fSB", funcSigBg, lowerL, upperL, 12 );

    // perform global fit

    ROOT::Math::WrappedMultiTF1 wfB(*fB,1);
    ROOT::Math::WrappedMultiTF1 wfSB(*fSB,1);

    ROOT::Fit::DataOptions opt;
}

```

```

ROOT::Fit::DataRange rangeB;
rangeB.SetRange(lowerL,upperL);
ROOT::Fit::BinData dataB(opt,rangeB);
ROOT::Fit::FillData(dataB, hB);

ROOT::Fit::DataRange rangeSB;
rangeSB.SetRange(lowerL,upperL);
ROOT::Fit::BinData dataSB(opt,rangeSB);
ROOT::Fit::FillData(dataSB, hSB);

ROOT::Fit::Chi2Function chi2_B(dataB, wfB);
ROOT::Fit::Chi2Function chi2_SB(dataSB, wfSB);

GlobalChi2 globalChi2(chi2_B, chi2_SB);

ROOT::Fit::Fitter fitter;

// create before the parameter settings in order to fix or set
// → range on them
fitter.Config().SetParamsSettings(21,parInit);
// fix some parameters
fitter.Config().ParSettings(2).Fix();
fitter.Config().ParSettings(5).Fix();
fitter.Config().ParSettings(8).Fix();
fitter.Config().ParSettings(12).Fix();
fitter.Config().ParSettings(15).Fix();
fitter.Config().ParSettings(18).Fix();

fitter.Config().ParSettings(0).SetName("Common Background
// → Constant");
fitter.Config().ParSettings(1).SetName("Cu Ka1 Gain BG");
fitter.Config().ParSettings(2).SetName("Cu Ka1 Mean");
fitter.Config().ParSettings(3).SetName("Cu Ka1 Sigma BG");
fitter.Config().ParSettings(4).SetName("Cu Kb Gain BG");
fitter.Config().ParSettings(5).SetName("Cu Kb Mean");
fitter.Config().ParSettings(6).SetName("Cu Kb Sigma BG");
fitter.Config().ParSettings(7).SetName("Ni Ka1 Gain BG");

```

```

fitter.Config().ParSettings(8).SetName("Ni Ka1 Mean");
fitter.Config().ParSettings(9).SetName("Ni Ka1 Sigma BG");
fitter.Config().ParSettings(10).SetName("Common Background Slope
    ↪ ");
fitter.Config().ParSettings(11).SetName("Cu Ka1 Gain SIG");
fitter.Config().ParSettings(12).SetName("Cu Ka1 Mean");
fitter.Config().ParSettings(13).SetName("Cu Ka1 Sigma SIG");
fitter.Config().ParSettings(14).SetName("Cu Kb Gain SIG");
fitter.Config().ParSettings(15).SetName("Cu Kb Mean");
fitter.Config().ParSettings(16).SetName("Cu Kb Sigma SIG");
fitter.Config().ParSettings(17).SetName("Ni Ka1 Gain SIG");
fitter.Config().ParSettings(18).SetName("Ni Ka1 Mean");
fitter.Config().ParSettings(19).SetName("Ni Ka1 Sigma SIG");
fitter.Config().ParSettings(20).SetName("Forbidden Gauss Gain");

// set limits
fitter.Config().ParSettings(0).SetLimits(400. * reBin/25,600. *
    ↪ reBin/25);
fitter.Config().ParSettings(1).SetLimits(200000. * reBin
    ↪ /25,400000. * reBin/25);

fitter.Config().ParSettings(3).SetLimits(72.,80.);
fitter.Config().ParSettings(4).SetLimits(70000. * reBin/25,90000.
    ↪ * reBin/25);

fitter.Config().ParSettings(6).SetLimits(75.,85.);
fitter.Config().ParSettings(7).SetLimits(10000. * reBin/25,20000.
    ↪ * reBin/25);

fitter.Config().ParSettings(9).SetLimits(60. ,85. );
fitter.Config().ParSettings(10).SetLimits(-0.05,0.05);
fitter.Config().ParSettings(11).SetLimits(200000. * reBin
    ↪ /25,400000. * reBin/25);

fitter.Config().ParSettings(13).SetLimits(75.,85.);
fitter.Config().ParSettings(14).SetLimits(70000. * reBin
    ↪ /25,90000. * reBin/25);

fitter.Config().ParSettings(16).SetLimits(75.,85.);

```

```
fitter.Config().ParSettings(17).SetLimits(10000. * reBin  
↪ /25,15000. * reBin/25);  
  
fitter.Config().ParSettings(19).SetLimits(65.,75.);  
//fitter.Config().ParSettings(20).SetLimits(0.,5000.); // no  
↪ limits on forbidden gauss gain  
  
fitter.Config().SetMinosErrors();  
fitter.Config().MinosErrors();  
fitter.FitFCN(nPar,globalChi2,parInit,dataB.Size()+dataSB.Size())  
↪ ;  
  
ROOT::Fit::FitResult result = fitter.Result();  
result.Print(std::cout);
```

C. Code for Bayesian Analysis

C.1. Count Based Analysis

```
RndList = {};
zs = 4119;
zbk = 4056;
lbkList = {};
expect = zs - zbk;
xValList = Range[0, 700];
For[i = 1, i < 100000, i++,
  lbk = RandomVariate[GammaDistribution[zbk + 1, 1]];
  probDist = ProbabilityDistribution[(lsg + lbk)^zs*Exp[-lsg]/
    (Exp[lbk]* Gamma[1 + zs, lbk]), {lsg, 0, Infinity}];
  yValList = {};
  yValList = N[PDF[probDist, xValList]];
  empDistTemp = EmpiricalDistribution[yValList -> xValList];
  r = N[RandomVariate[empDistTemp]];
  AppendTo[RndList, r];
  AppendTo[lbkList, lbk];
]
```

C.2. Fit Based Analysis

```
RooRealVar backC("backC","number_of_bg_events_without_current"
  ↪ ,31838.4,10000.,50000.);
backC.setConstant(kTRUE);

RooRealVar backS1("backS1","slope_of_the_bg_without_current"
  ↪ ,-0.05176,-1.,1.);
backS1.setConstant(kTRUE);
```

```

// set the background parameters to the values from the fit
    ↪ without current
// set them also constant for the fit

//CuKa1

RooRealVar meanCuKa1("meanCuKa1","mean_of_Cu_Ka1_gaussian"
    ↪ ,8047.78,8040.,8080.);
RooRealVar sigmaCuKa("sigmaCuKa","width_of_Cu_Ka1_gaussian"
    ↪ ,75.,70.,90.);
RooGaussian gaussCuKa1("gaussCuKa1","Cu_Ka1_PDF",energy,meanCuKa1
    ↪ ,sigmaCuKa);

RooRealVar cuKa1N("cuKa1N","cu_Ka1_Events",15000,0,100000);

//Cuka2

RooRealVar CuKa2Diff("CuKa2Diff","diff_Ka1_Ka2",19.95,19.,20.);
RooRealVar CuKa2Ratio("CuKa2Ratio","ratio_Ka1_Ka2",0.51,0.,1.);

RooGenericPdf meanCuKa2("meanCuKa2","diff_Cu_Ka1_Ka2_PDF",
    ↪ meanCuKa1_CuKa2Diff,RooArgSet(meanCuKa1,CuKa2Diff));
RooGaussian gaussCuKa2("gaussCuKa2","Cu_Ka2_PDF",energy,meanCuKa2
    ↪ ,sigmaCuKa);

RooGenericPdf cuKa2N("CuPdfRatio","ratio_Cu_Ka1_Ka2_PDF",
    ↪ cuKa1N*CuKa2Ratio,RooArgSet(cuKa1N,CuKa2Ratio));

//NiKa1

RooRealVar meanNiKa1("meanNiKa1","mean_of_Ni_Ka1_gaussian"
    ↪ ,7478.15,7470.,7500.);
RooRealVar sigmaNiKa("sigmaNiKa","width_of_Ni_Ka1_gaussian"
    ↪ ,70.,50.,90.);
RooGaussian gaussNiKa1("gaussNiKa1","Ni_Ka1_PDF",energy,meanNiKa1
    ↪ ,sigmaNiKa);

RooRealVar niKa1N("niKa1N","Nickel_Ka1_Events",200,0,1000);

//Nika2

```

```

RooRealVar NiKa2Diff("NiKa2Diff","diff_Ka1-Ka2",17.26,17.,18.);
RooRealVar NiKa2Ratio("NiKa2Ratio","ratio_Ka1/Ka2",0.51,0.,1.);

RooGenericPdf meanNiKa2("meanNiKa2","diff_Ni_Ka1-Ka2_PDF",
    ↪ meanNiKa1-NiKa2Diff",RooArgSet(meanNiKa1,NiKa2Diff));
RooGaussian gaussNiKa2("gaussNiKa2","Cu_Ka2_PDF",energy,meanNiKa2
    ↪ ,sigmaNiKa);

RooGenericPdf niKa2N("NiPdfRatio","ratio_Ni_Ka1/Ka2_PDF",
    ↪ niKa1N*NiKa2Ratio",RooArgSet(niKa1N,NiKa2Ratio));

//Background

//the variables for the background function are defined earlier

RooChebychev backgF("backgF","Background",energy,RooArgSet(backS1
    ↪ ));

// PEP violating tranistion

RooRealVar meanForbidden("meanForbidden","mean_of_the_forbidden_"
    ↪ tranistion", 7729, 7728.,7730.);
RooGaussian gaussForbidden("gaussForbidden","Forbidden_pdf",
    ↪ energy,meanForbidden,sigmaCuKa);

RooRealVar Nsig("Nsig","signal_Events",10.,0.,500.);

RooAddPdf PDFtot_nuis("PDFtot_nuis","PDFtot_nuis",RooArgList(
    ↪ gaussCuKa1,gaussCuKa2,gaussNiKa1,gaussNiKa2,backgF,
    ↪ gaussForbidden),RooArgList(cuKa1N,cuKa2N,niKa1N,niKa2N,
    ↪ backC,Nsig));

CuKa2Diff.setConstant(kTRUE);
CuKa2Ratio.setConstant(kTRUE);
NiKa2Diff.setConstant(kTRUE);
NiKa2Ratio.setConstant(kTRUE);
meanForbidden.setConstant(kTRUE);
meanCuKa1.setConstant(kTRUE);

```

```

meanNiKa1.setConstant(kTRUE);

PDFtot_nuis.fitTo(*withAD); // fit to data with current

backC.setConstant(kFALSE);
// set Background to parameters without current
backC.setError(252.7);
backS1.setConstant(kFALSE);
backS1.setError(0.010902);

nuisW->import(PDFtot_nuis);
ModelConfig sbModel;
sbModel.SetWorkspace(*nuisW);
sbModel.SetPdf("PDFtot_nuis");
sbModel.SetName("S+BLModel");
RooRealVar* poi = nuisW->var("Nsig");
poi->setRange(0.,500.);
sbModel.SetParametersOfInterest(*poi);
sbModel.SetNuisanceParameters(RooArgSet(backC,backS1));

nuisW->factory("Uniform::prior(Nsig)");
sbModel.SetPriorPdf(*nuisW->pdf("prior"));

//Construct the bayesian calculator
BayesianCalculator bc(*wConst->data("withDH")), sbModel); // 
    ↪ initialize with data taken with current
bc.SetConfidenceLevel(0.997);
bc.SetLeftSideTailFraction(0.);
bc.SetIntegrationType("plain");
bc.SetNumIters(10000);
// set number of iterations (i.e. number of toys for MC
    ↪ integrations)
bc.SetScanOfPosterior(100);
SimpleInterval* bcInt = bc.GetInterval();
RooPlot *bcPlot = bc.GetPosteriorPlot(true);

```